

Aus der Sektion für Gehirnsimulation
an der Klinik für Neurologie und experimentelle Neurologie
der Medizinischen Fakultät Charité – Universitätsmedizin Berlin

DISSERTATION

Amyloid-basierte Gehirnsimulation der Alzheimer-Krankheit
mit The Virtual Brain

Amyloid-based brain simulation of Alzheimer's disease
with The Virtual Brain

zur Erlangung des akademischen Grades
doctor medicinae (Dr. med.)

vorgelegt der Medizinischen Fakultät
Charité – Universitätsmedizin Berlin

von

Leon Stefanovski

aus Berlin

Datum der Promotion: 04.06.2021

INHALTSVERZEICHNIS

Abstract in English	S. 4
Zusammenfassung auf Deutsch	S. 5
Manteltext	S. 7
1. Einführung.....	S. 7
2. Forschungsfragen und Hypothesen.....	S. 10
3. Methoden.....	S. 12
3.1. Alzheimer's Disease Neuroimaging Initiative (ADNI).....	S. 12
3.2. Anatomische MRT.....	S. 12
3.3. Diffusions-MRT.....	S. 13
3.4. AV-45-PET.....	S. 13
3.5. Bildverarbeitung.....	S. 13
3.6. Standardisierung der strukturellen Konnektivität.....	S. 14
3.7. Ursache-Wirkungs-Modell von Abeta in TVB.....	S. 15
3.8. Graphentheoretische Analyse.....	S. 16
3.9. Spektralanalyse mittels Fourier-Transformation.....	S. 17
3.10. Statistische Methoden.....	S. 18
4. Ergebnisse.....	S. 19
5. Diskussion.....	S. 25
6. Referenzen.....	S. 28
Eidesstattliche Versicherung	S. 34
Anteilsklärung	S. 35
Auszug aus der Journal Summary List	S. 38
Druckexemplar der Originalpublikation	S. 40
Supplementary Material der Originalpublikation	S. 68
Lebenslauf	S. 82
Vollständige Publikationsliste	S. 83
Danksagung	S. 85

ABSTRACT IN ENGLISH

Introduction. Our knowledge on the underlying mechanisms as well as biomarkers and disease-modifying treatments of Alzheimer's disease still remains poor. In this work, I present a computational multi-scale brain model which links the micro-scale phenomenon of changed Excitation-Inhibition-balance to macro-scale observation of slowing in electroencephalography in Alzheimer's disease.

Methods. The neuroinformatics platform The Virtual Brain (TVB; thevirtualbrain.org) is a tool for standardized large-scale structural connectivity-based simulations of whole brain dynamics. As a novelty, we connect the protein amyloid beta (Abeta) from positron emission tomography (PET) to the phenomenon of hyperexcitability in Alzheimer's disease. Based on an averaged healthy connectome and individual PET derived distributions of Abeta, we virtualize individual brains in patients with Alzheimer's disease, mild cognitive impairment and in age-matched healthy controls using data from the ADNI-3 database (<http://adni.lni.usc.edu>). The individual Abeta burden is transferred to a regional change in Excitation-Inhibition balance, leading to local hyperexcitation. We analyze simulated electroencephalograms (EEG) and regional neural activity.

Results. The known phenomenon of EEG slowing in Alzheimer's disease could be reproduced in our simulations. We could show that the heterogeneity of the Abeta distribution (with some highly affected regions) is important to lead to the EEG slowing. The observed spectral phenomena in Alzheimer's disease were mainly observable in the network hubs, independent of the spatial localization of Abeta. We present moreover a strategy of virtual therapy with memantine by modeling N-methyl-D-aspartate (NMDA) receptor antagonism in TVB. This approach turned out potential reversibility of the observed EEG slowing in virtual Alzheimer's disease brains.

Discussion. We provide proof-of-concept with a novel mechanistic virtual brain model of Alzheimer's disease, which shows how TVB enables the simulation of large-scale phenomena caused by micro-scale features in human brains.

This abstract is modified from [1].

ZUSAMMENFASSUNG AUF DEUTSCH

Einführung. Unsere Erkenntnisse über die zugrundeliegenden Mechanismen, über Biomarker und mögliche kausale Therapien der Alzheimer-Krankheit sind nach wie vor unzureichend. In dieser Arbeit präsentieren wir ein computergestütztes Multiskalen-Gehirnmodell, welches das mikroskopische Phänomen des veränderten Gleichgewichts zwischen Exzitation und Inhibition mit der makroskopischen Beobachtung der Verlangsamung in der Elektroenzephalographie bei Alzheimer-Krankheit verknüpft.

Methoden. Die Neuroinformatik-Plattform The Virtual Brain (TVB; thevirtualbrain.org) bietet die Möglichkeit für standardisierte Simulationen der Dynamik des gesamten Gehirns auf der Basis struktureller Konnektivität. Als neues Konzept verknüpfen wir nun das Protein Amyloid-Beta (Abeta) aus der Positronenemissionstomographie (PET) mit dem Phänomen der Übererregbarkeit bei der Alzheimer-Krankheit. Basierend auf einem standardisierten gesundem Konnektom und individuellen PET-basierten Verteilungen von Abeta virtualisieren wir einzelne Gehirne bei Patienten mit Alzheimer-Krankheit, leichter kognitiver Beeinträchtigung (MCI) und altersangepassten gesunden Kontrollen (HC) unter Verwendung von Daten aus der ADNI-3-Datenbank (<http://adni.lni.usc.edu>). Die individuelle Abeta-Belastung wird auf eine regionale Veränderung des Gleichgewichts zwischen Exzitation und Inhibition übertragen, die zu lokaler Übererregung führt. Wir analysieren simulierte Elektroenzephalogramme (EEG) und regionale neuronale Aktivität.

Ergebnisse. Das bekannte Phänomen der EEG-Verlangsamung bei Patienten mit Alzheimer-Krankheit konnte in unseren Simulationen reproduziert werden. Wir konnten weiterhin zeigen, dass die Heterogenität der Abeta-Verteilung (mit einigen stark betroffenen Regionen) wichtig ist, um zu einer Verlangsamung des EEGs zu führen. Die beobachteten spektralen Phänomene bei der Alzheimer-Krankheit waren hauptsächlich in den wichtigen Netzwerkknotenpunkten (Hubs) zu beobachten, unabhängig von der räumlichen Lokalisierung von Abeta. Wir präsentieren außerdem eine Strategie der virtuellen Therapie mit Memantin durch Modellierung seines N-Methyl-D-Aspartat (NMDA) -Rezeptor-Antagonismus in TVB. Dieser Ansatz ergab eine mögliche Reversibilität *in silico* der beobachteten EEG-Verlangsamung in virtuellen AD-Gehirnen.

Diskussion. Wir liefern einen *Proof-of-Concept* mit einem neuartigen mechanistischen virtuellen Gehirnmodell der Alzheimer-Krankheit, das zeigt, wie TVB die Simulation von makroskopischen Phänomenen ermöglicht, die durch mikroskopische Merkmale im menschlichen Gehirn verursacht werden.

Diese Zusammenfassung ist modifiziert und übersetzt aus [1].

MANTELTEXT

1. Einführung

Es war eine klinische Beobachtung eines aufmerksamen Untersuchers, die im Jahr 1906 die Zukunft der Neurowissenschaften maßgeblich beeinflussen sollte. Alois Alzheimer untersuchte in diesem Jahr eine Patientin, welche im Alter von nur 56 Jahren die charakteristische Psychopathologie der damals bekannten *dementia senilis* aufwies [2]. Während Demenz bei älteren Menschen damals bereits bekannt war im Sinne des Verlusts von kognitiven Funktionen [3], war Alzheimer verwundert über das fortgeschrittene mnestiche Syndrom in diesem jungen Alter, zumal es keiner damals bekannten neurologischen Erkrankung zugeordnet werden konnte [2]. Nach dem Tod seiner Patientin Auguste D. untersuchte Alzheimer das Gehirn der Frau und konnte darin spezifische Veränderungen nachweisen, die bis heute maßgeblich sind für die neuropathologische Diagnose der später nach ihm benannten Alzheimer-Krankheit (*Alzheimer's Disease*, im Folgenden *AD*): sogenannte senile Plaques und Fibrillen [2, 4].

Bei der Demenz vom Alzheimer-Typ handelt es sich um eine progressive neurodegenerative Erkrankung vornehmlich des Großhirns, die klinisch mit einem fortschreitenden Verlust kognitiver Leistungsfähigkeit der Patienten einhergeht. Oft stellen subtile Einbußen der mnestiche Funktion ein Erstsymptom dar, in der Folge häufig begleitet mit Funktionseinbußen der Sprache und der räumlichen Orientierung sowie Apraxie. Die Erkrankung hat einen chronischen Verlauf und stellt durch den zunehmenden Verlust von Alltagsfunktionen eine erhebliche Einschränkung der Lebensqualität der Betroffenen und ihrer Angehörigen dar [5].

Viele Jahre nach Alzheimers Erstbeschreibung der Erkrankung bei Auguste D. konnte nachgewiesen werden, dass seine Patientin an einer der seltenen monogenetischen, früh einsetzenden Varianten der AD litt, da eine Mutation im Presenilin-1-Gen *PSEN1* nachgewiesen werden konnte [6].

Die eigentliche Ursache der viel häufigeren, sporadischen Form ist jedoch bis heute ungeklärt. Kausale oder auch nur krankheitsmodifizierenden Behandlungen sind daher noch nicht verfügbar [7]. Die ursprünglichen Plaques und Fibrillen konnten jedoch hinsichtlich ihrer Korrelate auf Proteinebene klassifiziert werden: es handelte sich um

das Beta-Amyloid ($A\beta_{40}$ und $A\beta_{42}$, im Folgenden Abeta) und das phosphorylierte Tau-Protein (für den griechischen Buchstaben τ bzw. TAU für *Tubulin-associated Unit* [8], im folgenden Tau) [5]. Wenngleich ihre bloße Beteiligung an der Pathogenese letztlich unbestritten scheint [9, 10], sind die genauen (auch kausalen) Zusammenhänge weiterhin unklar.

Während sich die diagnostischen Möglichkeiten in den letzten Jahren erheblich gebessert haben durch Biomarker im Liquor cerebrospinalis sowie bildgebende Verfahren [11] und die Abgrenzung zu den relevanten Differentialdiagnosen oft schon in frühen Stadien gestellt werden kann, stellt die Therapie der AD im klinischen Alltag weiterhin eine Herausforderung dar [7, 12]. Durch die demographisch bedingt steigende Prävalenz der AD [13] erlangt das Thema zudem noch zunehmende Relevanz.

Die verfügbaren Pharmaka beschränken sich auf symptomatische Wirksamkeit auf Gedächtnis und andere kognitive Funktionen, haben allerdings keinen krankheitsmodifizierenden oder verzögernden Effekt auf den Verlauf der Erkrankung [7]. Es besteht also auch hinsichtlich der Entwicklung neuer Therapieansätze weiterhin ein großer Bedarf an Grundlagenforschung, um die genauen Zusammenhänge in diesem komplexen Krankheitsbild aufzudecken und durch dessen tiefergehendes Verständnis neue Möglichkeiten der Intervention zu identifizieren [12].

Gleichzeitig wird es zunehmend evident, dass es sich selbst bei der histologisch gesicherten AD um ein multifaktorielles Krankheitsbild handelt, in welchem neben den pathognomonischen Ablagerungen von Abeta und Tau auch andere, konkomitante Proteinopathien sowie vaskuläre Schädigungen nachweisbar sind [14, 15]. Daher versuchen neuere Forschungsansätze auch, das bereits vorhandene Wissen über diese multifaktorielle Erkrankung mit technologischen Mitteln zu integrieren, um bestehende Hypothesen neu bewerten zu können und beispielsweise auf Basis vorhandener Datenbanken mit multimodalen Bildgebungsdaten sowie innovativen Algorithmen zu neuen Erkenntnissen zu gelangen [16, 17]. Das Forschungsfeld der *Computational Neuroscience* ermöglicht hier eine Diskussion bekannter Faktoren, die auf die zugrundeliegenden Mechanismen und Kausalität abzielt, und geht somit über das hinaus, was korrelationsbasierte statistische Analysen beantworten können [16, 17].

In dieser Arbeit wurde zu diesem Zwecke die Software The Virtual Brain (TVB, www.thevirtualbrain.org) verwendet [18]. Es handelt sich dabei um eine *open source* Plattform für multimodale und skalenübergreifende Gehirnsimulationen [17-20], welche Simulationen mit einem funktionellen, dreidimensionalen Modell des Gehirns ermöglicht, in welchem komplexe Zustände des Gehirns in Abhängigkeit von einer Reihe von Parametern zeitlich und räumlich simuliert werden können.

Grundlage der Arbeitsweise von TVB ist die integrale Kombination aus:

1. Strukturellen Bildgebungsdaten eines Gehirns in Form hochauflösender anatomischer Magnetresonanztomographie (MRT) [21]), welche das „Gerüst“ für die Erstellung des Netzwerkmodells und die Simulation bildet
2. Daten zur strukturellen Konnektivität zwischen den einzelnen Hirnregionen, die auf der DTI-Traktographie (DTI: diffusion tensor imaging) basieren. Die Traktographie ist ein Verfahren, welches anhand der Bewegung von Wassermolekülen in diffusionsgewichteten MR-Sequenzen die Länge und Stärke der Fasertrakte im Gehirn schätzt. Mithilfe eines sogenannten Hirnnetzwerkmodells, welches die neuronale Aktivität miteinander verbundener Areale zusammenführt, lassen sich diese Informationen nutzen, um zu simulieren, wie die Aktivität in einem Areal von der Aktivität aller mit ihm verbundenen Areale abhängig ist [20].
3. Sogenannten neuronalen Massenmodellen, welche die neuronale Aktivität als Funktion der Zeit simulieren können – für eine sogenannte neuronale Masse. Eine neuronale Masse ist eine Gruppe von Neuronen mit ähnlichen Eigenschaften, z.B. eine funktionelle Hirnregion, eine Kolumne oder ein Ensemble, je nach gewünschtem Detailgrad des Modells [22]. Das Konzept der neuronalen Massen ist eine Vereinfachung von Neuronenpopulationen im Sinne der Molekularfeldtheorie, wie sie beispielsweise auch bei der Beschreibung von Molekülen in Gasen oder Flüssigkeiten angewendet werden kann [23]. Die Dynamik innerhalb eines neuronalen Massenmodells wird meist durch Differentialgleichungssysteme mit mehreren Zustandsvariablen und Parametern beschrieben [20].

Im Rahmen meiner Promotion habe ich TVB verwendet, um ein mechanistisches Modell der AD zu konstruieren, in welchem die direkten lokalen Auswirkungen des Abeta auf die umliegenden Neurone implementiert sind. Ich habe hierfür Daten von 33 Probanden der *Alzheimer's Disease Neuroimaging Initiative* (ADNI) verwendet, welche

neben den notwendigen MR-Sequenzen auch über PET-Scans mit AV-45 verfügten, welche die lokale Abeta-Konzentration *in vivo* messen. Ziel der Arbeit war es, die Effekte dieser lokalen Abeta-abhängigen Veränderung auf die Funktionsweise des Gehirns zu untersuchen – bei Patienten mit AD, bei gesunden Kontrollen (*healthy controls*, HC) sowie bei Patienten mit leichter kognitiver Störung ohne das Vollbild der AD (*mild cognitive impairment*, MCI).

Die konkreten Überlegungen in Bezug auf die Auswahl des passenden Modells, die detaillierte Methodik der Bilddatenverarbeitung, Simulation und Auswertung sowie eine ausführliche Darstellung und Einordnung der Ergebnisse findet sich in der entsprechenden Originalpublikation [1], welche diesem Dokument angefügt ist. Im Folgenden möchte ich daher fokussiert auf die zugrundeliegenden Hypothesen eingehen und ihre Entsprechungen in den Ergebnissen hervorheben.

2. Forschungsfragen und Hypothesen

Das Ziel dieser Arbeit besteht darin, biologisch realistische Modelle des individuellen menschlichen Gehirns basierend auf empirischen Daten zu konstruieren, um die Pathomechanismen der AD zu verstehen. Um dies zu erreichen, habe ich ein Ursache-Wirkungs-Modell erstellt, das die individuelle Abeta-Ablagerung aus der PET in einen Modellparameter übersetzt. Wie in der Originalveröffentlichung erläutert, mussten zu diesem Zweck mehrere Entscheidungen bezüglich der genauen Konstruktion dieses Modells getroffen werden. Die beiden wichtigsten waren die Wahl des Jansen-Rit-Modells [24] als lokales neuronales Massenmodell und die Übersetzung von Abeta in ein verändertes Exzitations-Inhibitions-Gleichgewicht (E/I-Gleichgewicht).

Ich habe mich für das Jansen-Rit-Modell aufgrund seines biologisch plausiblen Parameterraums entschieden (mit drei Neuronenpopulationen: exzitatorische Interneurone, inhibitorische Interneurone und Pyramidenzellen), außerdem aufgrund seiner Fähigkeit, plausible lokale Feldpotentialschwingungen und realistische Frequenzen der Elektroenzephalographie (EEG) zu simulieren, sowie aufgrund des Vorhandenseins eines bekannten Parameterbereichs mit Kritikalitätsverhalten [25]. Kritikalität ist ein Phänomen aus der Beschreibung nicht-linearer Dynamik und bezeichnet einen Zustand, welcher sich nahe an einer kritischen Schwelle befindet, die das Verhalten des Systems fundamental ändert. Dies ermöglicht Simulationen, die

sehr sensitiv auf einen externen Faktor wie Abeta reagieren und auch ohne stochastisches Rauschen, wie es ansonsten oft verwendet wird, zu individuellen Unterschieden führen können.

Die Entscheidung für die Umsetzung des Abeta-Effekts war schwieriger. Auf verschiedenen Ebenen wurden molekulare Wirkungen von Abeta empirisch beschrieben: z. B. die direkte Neurotoxizität [26], Wirkungen auf die Plastizität [27-29] oder Hyperexzitation [30, 31]. Da Änderungen in der Erregbarkeit des Systems sehr präzise in TVB integriert werden können und bereits nachgewiesen wurde, dass sie zu relevanten und biologisch plausiblen Änderungen der simulierten Ergebnisse führen [25], habe ich hier eine Implementierung der Hyperexzitation durch eine Verschiebung des E/I-Gleichgewichts gewählt. Im Jansen-Rit-Modell kann das E/I-Gleichgewicht durch zwei dendritische Zeitkonstanten τ_e und τ_i beschrieben werden [24, 25].

Zuletzt musste ein empirisches Korrelat ausgewählt werden, mit welchem sich überprüfen lässt, ob die Simulationen tatsächlich zu einer Änderung durch Abeta führen. Ich entschied mich hier für die Frequenzspektren EEG sowie der lokalen Feldpotentiale, da eine Verlangsamung der Frequenzen (insbesondere mit Verschiebung aus dem Alpha- in das Theta-Band) ein lange bekanntes und gut beschriebenes Phänomen bei der AD ist [32, 33].

Die zugrundeliegenden Hypothesen sind nun folgende:

1. Hypothese:

- 1.1. Die pathologische Ablagerung von Abeta bei Patienten mit AD führt lokal zu einer Störung der Funktion inhibitorischer Interneurone, was in der Folge zu einer Übererregung auf Netzwerkebene durch Disinhibition führt.
- 1.2. Infolge lokaler Übererregung kommt es zu einer globalen Verlangsamung der Oszillationsaktivität der neuronalen Massen.
- 1.3. Die Verlangsamung der Oszillationsaktivität bei Patienten mit AD zeigt sich insbesondere in einer Verschiebung der spektralen Leistungsdichte vom Alpha-Band zum Theta-Band.

2. Hypothese:

Die virtuelle Simulation eines antagonistischen Faktors im Sinne der Verringerung der NMDA-ergen Transmission im System führt bei Patienten mit AD zur Reversibilität der beobachteten Phänomene.

3. Methoden

Eine ausführliche Beschreibung der Methoden findet sich in der Originalveröffentlichung [1] im Abschnitt **Methods**. Daher werde ich in diesem Abschnitt alle verwendeten Methoden lediglich kurz beschreiben und ihre Verwendung in dieser Arbeit erläutern.

Ein Schwerpunkt liegt dabei auf jenen Methoden bzw. Aspekten, auf die in der Originalveröffentlichung aufgrund der begrenzten Zahl an Wörtern nicht im Detail eingegangen werden konnten.

3.1. Alzheimer's Disease Neuroimaging Initiative (ADNI)

Alle empirischen Daten entstammen der *Alzheimer's Disease Neuroimaging Initiative* (ADNI). Ich habe die folgenden Modalitäten verwendet: Anatomische MRT, DTI und AV-45-PET (AV-45 ist ein Abeta-Tracer).

Die Verwendung dieser Daten ist von ADNI genehmigt und alle verwendeten Daten wurden von ADNI bereits für andere Studienzwecke verwendet [34]. Daher mussten für diese Studie keine neuen empirischen Daten erhoben werden. Eine detaillierte Beschreibung der ausgewählten Kohorte aus ADNI findet sich in der Originalveröffentlichung [1] in **Methods (S. 7-8)** .

3.2. Anatomische MRT

Die MRT-Untersuchungen wurden jeweils mit einem 3-Tesla-MRT durchgeführt. Für jede Probandin und jeden Probanden wurden räumlich hochauflösende dreidimensionale T1- und T2-gewichtete Messungen durchgeführt, auf deren Grundlage das Gehirn mit einem optimalen Kontrast aus grauer und weißer Substanz dargestellt werden kann.

3.3. Diffusions-MRT

Die individuelle strukturelle Konnektivität (*Structural connectivity*, im Folgenden SC, eine Matrix der Nervenbahnen basierend auf der fraktionierten Anisotropie) wird anhand von Datensätzen aus der DTI bestimmt. Die DTI-Bildgebung basiert auf Standard-Spin-Echo-MR-Sequenzen, die um diffusionsgewichtete Gradienten erweitert wurden. Diese Sequenzen ermöglichen die Rekonstruktion der dominanten Faserverbindungen auf der Grundlage der Anisotropie der Diffusion von Wassermolekülen entlang dieser Nervenfasern.

3.4. AV-45-PET

Um die lokale Verteilung von Abeta im Gehirn der Teilnehmer zu bestimmen, wurde ihnen intravenös der Tracer AV-45 injiziert, eine Tracersubstanz mit hoher Avidität für Abeta, die an ein Radionuklid auf Fluorbasis (^{18}F) gebunden ist, das dem Beta-Plus-Zerfall unterliegt (unter Emission von Positronen) [35]. In Gegenwart von Materie reagieren Positronen in einer sogenannten Annihilation (eine Teilchen-Antiteilchen-Reaktion) mit umgebenden Elektronen, was die Auslöschung beider Teilchen zur Folge hat und zur Emission von Photonen im Frequenzbereich der Gammastrahlung führt, die bei der PET-Untersuchung gemessen werden [36]. Die verwendeten Beta-Plus-Strahler (hier also das Isotop ^{18}F) haben eine extrem kurze Halbwertszeit und können sich aufgrund der Annihilation nicht dauerhaft im Gewebe anreichern.

Die Untersuchung mittels PET ist bei wissenschaftlichen Fragestellungen durchaus eine etablierte Methode zur Diagnostik von Demenzen. In der aktuellen Klassifikation der AD durch das *National Institute of Aging* und die *Alzheimer's Association* (NIA-AA) wird sie sogar als gleichwertig zur Untersuchung des Liquor cerebrospinalis angesehen [10].

3.5. Bildverarbeitung

Wir verwendeten eine bereits etablierte Pipeline, um die Datensätze zu analysieren [21]. Die strukturelle MRT wurde gemäß den minimalen Präprozessierungsstandards des Human-Connectome-Projekts

präprozessiert [37]. Anschließend wurde die kortikale Oberfläche gemäß der von Glasser et al. entwickelten multimodalen Parzellierung registriert [38].

Diese Parzellierung wurde anschließend verwendet, um das AV-45-PET-Bild mit der strukturellen MRT zu koregistrieren. Wir berechneten die relative Signalintensität als *Standardized Uptake Value Ratio* (SUVR) für jede parcellierte Hirnregion. Das heißt, das einzelne dreidimensionale PET-Bild wurde in eine eindimensionale Anordnung von Abeta-Belastungen pro Gehirnregion transformiert.

Die kortikale Oberfläche wurde auch verwendet, um das individuelle Modell von Kortex, Schädel und Haut zu berechnen, das für die Projektion der neuronalen Aktivität vom Inneren des Gehirns zur äußeren Oberfläche der Kopfhaut erforderlich ist. Dies ermöglicht die Simulation des EEG mit Brainstorm [39].

Die strukturelle Konnektivität wurde aus der diffusionsgewichteten MRT unter Verwendung der vorhandenen Parzellierung und der Informationen über die Orientierung der Fasertrakte berechnet, die durch die Diffusionsdaten gegeben sind. Eine ausführliche Beschreibung der erwähnten Methoden zur Präprozessierung und Prozessierung sowie der verwendeten Software finden Sie in der Originalveröffentlichung [1] im Abschnitt **Methods (S. 8 - 10)**.

3.6. Standardisierung der strukturellen Konnektivität

Das Ziel der Simulation war es, den isolierten Effekt von Abeta bei HC und denen mit MCI oder AD zu untersuchen. Um die Ergebnisse aber zweifelsfrei auf die Abeta-Verteilung zurückführen zu können, war es nötig, andere Faktoren zu eliminieren. Aus diesem Grund wurde nicht die individuelle SC der Patienten mit AD oder MCI verwendet, da diese SC selbst bereits Unterschiede zur Kontrollgruppe enthalten könnte (z.B. eine niedrigere Konnektivität), welche die Simulation dann lediglich reproduzieren würde. Durch die Verwendung derselben SC für alle Probanden unter Beibehaltung der individuellen Verteilung von Abeta gelingt eine Kontrolle aller individuellen Faktoren mit Ausnahme der Abeta-Verteilung. Infolgedessen können auch alle beobachteten Unterschiede zwischen den Probanden direkt der individuellen Abeta-Verteilung zugeordnet werden, da diese sie als alleiniges Merkmal unterscheidet.

Zur Konstruktion einer solchen standardisierten SC verwendeten wir ein einfaches arithmetisches Mittel der SC der gesunden Probanden. Die entsprechende Gleichung

findet sich in der Originalveröffentlichung [1] im Abschnitt **Methods (S. 10)**, ebenso wie eine Visualisierung der SC als Konnektivitätsmatrix sowie als Graph in **Abb. 4** in [1].

3.7. Ursache-Wirkungs-Modell von Abeta in The Virtual Brain

In dieser Arbeit haben wir das Jansen-Rit-Modell [24] für die Simulationen ausgewählt. Die detaillierten Gründe für diese Entscheidung, die mathematische Beschreibung einschließlich der zugrundeliegenden Gleichungen und ihre Integration in ein Hirnnetzwerkmodell findet sich in der Originalveröffentlichung [1] im Abschnitt **Methods (S. 11- 13)**.

Als neuartige Methode in dieser Studie haben wir ein Ursache-Wirkungs-Modell von Abeta eingeführt, welches das E/I-Gleichgewicht jeder einzelnen neuronalen Masse lokal verändert. Um dies zu erreichen, wurde das Konzept einer Transferfunktion verwendet, welche die lokale Abeta-Konzentration β_a in einen der Modellparameter übersetzt, nämlich die lokale inhibitorische Zeitkonstante τ_i . Durch eine Änderung von τ_i bei konstanten Werten der anderen Parameter ändert sich das Verhalten des Systems grundlegend. Da die Simulation in einem gekoppelten Netzwerk stattfindet und darüber hinaus sogar das neuronale Massenmodell in jeder Region ein nichtlineares System aus sechs Differentialgleichungen ist, sind die resultierenden Änderungen sehr komplex.

Die Modellierung des veränderten E/I-Gleichgewichts durch Variation der inhibitorischen Zeitkonstante τ_i ist nur eine von vielen Möglichkeiten. Die Gründe für die Wahl dieses Parameters sowie die Herleitung der verwendeten Transferfunktion finden sich in der Originalveröffentlichung [1] im Abschnitt **Methods (S. 10 - 11)**. Die vollständige mathematische Beschreibung (**Gleichungen 1 - 14**) der modifizierten Version des Jansen-Rit-Modells findet sich ebenfalls dort [1] im Abschnitt **Methods (S. 11 - 13)**. Eine ausführliche Erörterung der Einschränkungen und Vorteile des ausgewählten Modells findet sich außerdem im Abschnitt **Discussion (S. 19 - 23)** der Originalveröffentlichung [1], insbesondere in **Abb. 13**.

3.8. Graphentheoretische Analyse

Die Graphentheorie ist eine Disziplin der Mathematik, die verschiedene Probleme als sogenannte Graphen behandelt, d. h. als eine Art „Netzwerk“, welches aus Knoten sowie gerichteten oder ungerichteten Kanten zwischen ihnen besteht [40]. Die erste Anwendung dieser Theorie wurde vermutlich von Leonhard Euler im Jahr 1741 vorgestellt, um alle möglichen Spazierwege über die Brücken von Königsberg zu analysieren [41]. Wie dieses Beispiel zeigt, können die Knoten und Kanten eines Graphen sehr viele verschiedene Dinge darstellen. Knoten können z.B. die Inseln von Königsberg sein, Menschen in einem sozialen Netzwerk – oder Gehirnregionen. Kanten können Brücken, Kommunikationshäufigkeiten zwischen Menschen oder Fasertrakte im Gehirn sein. Da die Graphentheorie eine Vielzahl komplexer Probleme zu einer vergleichsweise simplen, aber hochgradig organisierten geometrischen Struktur vereinfacht, können bestimmte mathematische Methoden deutlich einfacher für ihre Analyse verwendet werden als für die Analyse des ursprünglichen Systems.

Die SC eines Gehirns wird daher häufig als Graph verstanden und als solcher in Form einer Graphendarstellung oder als Matrix visualisiert (siehe **Abb. 4** in der Originalveröffentlichung [1]). Die SC-Matrix ist per Definition eine Matrix, welche die Stärke der Verbindungen zwischen entfernten Gehirnregionen beschreibt. Die Verbindungsstärken sind ein normalisierter Wert für die Anzahl der Trakte, welche die Regionen in der Traktographie verbinden. Durch Definition eines Schwellenwerts, ab dem eine Verbindung als relevant angesehen wird, kann die SC-Matrix in eine sogenannte Nachbarhaft- oder Adjazenzmatrix für einen Graphen transformiert werden. In **Abb. 4** in [1] wurde die Schwelle beim 95. Perzentil der Verbindungsstärken festgelegt, so dass nur die stärksten 5% der Verbindungen für den Graphen verwendet wurden. Diese 5% entsprechen in der Adjazenzmatrix dem Wert Eins, während die verbleibenden Werte der Adjazenzmatrix Null entsprechen. Nun kann der Graph konstruiert werden, indem man die Knoten (Gehirnregionen) und ihre Kanten (Verbindungen) aufzeichnet. Computeralgorithmen helfen dabei, die Knoten und Kanten graphisch auf sinnvolle Weise anzuordnen, so z.B. stark verbundene Knoten nahe beieinander zu platzieren und umgekehrt. Die Analyse des Graphen kann nun verschiedene Indices für die Zentralität eines Knotens berechnen (z. B. deren Grad (*degree*), also die Anzahl der Kanten, die mit einem Knoten verbunden sind; oder die

Zentralität zwischen zwei Knoten (*betweenness centrality*), ein Maß dafür, wie viele kürzeste Verbindungen zwischen anderen Knoten den beschriebenen Knoten kreuzen) [40]. Es ist auch möglich, Eigenschaften des gesamten Graphen zu beschreiben, z. B. die Effizienz (ein inverses Maß für den typischen Abstand zwischen zwei Knoten – bei großer Effizienz ist der Weg zwischen zwei Knoten sehr kurz) [40]. Auch die Visualisierung selbst bietet Informationen über den Graphen. Wie in **Abb. 4B** der Originalveröffentlichung [1] dargestellt, weist die gemittelte SC eine Trennung der beiden Großhirnhemisphären auf, darüber hinaus hat sie einen allgemein sehr symmetrischen Aufbau und subkortikale Regionen nehmen eine dominante Rolle bei der Verbindung innerhalb und zwischen den Hemisphären ein.

Die Struktur des zugrundeliegenden SC-Graphen wurde auch verwendet, um die spektralen Befunde sowie die empirische Verteilung von Abeta in den Ergebnissen zu interpretieren (siehe **Abb. 10 – 12** in [1]).

3.9. Spektralanalyse mittels Fourier-Transformation

Wie in der mathematischen Notation des Jansen-Rit-Modells beschrieben [24], verwendet es eine sigmoidale Transfersfunktion, um das simulierte postsynaptische Potential (PSP) in eine Feuerrate umzuwandeln (siehe **Gleichungen 11 und 12** in der Originalveröffentlichung [1]). Da eine Feuerrate als Oszillation auch eine Oszillationsfrequenz besitzt, ist es möglich, ihr Leistungsdichtespektrum (Powerspektrum) unter Verwendung einer Fourier-Transformation zu berechnen. Diese Powerspektren zeigen die Zusammensetzung des Signals aus verschiedenen Frequenzanteilen - im EEG z.B. auch die Zusammensetzung aus den verschiedenen Frequenzbändern Alpha, Beta, Gamma, Theta und Delta. Beispielhafte Spektren einzelner Gehirnregionen sind in der Originalveröffentlichung [1] in **Abb. 5A–F** dargestellt. Da in der Simulation für jeden Probanden 379 Hirnregionen mit einzigartigen Powerspektren in jeweils 201 verschiedenen Parameterkonstellationen vorliegen, haben wir uns entschieden, in erster Linie den dominanten Rhythmus für die weitere Analyse zu verwenden. Der dominante Rhythmus ist die Frequenz mit der höchsten Power. Die Verteilung dominanter Rhythmen in verschiedenen Hirnregionen wird für mehrere Analysen in den **Abb. 5G-J, 6B, 6F, 6J, 7, 8, 9** und **10C-F** in [1] verwendet. Die Analysen enthalten Bewertungen von Gruppenunterschieden zwischen Diagnosegruppen; Abhängigkeiten der dominanten Frequenz von der

lokalen Abeta-Konzentration, der lokalen inhibitorischen Zeitkonstante und des globalen Skalierungsfaktors G ; sowie die räumliche Verteilung verschiedener dominanter Rhythmen im SC-Graphen des Gehirns.

3.10. Statistische Methoden

Um die gestellten Hypothesen zu testen und die Ergebnisse weiter zu analysieren und zu interpretieren wurden verschiedene statistische Methoden verwendet.

Die lineare Regressions- und Korrelationsanalyse wurde verwendet, um verschiedene lineare Abhängigkeiten zwischen den Ergebnissen zu bewerten. Im Detail wurde sie verwendet, um die lineare Abhängigkeit zu zeigen und zu quantifizieren für folgende Zusammenhänge [1]:

1. Zwischen lokaler Abeta-Konzentration und lokaler LFP-Frequenz für drei verschiedene Diagnosegruppen (**Abb. 8** in [1])
2. zwischen strukturellem *degree* und lokaler Abeta-Konzentration sowie lokaler LFP-Frequenz (**Abb. 10** in [1])
3. zwischen lokaler Übererregung und der antagonistischen Wirkung von virtuellem Memantin (**Abb. 11F** in [1]) sowie lokalem Auftreten des Theta-Rhythmus (**Abb. 12F** in [1]) sowie strukturellem *degree* (**Abb. 12G** in [1]).

Mit Ausnahme des Zusammenhangs zwischen strukturellem *degree* und der lokalen Abeta-Konzentration (**10B** in [1]) hatten alle anderen untersuchten Phänomene eine signifikante lineare Abhängigkeit mit $p < 0,0001$. Die Korrelationsanalyse ergab die Stärke dieser Abhängigkeit durch den quadratischen Korrelationskoeffizienten R^2 .

Zur Bewertung der Frequenzunterschiede zwischen den gesunden Probanden und den Patienten mit AD, HC oder MCI (**Abb. 7** [1]) wurde der nicht-parametrische Kruskal-Wallis-Test verwendet, da die untersuchten Variablen nicht der Normalitätsannahme einer ANOVA entsprachen.

Jeder durchgeführte statistische Test und die Gründe für seine Verwendung sind in der **Supplementary Table 8** der Originalveröffentlichung [1] zusammen mit der eindeutigen statistischen Frage, der Charakterisierung der verwendeten Daten und den Gruppierungsvariablen explizit aufgeführt.

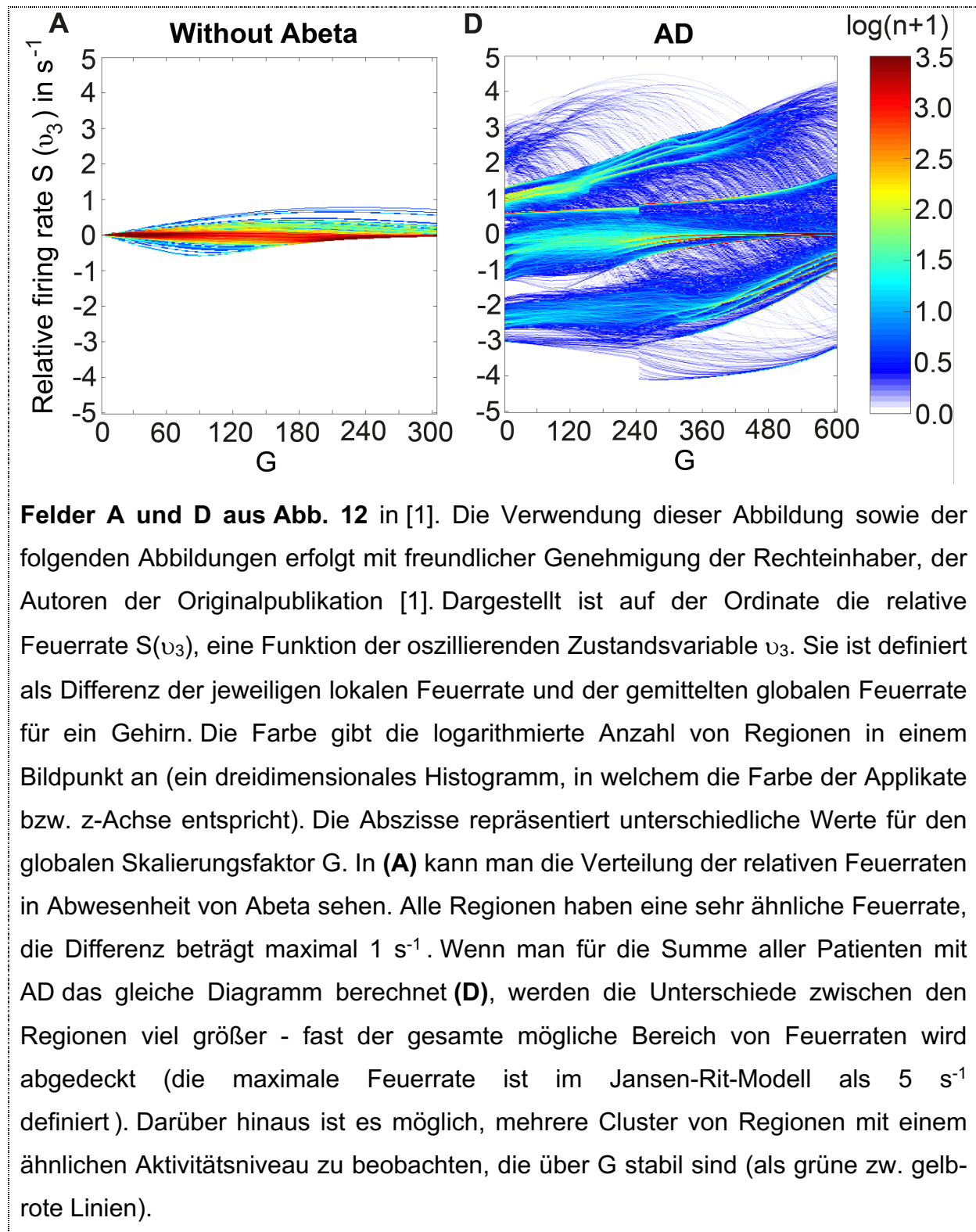
4. Ergebnisse

Im Folgenden möchte ich die wichtigsten Ergebnisse der Studie im Hinblick auf die Bewertung der Hypothesen hervorheben. Zu diesem Zweck werde ich auch einzelne Ausschnitte aus wichtigen Abbildungen der Originalfiguren anführen, um die Ergebnisse tiefergehend zu erläutern. Die vollständige Vorstellung der Ergebnisse findet sich detailliert in der Originalveröffentlichung [1], auch unter Einbezug von Erkenntnissen, die über die Hypothesen hinausgehen, weil sie sich erst aus der weiterführenden Analyse der Ergebnisse ergeben haben.

In Bezug auf die 1. Hypothese:

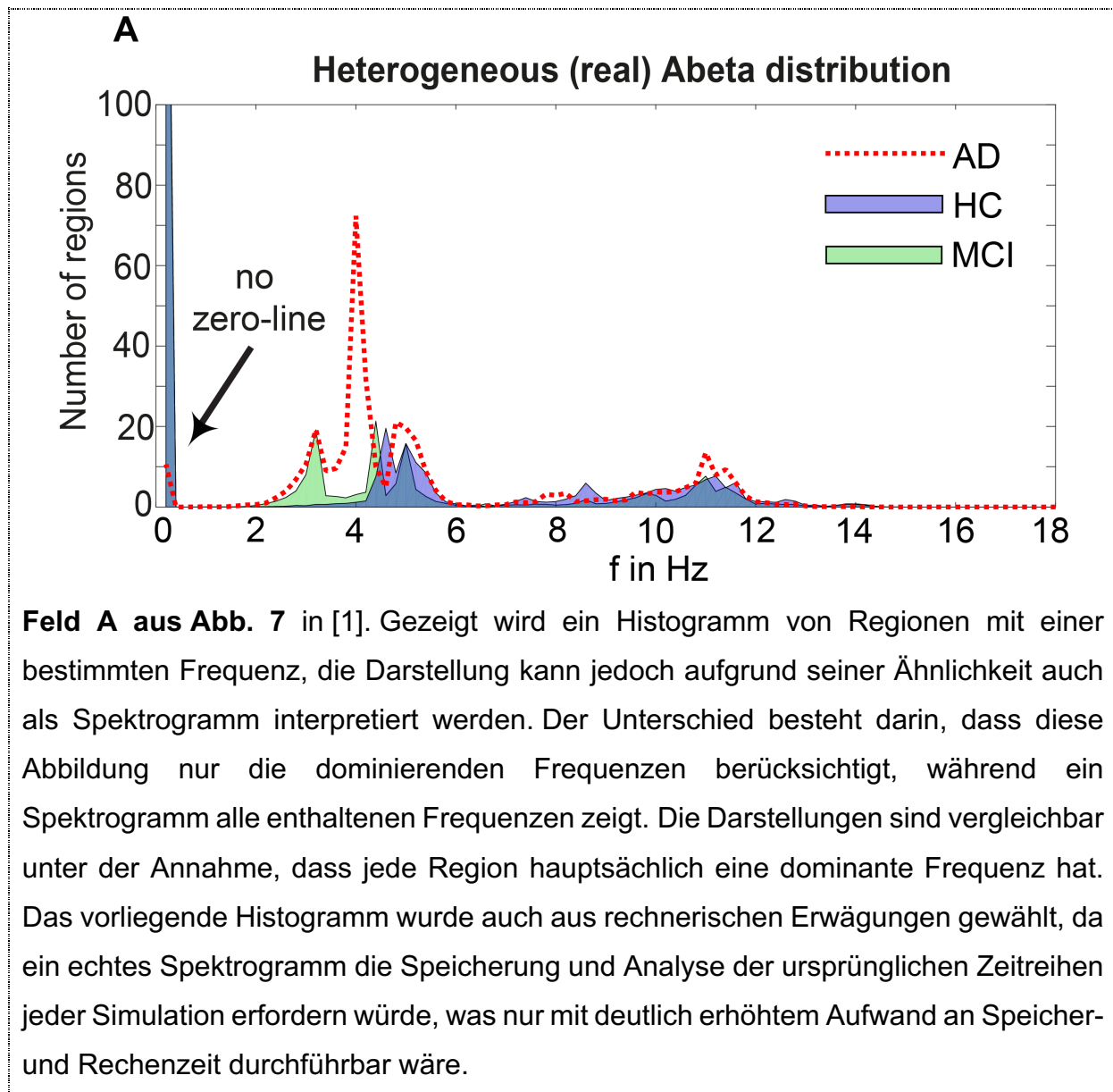
1.1. *„Die pathologische Ablagerung von Abeta bei Patienten mit AD führt lokal zu einer Störung der Funktion inhibitorischer Interneurone, was in der Folge zu einer Übererregung auf Netzwerkebene durch Disinhibition führt.“*

Während der erste, biologische Teil dieser Hypothese eine Annahme ist, die auf früheren empirischen Befunden basiert, können wir die Integration dieses Konzepts in das mathematische Modell formal beweisen. Es konnte gezeigt werden, dass mit der Einführung von Abeta sowohl stärker aktive (hyperaktive), aber auch weniger aktive (hypoaktive) Regionen auftreten – relativ im Vergleich zur mittleren Aktivität im Gehirn (siehe **Abb. 12** und Abschnitt **Discussion** in der Originalveröffentlichung [1]). Daher ist der allgemeine Satz, dass das veränderte E/I-Gleichgewicht global zu einer Übererregung führt, nicht zutreffend. Im Gegenteil führt Abeta durch ein verändertes E/I- Gleichgewicht zu lokaler Übererregung.



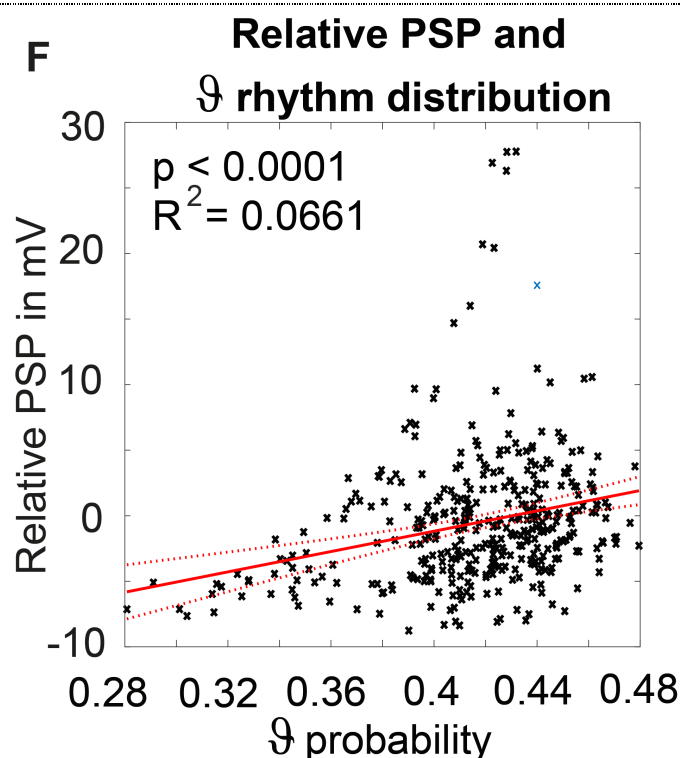
1.2. „Infolge lokaler Übererregung kommt es zu einer globalen Verlangsamung der Oszillationsaktivität der neuronalen Massen.“

Während sich der erste Teil der Hypothese auf die Kausalität bezieht und daher nicht eindeutig mit empirischen Mitteln beantwortet werden kann, kann der zweite Teil durch den Vergleich dominanter Frequenzen in verschiedenen Diagnosegruppen bestätigt werden. In Abb. 7A in [1] ist ein Histogramm dargestellt, welches die Anzahl von Regionen mit einer spezifischen dominierenden Frequenz getrennt für die gesunden Probanden, die Patienten mit AD und mit MCI visualisiert. Es können signifikante Unterschiede im Theta-Delta-Bereich (1 Hz bis 4 Hz) beobachtet werden, wobei die Patienten mit AD einen starken Peak bei 4 Hz zeigen, der in der HC- und MCI-Gruppe nicht auftritt.



Feld A aus Abb. 7 in [1]. Gezeigt wird ein Histogramm von Regionen mit einer bestimmten Frequenz, die Darstellung kann jedoch aufgrund seiner Ähnlichkeit auch als Spektrogramm interpretiert werden. Der Unterschied besteht darin, dass diese Abbildung nur die dominierenden Frequenzen berücksichtigt, während ein Spektrogramm alle enthaltenen Frequenzen zeigt. Die Darstellungen sind vergleichbar unter der Annahme, dass jede Region hauptsächlich eine dominante Frequenz hat. Das vorliegende Histogramm wurde auch aus rechnerischen Erwägungen gewählt, da ein echtes Spektrogramm die Speicherung und Analyse der ursprünglichen Zeitreihen jeder Simulation erfordern würde, was nur mit deutlich erhöhtem Aufwand an Speicher- und Rechenzeit durchführbar wäre.

Da nun das Vorhandensein einer Verlangsamung der neuronalen Frequenzen gezeigt wurde, können wir uns auf den ersten Teil der Hypothese bezüglich ihrer Ursache bei Übererregung beziehen. Wir können den Kausalzusammenhang zwar nicht beweisen, aber man kann zeigen, dass die Übererregbarkeit räumlich mit der Verlangsamung der Frequenzen korreliert (siehe **Abb. 12E-F** in [1]). Interessanterweise ist dies wahrscheinlich durch die Tatsache vermittelt, dass die Verlangsamung (sowie die Übererregung) hauptsächlich in zentralen Netzwerkanteilen stattfindet, unabhängig davon, wo die Ursache (eine erhöhte Abeta-Konzentration) verortet ist (vergleiche **Abb. 10** und **12** in [1]).



Feld F aus Abb. 12 in [1]. Ein sogenanntes Streudiagramm mit Regressionskurve, das die Beziehung zwischen lokaler Übererregung, dargestellt als relative PSP, und der Häufigkeit des Theta-Rhythmus in jeder Region zeigt. Eine lineare Regression ergab eine signifikante, aber schwache lineare Abhängigkeit mit $R^2 = 0,0661$, was bedeutet, dass nur 6,61% der Variation der regionalen Häufigkeit an Theta-Frequenzen durch die relative PSP erklärt werden können.

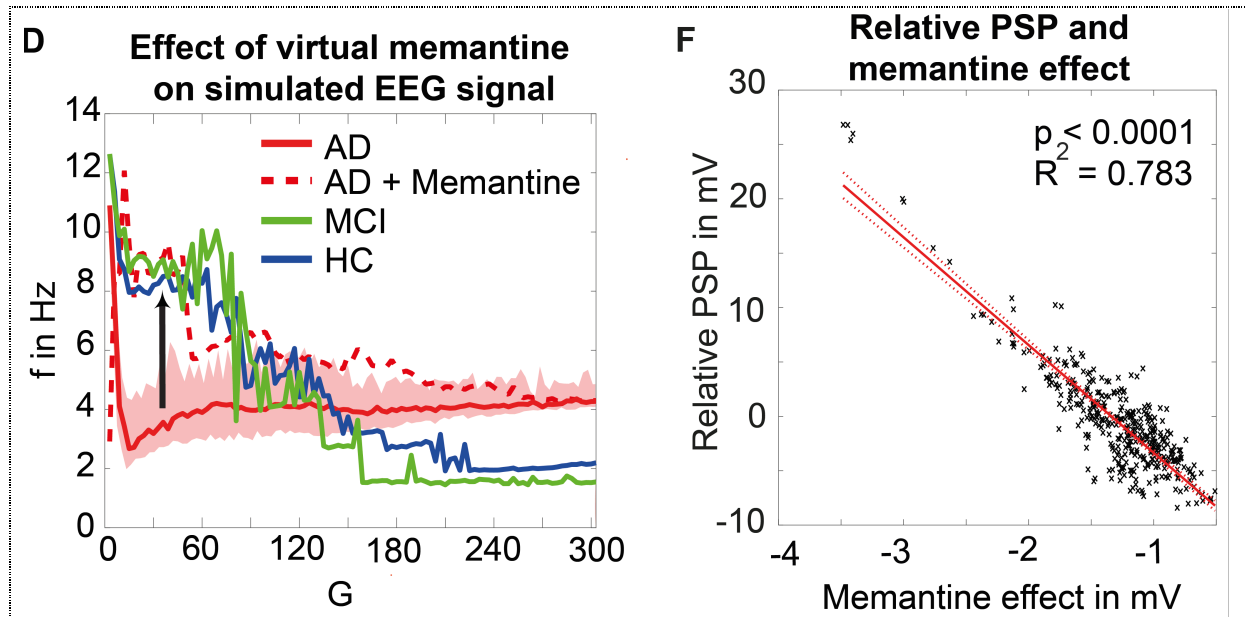
1.3. *„Die Verlangsamung der Oszillationsaktivität bei Patienten mit AD zeigt sich insbesondere in einer Verschiebung der spektralen Leistungsdichte vom Alpha-Band zum Theta-Band.“*

Diese Hypothese wurde bereits oben durch die Analyse in **Abb. 7** in [1] bestätigt. Aus mathematischer und mechanistischer Sicht kann dies durch einen detaillierten Blick in die Bifurkationsdiagramme des nichtlinearen Systems erklärt werden. Die spektrale Verschiebung von Alpha zu Theta kann mathematisch verstanden werden als eine Verschiebung zwischen zwei Grenzyklen des Jansen-Rit-Modells. Grenzyklen sind Phänomene, die in der Theorie nichtlinearer Systeme beobachtet und durch die Bifurkationstheorie beschrieben werden können. Sie sind die mathematische Ursache für Oszillationen im Jansen-Rit-Modell. Eine ausführliche Erläuterung findet sich im Abschnitt **Results** und insbesondere in **Abb. 6** in [1]. Zusammenfassend lässt sich sagen, dass sich das System in Abwesenheit von Abeta in einem Zustand mit nur einem einzigen Grenzyklus befindet, der Oszillationen im Alpha-Bereich erzeugen kann. Durch die Variation von τ_i wird ein zweiter Grenzyklus eingeführt (der langsamere Frequenzen im Theta-Delta-Bereich erzeugt). Das spektrale Verhalten ändert sich, weil ein variiertes τ_i zu grundlegenden Änderungen der Bifurkationsdiagramme (und damit der Neigung des Systems zu bestimmten Rhythmen) führt.

In Bezug auf die 2. Hypothese:

„Die virtuelle Simulation eines antagonistischen Faktors im Sinne der Verringerung der NMDA-ergen Transmission im System führt bei Patienten mit AD zur Reversibilität der beobachteten Phänomene.“

Um einen Ansatz der „virtuellen Therapie“ zu erproben, wurde ein Modell für „virtuelles Memantin“ entwickelt, indem die NMDA-erge Übertragung im Modell reduziert wurde. Die Idee dahinter war, die eingeführte Übererregbarkeit durch Abeta mit einem entgegengesetzt wirkenden Agens umzukehren. Durch Anwendung einer um 25% reduzierte NMDA-ergen Transmission auf die Patienten mit AD verringerten sich die Frequenzunterschiede zwischen den Gruppen deutlich (siehe **Abb. 11D** in [1]).



Felder D und F aus Abb. 11 in [1]. Bitte beachten Sie, dass in der Online-Version der Veröffentlichung auf Feld D eine falsche Beschriftung vorhanden ist, die es fälschlicherweise als B kennzeichnet.

(D) Zeigt die regionale Frequenz für jede Gruppe in Abhängigkeit vom globalen Skalierungsfaktor G . Für die Patienten mit AD wird sie ohne virtuelles Memantin (durchgehende rote Linie mit niedrigeren Frequenzen bei $G < 120$) und mit virtuellem Memantin (gepunktete rote Linie) dargestellt. Es ergeben sich bei Applikation des „virtuellen Memantins“ ähnliche Frequenzen für alle drei Gruppen (AD, MCI und HC) über dem gesamten Spektrum von G . **(F)** Die Reversibilität konzentriert sich auf die Hubs des Netzwerkes: Dargestellt ist ein Streudiagramm, welches die Abhängigkeit zwischen lokaler relativer Übererregung und der Wirkung von Memantin (absoluter Unterschied von PSP mit und ohne Memantin) zeigt. Eine lineare Regressionsanalyse zeigt eine sehr starke lineare Abhängigkeit ($R^2 = 0,783$). Das heißt, obwohl das virtuelle Memantin homogen auf alle Gehirnregionen angewendet wird, entfaltet es seine Wirkung hauptsächlich in zentralen Teilen des Netzwerkes, wo auch die lokale Übererregung stattfindet.

Die Originalveröffentlichung [1] enthält darüber hinaus noch weitere, vertiefende Analysen, welche über die Beantwortung der zugrundeliegenden Hypothesen hinausgehen, um die beobachteten Ergebnisse noch genauer zu charakterisieren. Bitte beachten Sie daher den Abschnitt **Results (S. 13-19)** sowie die **Abb. 11-13** (aus Platzgründen im Abschnitt **Discussion**) sowie die

Supplementary Figures 3 - 6 im Supplementary Material.

Die wesentlichen Erkenntnisse, die sich hierbei über die bloße Adressierung der Hypothesen hinaus ergaben, waren:

1. Sowohl Hyperexzitation (**Abb. 12** in [1]) als auch AD-assoziierte Theta-Frequenzen (**Abb. 10** in [1]) finden sich bevorzugt in zentralen Hirnregionen, welche besonders stark vernetzt sind. Diese Fokussierung auf zentrale Netzwerkanteile ist unabhängig von der räumlichen Abeta-Verteilung und somit als Effekt des SC-Netzwerkes zu werten.
2. Die Abeta-abhängige Verlangsamung der Frequenzen tritt nur in der AD-Gruppe auf, nicht jedoch in den Kontrollgruppen (**Abb. 8** in [1]).
3. Die Verschiebung der Oszillationsfrequenzen vom Alpha-Bereich in den unteren Theta-Bereich lässt sich anhand der Bifurkationsdiagramme des Jansen-Rit-Modells nachvollziehen (**Abb. 6** und **13** in [1]), indem man den Abeta-Konzentrationen mithilfe der Transferfunktion einen Wert für die inhibitorische Zeitkonstante τ_i zuordnet. Im Bereich des Parameterraumes, der von den vorhandenen Abeta-Konzentrationen abgebildet wird (**Abb. 9** in [1]), treten mindestens drei fundamental verschiedenen dynamische Regime auf (**Abb. 6** in [1]): bei niedrigen Abeta-Konzentrationen existiert lediglich ein Grenzzyklus mit einer Alpha-Frequenz (das *Alpha-Regime*); bei mittleren Abeta-Konzentrationen koexistieren zwei Grenzzyklen mit Alpha- und Theta-Frequenz (das *bistabile Regime*); bei hohen Abeta-Konzentrationen existiert lediglich ein Grenzzyklus mit Theta-Frequenz (das *Theta-Regime*). Abhängig davon, welche und wie viele Regionen sich in jedem der dynamischen Regime befinden, wird das Verhalten des gesamten Systems maßgeblich beeinflusst. Dieser Zusammenhang ist anhand von Beispielen ausführlich in **Supplementary Figure 6 in [1]** aufgezeigt.

5. Diskussion

Eine ausführliche Diskussion der Ergebnisse und ihrer Limitationen findet sich in der Originalveröffentlichung [1] - Abschnitt **Discussion (S. 19-23)**. Über die dort genannten Aspekte hinaus werde ich im Folgenden die Ergebnisse im klinischen Kontext verorten und einen Ausblick auf mögliche zukünftige Studien und klinische Anwendungen geben.

Zunächst möchte ich einige grundsätzliche Erwägungen bei der Entwicklung diagnostischer Instrumente in der AD-Forschung erläutern. Eine klinisch relevante, verbesserte Diagnostik kann nicht nur darin bestehen, AD-Patienten von gesunden Kontrollen zu unterscheiden, sondern muss auch zwischen anderen Diagnosen unterscheiden können: Zuerst zwischen stabilem MCI (welches sich also nicht zum Vollbild der Demenz entwickelt) und progressivem MCI (welches zu AD konvertiert), da diese Unterscheidung eine häufige Fragestellung der Patienten und ihrer Angehörigen im Setting der Früherkennung darstellt. Weiterhin von Bedeutung ist die Differenzierung zwischen AD und anderen Demenzen – insbesondere auch solchen Ursachen, die behandelt werden können (z.B. immunologische, infektiöse, vaskuläre oder metabolische Demenzen sowie der Normaldruck-Hydrozephalus). Prinzipiell bietet die Gehirnsimulation die Chance, Biomarker zu entwickeln, die mehrere dieser Aspekte abdecken können. Während nämlich viele pathogenetische Faktoren wie Abeta auf molekularer Ebene in ein rechnerisches Korrelat in einer Simulation übersetzt werden können, eignen sie sich auch als potenzielle mechanistische Biomarker. Als mechanistischen Biomarker kann man eine Größe verstehen, welche nicht nur empirisch mit einer Diagnose korreliert (ein „einfacher“ Biomarker), sondern direkt am Krankheitsmechanismus beteiligt ist. Dieser Unterschied zwischen diesen „echten“ Biomarkern und einfach korrelierten ist allerdings entscheidend für die weitere klinische Relevanz: Erstens ist die Beziehung mechanistischer Biomarker zur Krankheit tendenziell stärker und stabiler, z. B. wenn sie mit verschiedenen Methoden gemessen werden können (z. B. Abeta oder Tau, gemessen im Liquor oder im PET oder immunhistochemisch *post mortem*). Darüber hinaus eröffnet die Identifizierung eines mechanistischen Biomarkers die Möglichkeit, ein tieferes Verständnis des Krankheitsmechanismus selbst zu entwickeln. *Computational Neuroscience* liefert die theoretische Methodik, um Kandidaten für mechanistische Biomarker (wie Abeta bei AD) auf mathematisch klar beschriebene mechanistische Modelle zu übertragen. Als Pilotstudie auf diesem Gebiet haben wir die aus PET-Daten abgeleitete lokale Abeta-vermittelte Übererregbarkeit in TVB modelliert und konnten daher die detaillierten mikroskopischen und makroskopischen Mechanismen hinter der elektroenzephalographischen Verlangsamung bei AD näher beleuchten [1]. Die Präsentation einer „virtuellen Therapie“ mit Memantin gibt einen Ausblick auf die Entwicklung neuer Behandlungsstrategien mit TVB. Memantin ist bereits eine etablierte symptomatische Behandlung bei AD, aber unsere Ergebnisse reversibler

Abeta-induzierter Effekte [1] führen z. B. zu der Frage, ob eine Langzeitbehandlung mit Memantin neuroprotektiv wirken könnte. Dies ist eine Frage, die beispielsweise in einer retrospektiven Analyse oder sogar in einer prospektiven klinischen Studie untersucht werden kann. In Zukunft lassen sich auch gänzlich neue Behandlungsstrategien in TVB untersuchen. Da die Forschung mit der Gehirnsimulation nach der Virtualisierung des einzelnen Gehirns vollständig non-invasiv ist, könnte man mathematische Methoden verwenden, um das erkrankte System zurück in einen gesunden Zustand zu führen. Abhängig davon, welche Parameter geändert werden müssen, um dies zu erreichen, könnten völlig neue therapeutische *Targets* identifiziert werden. Beispielsweise haben viele verschiedene Rezeptoren des zentralen Nervensystems eindeutige Surrogate in TVB-Modellparametern, und auch alle Arten von Gehirnstimulation können im virtuellen Modell non-invasiv durchgeführt werden.

Zukünftige diagnostische Ansätze könnten auch Techniken der künstlichen Intelligenz und des maschinellen Lernens berücksichtigen, um die Verarbeitung von *Big Data* zu ermöglichen, z. B. im vollständigen ADNI-Datensatz oder in der UK Biobank [42, 43]. Nach der Untersuchung einzelner Mechanismen besteht ein weiteres Ziel darin, multimodale Datensätze in das virtuelle Gehirn zu integrieren [17, 44, 45]. Letztendlich könnten rechnerische Ansätze helfen, die Informationen aus mehreren Bereichen der empirischen AD-Forschung zu integrieren und zu dekodieren. Dies könnte in Zukunft zu einer verbesserten Diagnostik in frühen Stadien der Demenz führen sowie zu einer genaueren Prognose und Differentialdiagnose als Grundlage einer rationalen medizinischen Behandlung.

6. Referenzen

1. Stefanovski, L., P. Triebkorn, A. Spiegler, M.-A. Diaz-Cortes, A. Solodkin, V. Jirsa, A.R. McIntosh and P. Ritter for the Alzheimer's Disease Neuroimaging Initiative, *Linking Molecular Pathways and Large-Scale Computational Modeling to Assess Candidate Disease Mechanisms and Pharmacodynamics in Alzheimer's Disease*. *Frontiers in Computational Neuroscience*, 2019. **13**(54).
2. Alzheimer, A., *Über eine eigenartige Erkrankung der Hirnrinde*. *Centralblatt für Nervenheilkunde und Psychiatrie*, 1907. **18**: p. 177-179.
3. Keuck, L., *Diagnosing Alzheimer's disease in Kraepelin's clinic, 1909–1912*. *History of the Human Sciences*, 2018. **31**(2): p. 42-64.
4. Alzheimer, A., *Über eigenartige Krankheitsfälle des späteren Alters*. *Zeitschrift für die gesamte Neurologie und Psychiatrie*, 1911. **4**(1): p. 356-385.
5. Blennow, K., M.J. de Leon, and H. Zetterberg, *Alzheimer's disease*. *Lancet*, 2006. **368**(9533): p. 387-403.
6. Müller, U., P. Winter, and M.B. Graeber, *A presenilin 1 mutation in the first case of Alzheimer's disease*. *The Lancet Neurology*, 2013. **12**(2): p. 129-130.
7. Fassbender, K. and L. Frölich, *Leitlinien zur „Pharmakotherapie neurodegenerativer Demenzen“*. *Nervenarzt*, 2014. **85**(12): p. 1589-1600.
8. Gozes, I., *Tau pathology: predictive diagnostics, targeted preventive and personalized medicine and application of advanced research in medical practice*. *EPMA Journal*, 2010. **1**(2): p. 305-316.
9. Hyman, B.T., C.H. Phelps, T.G. Beach, E.H. Bigio, N.J. Cairns, M.C. Carrillo, D.W. Dickson, C. Duyckaerts, M.P. Frosch, E. Masliah, S.S. Mirra, P.T. Nelson, J.A. Schneider, D.R. Thal, B. Thies, J.Q. Trojanowski, H.V. Vinters, and T.J. Montine, *National Institute on Aging-Alzheimer's Association guidelines for the neuropathologic assessment of Alzheimer's disease*.

- Alzheimer's & Dementia: The Journal of the Alzheimer's Association, 2012. **8**(1): p. 1-13.
10. Jack, C.R., Jr., D.A. Bennett, K. Blennow, M.C. Carrillo, B. Dunn, S.B. Haeberlein, D.M. Holtzman, W. Jagust, F. Jessen, J. Karlawish, E. Liu, J.L. Molinuevo, T. Montine, C. Phelps, K.P. Rankin, C.C. Rowe, P. Scheltens, E. Siemers, H.M. Snyder, R. Sperling, C. Elliott, E. Masliah, L. Ryan, and N. Silverberg, *NIA-AA Research Framework: Toward a biological definition of Alzheimer's disease*. Alzheimer's & Dementia: The Journal of the Alzheimer's Association, 2018. **14**(4): p. 535-562.
 11. Ossenkoppele, R., N. Mattsson, C.E. Teunissen, F. Barkhof, Y. Pijnenburg, P. Scheltens, W.M. van der Flier, and G.D. Rabinovici, *Cerebrospinal fluid biomarkers and cerebral atrophy in distinct clinical variants of probable Alzheimer's disease*. Neurobiology of Aging, 2015. **36**(8): p. 2340-2347.
 12. Schneider, L.S., F. Mangialasche, N. Andreasen, H. Feldman, E. Giacobini, R. Jones, V. Mantua, P. Mecocci, L. Pani, B. Winblad, and M. Kivipelto, *Clinical trials and late-stage drug development for Alzheimer's disease: an appraisal from 1984 to 2014*. Journal of Internal Medicine, 2014. **275**(3): p. 251-283.
 13. Reitz, C., C. Brayne, and R. Mayeux, *Epidemiology of Alzheimer disease*. Nature reviews. Neurology., 2011. **7**(3): p. 137-152.
 14. Robinson, J.L., M.M. Corrada, G.G. Kovacs, M. Dominique, C. Caswell, S.X. Xie, V.M.Y. Lee, C.H. Kawas, and J.Q. Trojanowski, *Non-Alzheimer's contributions to dementia and cognitive resilience in The 90+ Study*. Acta Neuropathologica, 2018. **136**(3): p. 377-388.
 15. Robinson, J.L., E.B. Lee, S.X. Xie, L. Rennert, E. Suh, C. Bredenberg, C. Caswell, V.M. Van Deerlin, N. Yan, A. Yousef, H.I. Hurtig, A. Siderowf, M. Grossman, C.T. McMillan, B. Miller, J.E. Duda, D.J. Irwin, D. Wolk, L. Elman, L. McCluskey, A. Chen-Plotkin, D. Weintraub, S.E. Arnold, J. Brettschneider, V.M. Lee, and J.Q. Trojanowski, *Neurodegenerative disease concomitant proteinopathies are prevalent, age-related and APOE4-associated*. Brain, 2018. **141**(7): p. 2181-2193.

16. Solodkin, A., J. Zimmermann, A.R. McIntosh, L. Stefanovski, and P. Ritter, *Neurological Biomarkers and Neuroinformatics: The Role of The Virtual Brain*, in *Molecular-Genetic and Statistical Techniques for Behavioral and Neural Research*, R.T. Gerlai, Editor. 2018, Academic Press: San Diego. p. 3-30.
17. Stefanovski, L., A. Ghani, A.R. McIntosh, and P. Ritter, *Linking connectomics and dynamics in the human brain*. *Neuroforum*, 2016. **22**(3): p. 64-70.
18. Sanz Leon, P., S.A. Knock, M.M. Woodman, L. Domide, J. Mersmann, A.R. McIntosh, and V. Jirsa, *The Virtual Brain: a simulator of primate brain network dynamics*. *Frontiers in Neuroinformatics*, 2013. **7**(10).
19. Ritter, P., M. Schirner, A.R. McIntosh, and V.K. Jirsa, *The virtual brain integrates computational modeling and multimodal neuroimaging*. *Brain Connectivity*, 2013. **3**(2): p. 121-145.
20. Sanz-Leon, P., S.A. Knock, A. Spiegler, and V.K. Jirsa, *Mathematical framework for large-scale brain network modeling in The Virtual Brain*. *NeuroImage*, 2015. **111**: p. 385-430.
21. Schirner, M., S. Rothmeier, V.K. Jirsa, A.R. McIntosh, and P. Ritter, *An automated pipeline for constructing personalized virtual brains from multimodal neuroimaging data*. *NeuroImage*, 2015. **117**: p. 343-357.
22. Spiegler, A., T.R. Knösche, K. Schwab, J. Haueisen, and F.M. Atay, *Modeling Brain Resonance Phenomena Using a Neural Mass Model*. *PLOS Computational Biology*, 2011. **7**(12): p. e1002298.
23. Liley, D.T., P.J. Cadusch, and M.P. Dafilis, *A spatially continuous mean field theory of electrocortical activity*. *Network: Computation in Neural Systems*, 2002. **13**(1): p. 67-113.
24. Jansen, B.H. and V.G. Rit, *Electroencephalogram and visual evoked potential generation in a mathematical model of coupled cortical columns*. *Biological Cybernetics*, 1995. **73**(4): p. 357-66.

25. Spiegler, A., S.J. Kiebel, F.M. Atay, and T.R. Knösche, *Bifurcation analysis of neural mass models: Impact of extrinsic inputs and dendritic time constants*. *NeuroImage*, 2010. **52**(3): p. 1041-1058.
26. Sadigh-Eteghad, S., B. Sabermarouf, A. Majdi, M. Talebi, M. Farhoudi, and J. Mahmoudi, *Amyloid-Beta: A Crucial Factor in Alzheimer's Disease*. *Medical Principles and Practice*, 2015. **24**(1): p. 1-10.
27. Li, S., S. Hong, N.E. Shepardson, D.M. Walsh, G.M. Shankar, and D. Selkoe, *Soluble oligomers of amyloid Beta protein facilitate hippocampal long-term depression by disrupting neuronal glutamate uptake*. *Neuron*, 2009. **62**(6): p. 788-801.
28. Furukawa, K., S.W. Barger, E.M. Blalock, and M.P. Mattson, *Activation of K⁺ channels and suppression of neuronal activity by secreted beta-amyloid-precursor protein*. *Nature*, 1996. **379**(6560): p. 74-78.
29. Ripoli, C., S. Cocco, D.D. Li Puma, R. Piacentini, A. Mastrodonato, F. Scala, D. Puzzo, M. D'Ascenzo, and C. Grassi, *Intracellular Accumulation of Amyloid- β (A β) Protein Plays a Major Role in A β -Induced Alterations of Glutamatergic Synaptic Transmission and Plasticity*. *The Journal of Neuroscience*, 2014. **34**(38): p. 12893-12903.
30. Ulrich, D., *Amyloid-beta Impairs Synaptic Inhibition via GABA(A) Receptor Endocytosis*. *The Journal of Neuroscience*, 2015. **35**(24): p. 9205-9210.
31. Ren, S.-Q., W. Yao, J.-Z. Yan, C. Jin, J.-J. Yin, J. Yuan, S. Yu, and Z. Cheng, *Amyloid β causes excitation/inhibition imbalance through dopamine receptor 1-dependent disruption of fast-spiking GABAergic input in anterior cingulate cortex*. *Scientific Reports*, 2018. **8**(1): p. 1-10.
32. Miyauchi, T., H. Hagimoto, M. Ishii, S. Endo, K. Tanaka, S. Kajiwara, K. Endo, A. Kajiwara, and K. Kosaka, *Quantitative EEG in patients with presenile and senile dementia of the Alzheimer type*. *Acta Neurologica Scandinavica*, 1994. **89**(1): p. 56-64.

33. Rice, D.M., M.S. Buchsbaum, A. Starr, L. Auslander, J. Hagman, and W.J. Evans, *Abnormal EEG slow activity in left temporal areas in senile dementia of the Alzheimer type*. *Journal of Gerontology*, 1990. **45**(4): p. 145-151.
34. Weiner, M.W., D.P. Veitch, P.S. Aisen, L.A. Beckett, N.J. Cairns, R.C. Green, D. Harvey, C.R. Jack, Jr., W. Jagust, J.C. Morris, R.C. Petersen, J. Salazar, A.J. Saykin, L.M. Shaw, A.W. Toga, and J.Q. Trojanowski, *The Alzheimer's Disease Neuroimaging Initiative 3: Continued innovation for clinical trial improvement*. *Alzheimer's & Dementia: The Journal of the Alzheimer's Association*, 2017. **13**(5): p. 561-571.
35. Choi, S.R., G. Golding, Z. Zhuang, W. Zhang, N. Lim, F. Hefti, T.E. Benedum, M.R. Kilbourn, D. Skovronsky, and H.F. Kung, *Preclinical properties of 18F-AV-45: a PET agent for A β plaques in the brain*. *Journal of Nuclear Medicine*, 2009. **50**(11): p. 1887-1894.
36. Phelps, M.E., *Positron emission tomography provides molecular imaging of biological processes*. *Proceedings of the National Academy of Sciences*, 2000. **97**(16): p. 9226-9233.
37. Glasser, M.F., S.N. Sotiropoulos, J.A. Wilson, T.S. Coalson, B. Fischl, J.L. Andersson, J. Xu, S. Jbabdi, M. Webster, J.R. Polimeni, D.C. Van Essen, and M. Jenkinson, *The minimal preprocessing pipelines for the Human Connectome Project*. *NeuroImage*, 2013. **80**: p. 105-124.
38. Glasser, M.F., T.S. Coalson, E.C. Robinson, C.D. Hacker, J. Harwell, E. Yacoub, K. Ugurbil, J. Andersson, C.F. Beckmann, M. Jenkinson, S.M. Smith, and D.C. Van Essen, *A multi-modal parcellation of human cerebral cortex*. *Nature*, 2016. **536**(7615): p. 171-178.
39. Tadel, F., S. Baillet, J.C. Mosher, D. Pantazis, and R.M. Leahy, *Brainstorm: A User-Friendly Application for MEG/EEG Analysis*. *Computational Intelligence and Neuroscience*, 2011. **2011**: p. 1-13.
40. Bullmore, E. and O. Sporns, *Complex brain networks: graph theoretical analysis of structural and functional systems*. *Nature Reviews. Neuroscience*, 2009. **10**(3): p. 186-198.

41. Euler, L., *Solutio problematis ad geometriam situs pertinentis*. Commentarii academiae scientiarum Petropolitanae, 1741: p. 128-140.
42. Miller, K.L., F. Alfaro-Almagro, N.K. Bangerter, D.L. Thomas, E. Yacoub, J. Xu, A.J. Bartsch, S. Jbabdi, S.N. Sotiropoulos, J.L. Andersson, L. Griffanti, G. Douaud, T.W. Okell, P. Weale, I. Dragonu, S. Garratt, S. Hudson, R. Collins, M. Jenkinson, P.M. Matthews, and S.M. Smith, *Multimodal population brain imaging in the UK Biobank prospective epidemiological study*. Nature Neuroscience, 2016. **19**(11): p. 1523-1536.
43. Alfaro-Almagro, F., M. Jenkinson, N.K. Bangerter, J.L.R. Andersson, L. Griffanti, G. Douaud, S.N. Sotiropoulos, S. Jbabdi, M. Hernandez-Fernandez, E. Vallee, D. Vidaurre, M. Webster, P. McCarthy, C. Rorden, A. Daducci, D.C. Alexander, H. Zhang, I. Dragonu, P.M. Matthews, K.L. Miller, and S.M. Smith, *Image processing and Quality Control for the first 10,000 brain imaging datasets from UK Biobank*. NeuroImage, 2018. **166**: p. 400-424.
44. Hofmann-Apitius, M., M.E. Alarcon-Riquelme, C. Chamberlain, and D. McHale, *Towards the taxonomy of human disease*. Nature Reviews. Drug Discovery, 2015. **14**(2): p. 75-76.
45. Iyappan, A., M. Gundel, M. Shahid, J. Wang, H. Li, H.T. Mevissen, B. Muller, J. Fluck, V. Jirsa, L. Domide, E. Younesi, and M. Hofmann-Apitius, *Towards a Pathway Inventory of the Human Brain for Modeling Disease Mechanisms Underlying Neurodegeneration*. Journal of Alzheimer's Disease, 2016. **52**(4): p. 1343-1360.

EIDESSTATTLICHE VERSICHERUNG

„Ich, Leon Stefanovski, versichere an Eides statt durch meine eigenhändige Unterschrift, dass ich die vorgelegte Dissertation mit dem Thema: „Amyloid-basierte Gehirnsimulation der Alzheimer-Krankheit mit The Virtual Brain“ bzw. „Amyloid-based brain simulation of Alzheimer’s Disease with The Virtual Brain“ selbstständig und ohne nicht offengelegte Hilfe Dritter verfasst und keine anderen als die angegebenen Quellen und Hilfsmittel genutzt habe.

Alle Stellen, die wörtlich oder dem Sinne nach auf Publikationen oder Vorträgen anderer Autoren/innen beruhen, sind als solche in korrekter Zitierung kenntlich gemacht. Die Abschnitte zu Methodik (insbesondere praktische Arbeiten, Laborbestimmungen, statistische Aufarbeitung) und Resultaten (insbesondere Abbildungen, Graphiken und Tabellen) werden von mir verantwortet.

Ich versichere ferner, dass ich die in Zusammenarbeit mit anderen Personen generierten Daten, Datenauswertungen und Schlussfolgerungen korrekt gekennzeichnet und meinen eigenen Beitrag sowie die Beiträge anderer Personen korrekt kenntlich gemacht habe (siehe Anteilserklärung). Texte oder Textteile, die gemeinsam mit anderen erstellt oder verwendet wurden, habe ich korrekt kenntlich gemacht.

Meine Anteile an etwaigen Publikationen zu dieser Dissertation entsprechen denen, die in der untenstehenden gemeinsamen Erklärung mit der Erstbetreuerin, angegeben sind. Für sämtliche im Rahmen der Dissertation entstandenen Publikationen wurden die Richtlinien des ICMJE (International Committee of Medical Journal Editors; www.icmje.org) zur Autorenschaft eingehalten. Ich erkläre ferner, dass ich mich zur Einhaltung der Satzung der Charité – Universitätsmedizin Berlin zur Sicherung Guter Wissenschaftlicher Praxis verpflichte.

Weiterhin versichere ich, dass ich diese Dissertation weder in gleicher noch in ähnlicher Form bereits an einer anderen Fakultät eingereicht habe.

Die Bedeutung dieser eidesstattlichen Versicherung und die strafrechtlichen Folgen einer unwahren eidesstattlichen Versicherung (§§156, 161 des Strafgesetzbuches) sind mir bekannt und bewusst.“

Datum

Unterschrift

ANTEILSERKLÄRUNG

Ich hatte folgenden Anteil an der angefügten Originalpublikation:

Stefanovski, L., P. Triebkorn, A. Spiegler, M.-A. Diaz-Cortes, A. Solodkin, V. Jirsa, A. R. McIntosh and P. Ritter for the Alzheimer's Disease Neuroimaging Initiative (2019). "Linking Molecular Pathways and Large-Scale Computational Modeling to Assess Candidate Disease Mechanisms and Pharmacodynamics in Alzheimer's Disease." Frontiers in Computational Neuroscience **13**(54).

In der Originalpublikation „Linking Molecular Pathways and Large-Scale Computational Modeling to Assess Candidate Disease Mechanisms and Pharmacodynamics in Alzheimer's Disease“ entwickelte ich zusammen mit Prof. Ritter die Idee und das Konzept der Studie, also die Erweiterung des bestehenden Modells um eine sigmoidale Transferfunktion, welche den Effekt des Beta-Amyloids modelliert. Gemeinsam mit Paul Triebkorn, Andreas Spiegler und Prof. Ritter entwickelte ich hauptverantwortlich die mathematische und informatische Umsetzung der Grundidee der Studie in den entsprechenden Gleichungen und Codes sowie das Konzept der virtuellen Therapie mit Memantin.

Die Präprozessierung der Bildgebungsdaten in Vorbereitung auf ihre Nutzung zur Simulation sowie die Einrichtung der Netzwerkarchitektur zur Nutzung eines Supercomputers für die Simulation wurde von Paul Triebkorn übernommen.

Ich zeichne hauptverantwortlich für das Verfassen des gesamten Manuskriptes, die Auswertung, Analyse und Interpretation der Simulationsergebnisse. Im Einzelnen war ich alleine und selbstständig hauptverantwortlich für folgende Aspekte:

- Analyse und Auswahl der empirischen Daten aus ADNI
- Entwicklung des Konzeptes und Berechnung der Standardisierung der SC sowie deren graphentheoretische Analyse
- Spektralanalyse mittels Fourier-Transformation der simulierten Zeitserien
- Entwicklung und Berechnung der dreidimensionalen Histogramme zur Darstellung der dominanten Frequenzen in Abhängigkeit von G (Abbildungen 5G-J, 6B, 6F, 6J, Supplementary Figures 3, 4 und 6A)

- Interpretation der Bifurkationsdiagramme aus Abbildung 6 sowie Entwicklung des Konzeptes zur Verknüpfung dieser mit den Ergebnissen
- Berechnung, statistische Auswertung und Interpretation der Frequenzunterschiede zwischen den Diagnosegruppen im simulierten EEG sowie dem lokalen Feldpotential (LFP) bei empirischer sowie bei homogener Verteilung von Abeta (Abbildung 7)
- Berechnung, Regressionsanalyse und Interpretation der Frequenzabhängigkeit von der lokalen Abeta-Konzentration, jeweils für alle Diagnosegruppen (Abbildung 8)
- Indirekte Parameterraumexploration (mittels der Simulationsdaten aus Zufallsverteilungen von Abeta) zwischen dem globalen Skalierungsfaktor G sowie der inhibitorischen Zeitkonstante τ_i bezüglich der resultierenden dominanten Frequenz im LFP (Abbildung 9)
- Graphentheoretische Verortung und Interpretation der simulierten Frequenzen, der empirischen Abeta-Verteilung, des Effektes des virtuellen Memantins sowie der lokalen Hyperexzitation, sowie statistische Auswertung und Interpretation (Abbildungen 10 sowie 11E-F und 12 E-G)
- Berechnung und Auswertung der Ergebnisse der virtuellen Therapie mit Memantin hinsichtlich der resultierenden Frequenzen im simulierten EEG sowie der räumlichen Verteilung des Effektes sowie deren Interpretation im Hinblick auf die Gleichgewichtsmannigfaltigkeiten des Systems (Abbildung 11)
- Konzeption und Berechnung der relativen Hyperexzitation sowie deren Auswertung für alle Diagnosegruppen, und eine Abeta-unabhängige Kontrollsimulation (Abbildung 12)
- Kritische Bewertung des gewählten Modells mithilfe der Gleichgewichtsmannigfaltigkeiten des Systems in Abhängigkeit von Abeta sowie Verortung in einer übergeordneten Theorie zur Wirkungsweise des gewählten Modells (Abbildung 13)
- Berechnung und Auswertung der Kontrollsimulation ohne und mit maximaler Belastung von Abeta (Supplementary Figure 3)
- Konzeption, Berechnung und Auswertung von Kontrollsimulationen mit zufälliger Verteilung von Abeta (Supplementary Figure 5)
- Verortung der Frequenzunterschiede zwischen den einzelnen Studienteilnehmer in Abhängigkeit von der Zugehörigkeit einzelner beteiligter

Hirnregionen zu den Grenzyklen des Jansen-Rit-Modells (Supplementary Figure 6)

- Auswahl und Durchführung aller statistischen Tests (vgl. Supplementary Table 8)

Darüber hinaus erstellte ich selbstständig alle Abbildungen der Publikation, mit folgenden Ausnahmen:

- Abbildungen 2B-C, 6A, 6E, 6I, 11A-C und 13 A-D (zur Verfügung gestellt von Andreas Spiegler und daraufhin modifiziert und in den Kontext der gesamten Abbildung eingebunden)
- Supplementary Figures 1 und 2 (mit Erlaubnis der Rechteinhaber zitiert und wiederverwendet aus einer anderen Publikation)

Eine Stellungnahme zu den Anteilen der Autoren findet sich auch veröffentlicht in der Originalpublikation auf Seite 23.

Unterschrift des Doktoranden

AUSZUG AUS DER JOURNAL SUMMARY LIST (ISI WEB OF KNOWLEDGE)

Journal Data Filtered By: **Selected JCR Year: 2017** Selected Editions: SCIE,SSCI
 Selected Categories: **"NEUROSCIENCES"** Selected Category Scheme: WoS
Gesamtanzahl: 261 Journale

Rank	Full Journal Title	Total Cites	Journal Impact Factor	Eigenfactor Score
1	NATURE REVIEWS NEUROSCIENCE	40,834	32.635	0.069940
2	NATURE NEUROSCIENCE	59,426	19.912	0.153710
3	ACTA NEUROPATHOLOGICA	18,783	15.872	0.041490
4	TRENDS IN COGNITIVE SCIENCES	25,391	15.557	0.040790
5	BEHAVIORAL AND BRAIN SCIENCES	8,900	15.071	0.010130
6	Annual Review of Neuroscience	13,320	14.675	0.016110
7	NEURON	89,410	14.318	0.216730
8	PROGRESS IN NEUROBIOLOGY	13,065	14.163	0.015550
9	BIOLOGICAL PSYCHIATRY	42,494	11.982	0.056910
10	MOLECULAR PSYCHIATRY	18,460	11.640	0.047200
11	JOURNAL OF PINEAL RESEARCH	9,079	11.613	0.008600
12	TRENDS IN NEUROSCIENCES	20,061	11.439	0.026860
13	BRAIN	52,061	10.840	0.075170
14	SLEEP MEDICINE REVIEWS	6,080	10.602	0.010720
15	ANNALS OF NEUROLOGY	37,251	10.244	0.053390
16	Translational Stroke Research	2,202	8.266	0.005260
17	NEUROSCIENCE AND BIOBEHAVIORAL REVIEWS	24,279	8.037	0.048460
18	NEUROSCIENTIST	4,738	7.461	0.008730
19	NEURAL NETWORKS	10,086	7.197	0.015290
20	FRONTIERS IN NEUROENDOCRINOLOGY	3,924	6.875	0.006040
21	NEUROPSYCHOPHARMACOLOGY	24,537	6.544	0.042870
22	CURRENT OPINION IN NEUROBIOLOGY	14,190	6.541	0.034670
23	Molecular Neurodegeneration	3,489	6.426	0.009850
24	CEREBRAL CORTEX	29,570	6.308	0.058970
25	BRAIN BEHAVIOR AND IMMUNITY	12,583	6.306	0.026850
26	BRAIN PATHOLOGY	4,952	6.187	0.007750
27	Brain Stimulation	4,263	6.120	0.014510
28	NEUROPATHOLOGY AND APPLIED NEUROBIOLOGY	3,654	6.059	0.006350
29	JOURNAL OF CEREBRAL BLOOD FLOW AND METABOLISM	19,450	6.045	0.028280
30	JOURNAL OF NEUROSCIENCE	176,157	5.970	0.265950
31	Molecular Autism	1,679	5.872	0.006320
31	Translational Neurodegeneration	589	5.872	0.002280
33	GLIA	13,417	5.846	0.020530
34	Neurotherapeutics	3,973	5.719	0.008980
35	PAIN	36,132	5.559	0.038000
36	NEUROIMAGE	92,719	5.426	0.152610
37	Acta Neuropathologica Communications	2,326	5.414	0.011550
38	Multiple Sclerosis Journal	10,675	5.280	0.021890

1

Selected JCR Year: 2017; Selected Categories: "NEUROSCIENCES"

[...]

Rank	Full Journal Title	Total Cites	Journal Impact Factor	Eigenfactor Score
165	PHARMACOLOGY BIOCHEMISTRY AND BEHAVIOR	12,203	2.538	0.010510
166	BEHAVIORAL NEUROSCIENCE	7,111	2.507	0.004730
167	JOURNAL OF NEUROPHYSIOLOGY	43,471	2.502	0.041080
168	MUSCLE & NERVE	11,441	2.496	0.014410
169	INTERNATIONAL JOURNAL OF DEVELOPMENTAL NEUROSCIENCE	3,417	2.495	0.004450
170	NEUROMUSCULAR DISORDERS	4,725	2.487	0.008920
171	JOURNAL OF MOLECULAR NEUROSCIENCE	5,071	2.454	0.009050
172	Behavioral and Brain Functions	1,573	2.449	0.002360
173	JOURNAL OF THE NEUROLOGICAL SCIENCES	17,095	2.448	0.023150
174	METABOLIC BRAIN DISEASE	2,562	2.441	0.004930
175	Journal of Mathematical Neuroscience	186	2.414	0.001190
176	International Review of Neurobiology	2,551	2.371	0.003450
177	SYNAPSE	4,109	2.360	0.003110
178	ACTA NEUROPSYCHIATRICA	746	2.333	0.001520
179	NEUROLOGICAL SCIENCES	5,047	2.285	0.008870
180	NEUROSCIENCE RESEARCH	4,924	2.277	0.005340
181	GAIT & POSTURE	12,927	2.273	0.016950
182	NEUROIMMUNOMODULATION	1,369	2.238	0.001620
183	Neural Regeneration Research	2,801	2.234	0.007510
184	Brain and Behavior	1,351	2.219	0.005440
185	BMC NEUROSCIENCE	4,804	2.173	0.007190
186	NEUROLOGY INDIA	2,231	2.166	0.002000
187	JOURNAL OF CHEMICAL NEUROANATOMY	2,227	2.162	0.001940
188	NEUROSCIENCE LETTERS	33,322	2.159	0.029770
189	DEVELOPMENTAL NEUROSCIENCE	2,262	2.133	0.002370
190	Neural Development	968	2.130	0.002440
191	RESTORATIVE NEUROLOGY AND NEUROSCIENCE	2,096	2.101	0.003180
192	Clinical Psychopharmacology and Neuroscience	436	2.090	0.001360
193	CNS & Neurological Disorders-Drug Targets	2,625	2.084	0.005300
194	AUDIOLOGY AND NEURO-OTOLOGY	1,792	2.078	0.002440
195	Frontiers in Computational Neuroscience	2,173	2.073	0.008820
196	ACTA NEUROLOGICA BELGICA	959	2.072	0.001720
197	VISION RESEARCH	15,754	2.069	0.010430
198	BRAIN INJURY	6,172	2.061	0.008150
199	NEUROPHYSIOLOGIE CLINIQUE-CLINICAL NEUROPHYSIOLOGY	1,303	2.045	0.001450

6

Selected JCR Year: 2017; Selected Categories: "NEUROSCIENCES"

DRUCKEXEMPLAR DER ORIGINALPUBLIKATION

Stefanovski, L., P. Triebkorn, A. Spiegler, M.-A. Diaz-Cortes, A. Solodkin, V. Jirsa, A.R. McIntosh and P. Ritter for the Alzheimer's Disease Neuroimaging Initiative, *Linking Molecular Pathways and Large-Scale Computational Modeling to Assess Candidate Disease Mechanisms and Pharmacodynamics in Alzheimer's Disease*. Frontiers in Computational Neuroscience, 2019. **13**(54).

<https://doi.org/10.3389/fncom.2019.00054>



Linking Molecular Pathways and Large-Scale Computational Modeling to Assess Candidate Disease Mechanisms and Pharmacodynamics in Alzheimer's Disease

OPEN ACCESS

Edited by:

Anke Meyer-Baese,
Florida State University, United States

Reviewed by:

Li Su,
University of Cambridge,
United Kingdom
Alle Meije Wink,
VU University Medical
Center, Netherlands

*Correspondence:

Leon Stefanovski
leon.stefanovski@charite.de

[†]Data used in preparation of this article were obtained from the Alzheimer's Disease Neuroimaging Initiative (ADNI) database (adni.loni.usc.edu). As such, the investigators within the ADNI contributed to the design and implementation of ADNI and/or provided data but did not participate in analysis or writing of this report. A complete listing of ADNI investigators can be found at: https://adni.loni.usc.edu/wp-content/uploads/how_to_apply/ADNI_Acknowledgement_List.pdf

Received: 01 April 2019

Accepted: 22 July 2019

Published: 13 August 2019

Citation:

Stefanovski L, Triebkorn P, Spiegler A, Diaz-Cortes M-A, Solodkin A, Jirsa V, McIntosh RA and Ritter P (2019) Linking Molecular Pathways and Large-Scale Computational Modeling to Assess Candidate Disease Mechanisms and Pharmacodynamics in Alzheimer's Disease. *Front. Comput. Neurosci.* 13:54. doi: 10.3389/fncom.2019.00054

Leon Stefanovski^{1,2*}, Paul Triebkorn^{1,2}, Andreas Spiegler^{1,2}, Margarita-Arimatea Diaz-Cortes^{1,2,3}, Ana Solodkin⁴, Viktor Jirsa⁵, Anthony Randal McIntosh⁶ and Petra Ritter^{1,2,7} for the Alzheimer's Disease Neuroimaging Initiative[†]

¹ Charité—Universitätsmedizin Berlin, Corporate Member of Freie Universität Berlin, Humboldt-Universität zu Berlin, and Berlin Institute of Health, Department of Neurology, Brain Simulation Section, Berlin, Germany, ² Berlin Institute of Health, Berlin, Germany, ³ Institut für Informatik, Freie Universität Berlin, Berlin, Germany, ⁴ Behavioral and Brain Sciences, University of Texas at Dallas, Dallas, TX, United States, ⁵ Institut de Neurosciences des Systèmes, Aix Marseille Université, Marseille, France, ⁶ Baycrest Health Sciences, Rotman Research Institute, Toronto, ON, Canada, ⁷ Bernstein Center for Computational Neuroscience Berlin, Berlin, Germany

Introduction: While the prevalence of neurodegenerative diseases associated with dementia such as Alzheimer's disease (AD) increases, our knowledge on the underlying mechanisms, outcome predictors, or therapeutic targets is limited. In this work, we demonstrate how computational multi-scale brain modeling links phenomena of different scales and therefore identifies potential disease mechanisms leading the way to improved diagnostics and treatment.

Methods: The Virtual Brain (TVB; thevirtualbrain.org) neuroinformatics platform allows standardized large-scale structural connectivity-based simulations of whole brain dynamics. We provide proof of concept for a novel approach that quantitatively links the effects of altered molecular pathways onto neuronal population dynamics. As a novelty, we connect chemical compounds measured with positron emission tomography (PET) with neural function in TVB addressing the phenomenon of hyperexcitability in AD related to the protein amyloid beta (Abeta). We construct personalized virtual brains based on an averaged healthy connectome and individual PET derived distributions of Abeta in patients with mild cognitive impairment (MCI, $N = 8$) and Alzheimer's Disease (AD, $N = 10$) and in age-matched healthy controls (HC, $N = 15$) using data from ADNI-3 data base (<http://adni.loni.usc.edu>). In the personalized virtual brains, individual Abeta burden modulates regional Excitation-Inhibition balance, leading to local hyperexcitation with high Abeta loads. We analyze simulated regional neural activity and electroencephalograms (EEG).

Results: Known empirical alterations of EEG in patients with AD compared to HCs were reproduced by simulations. The virtual AD group showed slower frequencies in simulated local field potentials and EEG compared to MCI and HC groups. The heterogeneity

of the Abeta load is crucial for the virtual EEG slowing which is absent for control models with homogeneous Abeta distributions. Slowing phenomena primarily affect the network hubs, independent of the spatial distribution of Abeta. Modeling the N-methyl-D-aspartate (NMDA) receptor antagonism of memantine in local population models, reveals potential functional reversibility of the observed large-scale alterations (reflected by EEG slowing) in virtual AD brains.

Discussion: We demonstrate how TVB enables the simulation of systems effects caused by pathogenetic molecular candidate mechanisms in human virtual brains.

Keywords: Alzheimer's disease, The Virtual Brain, PET, beta amyloid, EEG, MRI, memantine, personalized medicine

INTRODUCTION

Neurodegenerative diseases (NDD) gain increasing socio-economic relevance due to an aging society (WHO, 2011; Wimo et al., 2011, 2017; Xu et al., 2017). The Alzheimer's Association's latest report estimates the yearly cost of Alzheimer's disease (AD) treatment in the U.S. at \$277 billion (Alzheimer's Association, 2018). By 2050 this number is expected to rise as high as \$1.1 trillion. According to the report, early diagnosis could save up to \$7.9 trillion in cumulated medical and care costs by the year 2050. While the prevalence of AD—the most common cause of dementia and the most common NDD in general—increases, its cause is still not understood, nor is there a cure. Our understanding of their pathogenesis and classification remain insufficient. Therefore, we aim to integrate clinical data from molecular biology and neurology, using nonlinear systems theory. Our aim is to build predictive models for health-outcome and cognitive function by individual virtual brain simulations using The Virtual Brain (TVB; thevirtualbrain.org) platform (Ritter et al., 2013; Sanz Leon et al., 2013). TVB integrates various empirical data in computational models of the brain that allow for the identification of neurobiological processes that are more directly linked to the causal disease mechanisms than the measured empirical data. Biomedical sciences are currently lacking a mapping between the degree and facets of cognitive impairments, biomarkers from high-throughput technologies, and the underlying causal origins of NDD like AD. The imperative for the field is to identify the features of brain network function in NDD that predict whether a person will develop dementia. The heterogeneity of NDD makes it difficult to develop robust predictions of cognitive decline. This can be addressed by large prospective studies where there is potential for participants to develop NDD. It is difficult in general to predict individual disease progression and this is a particular challenge in complex nonlinear systems, like the brain, where emergent features at one level of organization (e.g., cognitive function) can come about through the complex interaction of subordinate features (e.g., network dynamics, molecular pathways, gene expression). The Virtual Brain takes into account the principles of complex adaptive systems and hence poses a promising tool for identifying mechanistic predictive biomarkers for NDD. Due to the high dimensionality of brain models and the even greater

complexity of the to-be-simulated brain states, selecting the used modeling approach carefully for a specific question of interest is essential.

The candidate biological mechanism under investigation in the present study is related to amyloid beta (Abeta), a protein that is an oligomeric cleavage product of the physiological amyloid precursor protein (APP) (Bloom, 2014; Selkoe and Hardy, 2016). The soluble oligomers have the tendency for polymerization (Sadigh-Eteghad et al., 2015; Selkoe and Hardy, 2016). Due to their non-physiological configuration they aggregate and accumulates in brain tissue—a process that starts already in early preclinical stages of AD, i.e., many years before the onset of symptoms—typically in the fifth decade of life (Braak and Braak, 1997)—as shown in rodent models (Busche et al., 2012) and human studies (Klunk et al., 2007; Jack et al., 2009). Aggregated Abeta and its intermediates, soluble Abeta oligomers, can act directly neurotoxic (Hardy and Selkoe, 2002; Prasansuklab and Tencomnao, 2013; Selkoe and Hardy, 2016) and have been found intra- or extra-cellularly (Hardy and Selkoe, 2002; Walsh and Selkoe, 2007; Selkoe and Hardy, 2016). Those findings led to the hypothesis that the deposition of Abeta poses an initial step in the pathology of AD while Abeta has been suggested as a key feature in the pathogenesis of AD leading to major changes in the functionality and structure of the brain (Klunk et al., 2007; Jack et al., 2009; Villemagne et al., 2009). The goal of the present study is to incorporate the hypothesized qualitative and quantitative effects of Abeta on neuronal population dynamics into our brain network models, i.e., adding mathematical models that describe how molecular changes alter population activity—so called cause-and-effect models. We will focus here on the disrupted inhibitory function of interneurons and consecutive hyperexcitability caused by Abeta—while we are aware of various other factors with potential roles for AD etiology, such as vascular changes (Love and Miners, 2016; Storck and Pietrzik Claus, 2018; Bannai et al., 2019), neuroinflammation (Heneka et al., 2015a,b; Wang and Colonna, 2019; Zhou et al., 2019), genetics (Mahley, 2016; Hudry et al., 2019; Takatori et al., 2019), environmental factors (Alonso et al., 2018; McLachlan et al., 2019) and concomitant proteinopathies others than Abeta pathology (Robinson et al., 2018a,b). Beside Abeta there is a second molecular hallmark associated with the pathogenesis of AD: the phosphorylated Tau “tubulin-associated unit” protein

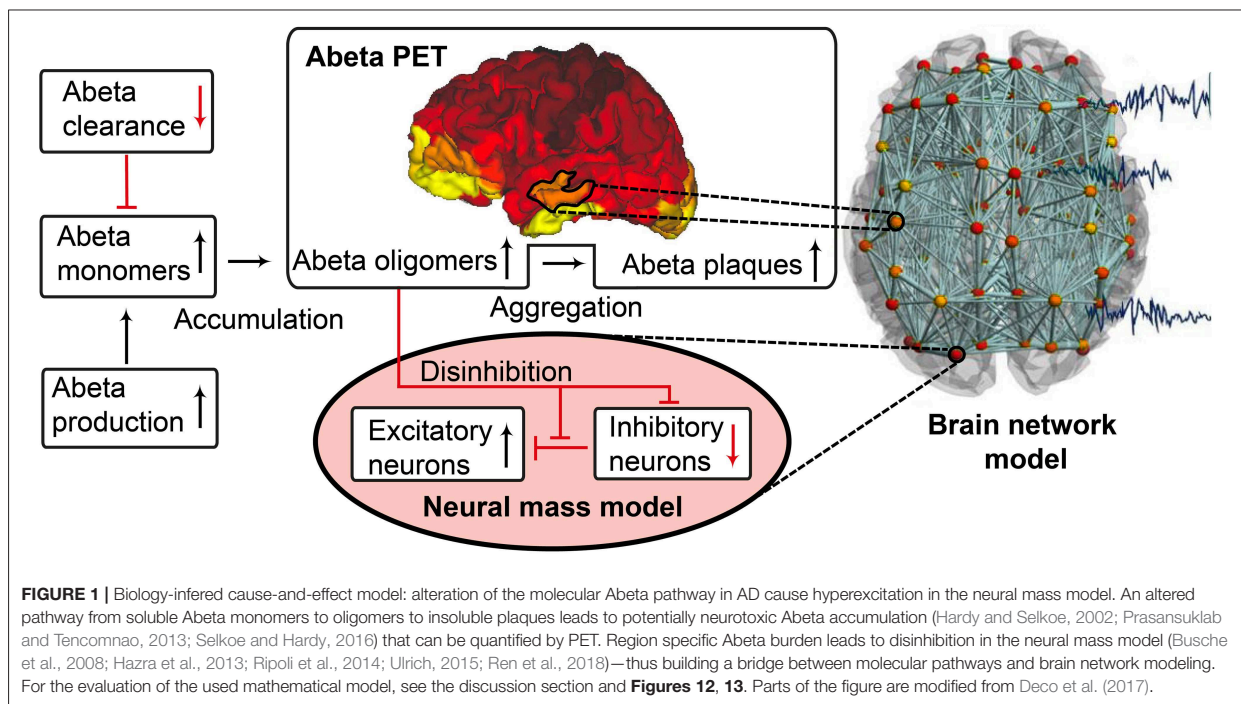
(Bloom, 2014; Guo et al., 2017; Tapia-Rojas et al., 2019) which contributes to microtubule stability in the neural cytoskeleton (Guo et al., 2017). One major argument in favor of the more prominent involvement of Abeta in the pathogenesis of AD, in contrast to Tau, is its higher specificity to AD and its appearance in the early familial variants of AD, where the molecular pathway is better understood (Blennow et al., 2006; Klunk et al., 2007; Villemagne et al., 2009). Therefore, most therapeutic strategies in the past targeted Abeta. Yet recently three clinical trials with antibodies against Abeta had to be terminated in phase III: aducanumab (Biogen, 2019; Chiao et al., 2019), crenezumab (Salloway et al., 2018; Roche, 2019), and solanezumab (Doggrell, 2018; Honig et al., 2018) did not meet the expectations to act in a disease-modifying manner slowing down the cognitive decline (Selkoe and Hardy, 2016). Nevertheless, there are still studies ongoing, e.g., with BAN-2401, an antibody against soluble monomeric Abeta protofibrils (as aducanumab) (Logovinsky et al., 2016; Osswald, 2018; Panza et al., 2019). A relevant percentage of clinically diagnosed AD patients show additional brain pathologies beside Abeta and Tau in autopsy (Robinson et al., 2018a). Even in the cases of neuropathological AD diagnosis (i.e., secured Abeta and Tau pathology in histology), 55% of cases also exhibited a pathology of alpha synuclein (which we would expect in synucleinopathies like Parkinson's disease) and 40% showed transactive response DNA binding protein 43kDa (TDP-43), a protein which we would expect in frontotemporal dementia or amyotrophic lateral sclerosis (Robinson et al., 2018b). Brain tissue of people who did not had relevant neurodegenerative brain changes in histological exams after death were showing Abeta in 50% and Tau pathology in 93% of the cases when using sensitive immunohistochemistry methods (Robinson et al., 2018b). Although Abeta and Tau are widely accepted as involved parts in the pathogenesis of AD and also define the disease entity (Jack et al., 2018), it remains unclear if they might be only epiphenomena of other contributing factors. This study hypothesizes a mechanistic role of Abeta in the disease process and builds a link between the molecular pathway alteration that leads to Abeta phenomenon of disinhibition and neural slowing in EEG (Figure 1). Our mechanistic modeling approach can help to understand the complex inter-dependencies between the involved factors in AD and will improve through iterative refinement.

Near Abeta plaques, a shift in neural activity has been observed (Busche et al., 2008). In AD mouse models with overexpression of APP and Presenilin-1, the number of hyperactive neurons was increased near Abeta plaques. This shift in the neuronal activity was associated with decreased performances in memory tests. Neuronal hyperactivity could be reduced by GABA agonists, suggesting pathology due to impaired inhibition. In neocortical and dentate gyri, pyramidal cells have been found to increase network excitability *in vivo* in an AD mouse model with overexpression of Abeta, that led to membrane depolarization and increased firing rates. A study by Hazra et al. (2013) investigated an AD mouse model by stimulation of the perforant pathway. AD mice showed increased amplitude and larger spatial distribution of response after stimulation. The reason for this increased network excitability was due to

impaired inhibitory neuron function, i.e., the inhibitory neurons of the molecular layer of the dentate gyrus in hippocampus were in part unable to produce action potentials, which resulted in a slower postsynaptic firing rate. Ulrich (2015) added Abeta to layer V pyramidal cells of rats. In their experiments they could show a decline in inhibitory postsynaptic currents (IPSCs), attributed to postsynaptic GABA_A receptor endocytosis after Abeta application. In a recent study by Ren et al. (2018) Abeta was found to increase excitability of pyramidal cells in the anterior cingulate cortex of mouse brain. The reason for hyperexcitability was again due to disturbed inhibitory input. Abeta seems to interact with the dopaminergic D1 receptor system. The D1 receptor regulates GABA release in fast-spiking (FS) inhibitory interneurons. By adding a D1 receptor antagonist to the cells they could reverse the effect of Abeta, increase IPSCs and decrease pyramidal excitability whereas D1 agonists had similar effects as Abeta. The underlying working model is that Abeta leads to dopamine release in dopaminergic neurons that activates D1 receptors at FS inhibitory interneurons and thus inhibits GABA release. As a consequence, the amplitude, frequency and total number of IPSPs is decreased. The instantaneous decrement of postsynaptic amplitude and frequency is also known as a toxic effect of Abeta in the glutamatergic system (Ripoli et al., 2014). Hence for the present modeling approach we decided to implement this Abeta dependent impaired inhibitory function. From the literature above, potential models for this disinhibition could be either a lower IPSP amplitude or a lower firing rate or a combination thereof.

One already established drug that assesses the pathology of hyperexcitation is memantine, an N-methyl-D-aspartate (NMDA) antagonist. Memantine is recommended for the symptomatic treatment of severe AD as a mono- and combination therapy with cholinesterase inhibitors and should be also considered as possible treatment in moderate AD in the current version of the UK National Institute for Health and Care Excellence (NICE) guidelines of dementia management (Pink et al., 2018). However, normally it is considered as an alternative or addition to cholinesterase inhibitors (Pink et al., 2018). In contrast, memantine has shown in a current meta-analysis its efficacy to improve cognitive function and reduce behavioral disturbances in AD patients compared to placebo (Kishi et al., 2017). The effect was particularly caused by the moderate-to-severe AD patients (Chen et al., 2017; Kishi et al., 2017) and was also observable in combination therapies with acetyl cholinesterase inhibitors, with a significant superiority for the combination of memantine and donepezil compared to any cholinesterase monotherapies (Kishi et al., 2017). It therefore is also recommended as possible first-line therapy in AD (Kishi et al., 2017). In our study, we will evaluate "virtual memantine" interacting with the Abeta-derived hyperexcitation.

Changes in electroencephalography (EEG) are described in AD as a general and progressive slowing of brain oscillations. In AD, cognitive decline and ¹⁸F-fluorodeoxyglucose (FDG) PET signal decreases are linked with increased left temporal power in the delta and the theta frequency bands, whereas temporo-parieto-occipital alpha band coherence decreases and delta coherence increases (Loewenstein et al., 1989; Rice et al.,



1990; Malek et al., 2017). Moreover, the spatial appearance of slow rhythms and hypometabolism in FDG PET have been linked (Dierks et al., 2000; Babiloni et al., 2016). A recent study produced similar findings in magnetoencephalography (MEG): A global increase of theta and a frontal increase of delta were correlated with entorhinal atrophy and glucose hypometabolism (Nakamura et al., 2018). In summary, a global slowing has been reported for AD, in particular a shift from alpha to theta and delta activity (Loewenstein et al., 1989; Rice et al., 1990; Dierks et al., 2000; Babiloni et al., 2016; Malek et al., 2017; Nakamura et al., 2018).

As a consequence of these findings, we will focus in our modeling approach on three main aspects of AD:

1. Spatial heterogeneous Abeta distribution in the brain
2. Hyperexcitation caused by impaired inhibitory function
3. Slowing of neural frequencies.

For Abeta, we propose a change in local neuronal excitability. Therefore, we construct a model of a healthy “standard brain” with an averaged structural connectivity (SC) with inferred micro-scale characteristics of excitation in those areas where a deposition of Abeta is found. We will infer this information about the local distribution of Abeta from individual AV-45 (florbetapir) positron emission tomography (PET) images. AV-45 is a PET tracer which binds to Abeta (Clark et al., 2011; Ossenkoppele et al., 2015; Morris et al., 2016; Martinez et al., 2017). Ante-mortem Abeta PET imaging can be related to post mortem Abeta pathology in brain tissue (Murray et al., 2015), corresponding to the THAL phases of Amyloid deposition (Thal

et al., 2002)—as well as Tau PET (Schöll et al., 2016) can be related to the BRAAK stages of neurofibrillary tangles (Braak and Braak, 1991, 1997; Braak et al., 2006). This has led to updated diagnostic criteria for AD, wherein Abeta and Tau PET can be used equivalently to neuropathology for AD diagnosis (Jack et al., 2018).

We investigate three clinical diagnostic groups of age- and gender-matched healthy controls (HC), individuals with mild cognitive impairment (MCI) and AD patients [see method section Alzheimer’s Disease Neuroimaging Initiative (ADNI) Database and **Table 1**]. For the simulated EEG and the underlying local neural activity frequency we expect a slowing in rhythms and particular a shift from alpha to theta activity with disease progression. Finally, we will simulate the effect of an anti-excitotoxic drug, the NMDA antagonist memantine for which we expect a reversal of the observed EEG slowing.

We will in the following provide an overview of the fundamentals of the here employed brain simulation technique. The particular strength of computational connectomics (Ritter et al., 2013; Kringelbach et al., 2015; Deco et al., 2017) or brain network modeling (BNM) is to unite various kinds of information in a single biophysically plausible framework (Breakspear, 2017). BNM are typically structurally informed (or constrained) by (a) geometric information of the brain, e.g., via T1 magnetic resonance imaging (MRI), and (b) the structural connectivity (SC) derived from the tractography of diffusion MRI that is supposed to represent the white matter fiber tracts (Jirsa et al., 2002; Schirner et al., 2015). The static three-dimensional scaffold of the brain is brought to life through

TABLE 1 | Basic epidemiological information of the study population.

Diagnosis	<i>n</i> (female)	Mean age	σ	Min. age	Max. age	Mean MMSE	σ	Min. MMSE	Max. MMSE
AD	10 (5)	72.0	9.6	55.9	86.1	21.3	6.8	9	30
HC	15 (9)	70.6	4.7	63.1	78.0	29.3	0.8	28	30
MCI	8 (3)	68.2	6.4	57.8	76.6	27.1	1.6	25	30

It is a subset of the suitable ADNI-3 participants, that had 3T imaging and all necessary image modalities. Only data from Siemens scanners was used (because this was the biggest subset of scanners).

the implementation of mathematical models, which generate activity at each brain region or node of the network, the so-called neural masses or population models (Spiegler and Jirsa, 2013; Sanz-Leon et al., 2015; Cabral et al., 2017). Population models are reduced descriptions of microscopically detailed neuronal networks (Wilson and Cowan, 1972; Zetterberg et al., 1978; Hindmarsh and Rose, 1984; Jansen and Rit, 1995; Wong and Wang, 2006; Stefanescu and Jirsa, 2008; Sanz-Leon et al., 2015)—inferred for example with methods of mean field theory (Deco et al., 2008; Jirsa, 2009; Bojak et al., 2010). They describe the so called meso-scale of the brain (Deco et al., 2008; Wright and Liley, 2010), i.e., population activity as captured with imaging methods like EEG, MEG and fMRI. Some neural mass models (NMM) are linked to (and still reflect to a certain degree) neurophysiological processes at the microscopic scale while others mathematically describe the observed lumped biological behavior not differentiating between underlying neurophysiological processes (phenomenological models). Time delays in the interaction between nodes (Jirsa and Kelso, 2000; Jirsa et al., 2002; Spiegler and Jirsa, 2013; Sanz-Leon et al., 2015) are critical for the spatiotemporal organization of the evolving activity patterns in the brain (Petkoski et al., 2016, 2018). Measured functional brain data such as EEG, MEG or functional MRI (fMRI) are used to tune the mathematical models—i.e., to fit selected free parameters of the model—to faithfully reproduce selected empirical features (Honey et al., 2007; Ghosh et al., 2008; Sotero and Trujillo-Barreto, 2008; Bojak et al., 2010; Jirsa et al., 2010; Ritter et al., 2013; Sanz-Leon et al., 2015; Kunze et al., 2016). By performing a systematic model parameter exploration, using e.g., brute force exhaustive parameter space searches, Monte-Carlo methods or weighted optimization algorithms, we can identify the optimal parameter configuration to portray the empirical functional phenomena. Thereby, we obtain indices of the brains individual function in relation to the explored parameters. This approach opens various possibilities to not only describe dependencies (i.e., correlations), but to make statements about potential underlying causal processes, i.e., mechanisms.

In this study we used TVB, an open source neuroinformatics platform (Ritter et al., 2013; Sanz Leon et al., 2013; Sanz-Leon et al., 2015; Stefanovski et al., 2016) (www.thevirtualbrain.org) for large-scale BNM simulations. We have already established the software TVB, and applied it to normative datasets, stroke, epilepsy, brain tumors, and neurodegenerative disease. For example, in stroke recovery, TVB models of patients were built using the patient's structural neuroimaging data, and the dynamics of local populations were tuned to fit the patient's

functional neuroimaging data (Falcon et al., 2015, 2016). The obtained parameters for excitatory/inhibitory (EI) balance of local neuronal populations predicted the patient's response to rehabilitation up to 1 year after therapy. Our work on epilepsy was able to infer seizure propagation with a model based on the patient's own diffusion weighted MRI and stereotaxic EEG (Jirsa et al., 2017; Proix et al., 2017). Moreover, positive surgical outcome was strongly associated with the epileptogenic zone that was excised as predicted by the patient's TVB model. Previous work with AD patients ($n = 16$), controls ($n = 73$), and persons with amnesic MCI ($n = 35$), all from the Sydney Memory and Aging Study, confirms the benefit of using the model parameters to characterize cognitive status (Zimmermann et al., 2018).

TVB provides several types of NMMs. In the present study, we selected a NMM that can simulate EEG and enables us to implement disinhibition. The wiring pattern of cortical circuitry is characterized by recurrent excitatory and inhibitory loops, and by bidirectional sparse excitatory connections at the large-scale (Schüz and Braitenberg, 2002). Several NMMs therefore feature projection neurons aka pyramidal cells with long axons projecting to distant cortical regions and local excitatory and inhibitory feedbacks (Lopes da Silva et al., 1974; Freeman, 1975; Jansen and Rit, 1995). The NMM by Jansen-Rit comprises an elementary circuit of three interconnected NMMs (**Figure 2**) describing a cortical area (or column). It has been used to explain both epilepsy-like brain activity (Wendling et al., 2000, 2002) and various narrow band oscillations ranging from the delta to the gamma frequency bands (David and Friston, 2003) including intracranial EEG (Spiegler and Jirsa, 2013). The Jansen-Rit model has been explored extensively on a single population level (Wendling et al., 2002; David and Friston, 2003; Spiegler et al., 2011) and in BNMs (Sotero et al., 2007; Merlet et al., 2013; Kunze et al., 2016). The Jansen-Rit model has a rich dynamic repertoire, which was extensively described before (Spiegler et al., 2010).

Specifically we chose the Jansen-Rit model for the present study due to the following considerations:

- (1) The Jansen-Rit model comprises three interacting neural masses (representing different cellular populations) in each local circuitry: pyramidal cells, inhibitory, and excitatory interneurons (**Figure 2B**). This is unique and opens the possibility to simultaneously model disinhibition, i.e., an impairment of the inhibitory neuronal subpopulation in one neural mass, and an anti-NMDAergic effect, i.e., a downscaled

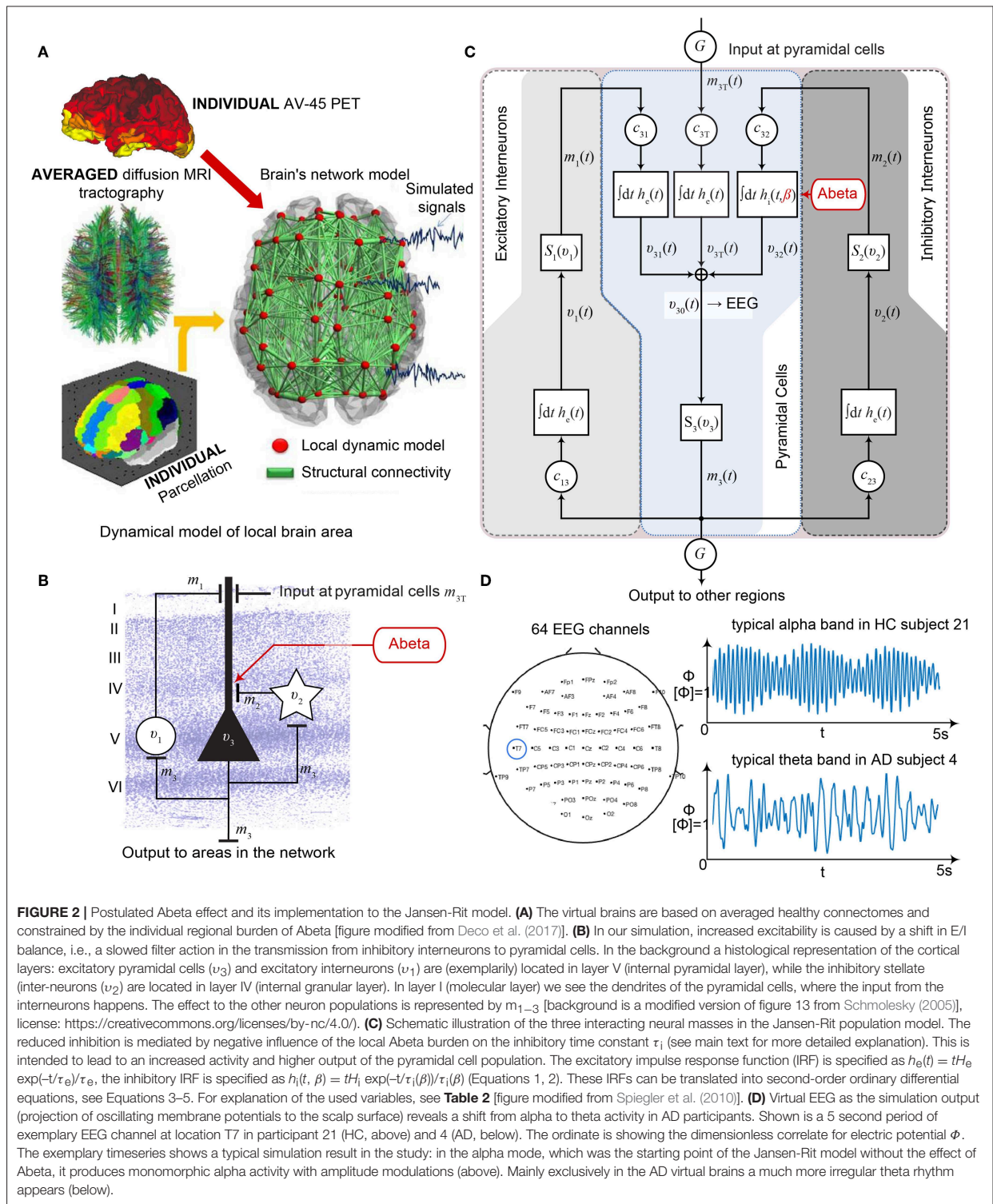


TABLE 2 | Used parameters for each Jansen-Rit element in the large-scale brain network (Jansen and Rit, 1995).

Parameter	Description	Value	Unit
H_e	Coefficient of the maximum amplitude of EPSP. Also called average synaptic gain (Equations 1, 3).	3.25	1 mV
H_i	Coefficient of the maximum amplitude of IPSP. Also called average synaptic gain (Equations 2, 4).	22.0	1 mV
$h_e(t)$	Amplitude of EPSP as a function of time (Equation 1).	Variable	1 mV
$h_i(t, \beta_a)$	Amplitude of IPSP as a function of time and local Abeta burden (Equation 2).	Variable	1 mV
τ_e	Excitatory dendritic time constant (Equations 1, 3, 5).	10.0	1 ms
$\tau_i(\beta_a)$	Inhibitory dendritic time constant as a function of Abeta load (Equations 2, 4, 13, 14).	$14.29 \leq \tau_i < 50$	1 ms
v_0	Is the mean PSP threshold for 50% of maximum firing rate (Equation 11).	6.0	1 mV
v_1	PSP of excitatory population (Equations 3, 10).	Variable	1 mV
v_2	PSP of inhibitory population (Equations 4, 10).	Variable	1 mV
v_3	PSP of pyramidal population (Equation 5).	Variable	1 mV
v_{30}	Outgoing projection of pyramidal population (Equation 10).	Variable	1 mV
e_0	The firing rate at the inflection point $e_0 = S(v = v_0)$. The maximum firing rate is $2e_0$ (Equation 11).	2.5	1 s^{-1}
f_v	Steepness of the sigmoid PSP-to-firing-rate transfer function (Equation 11).	0.56	$(\text{mV})^{-1}$
c_{31}	Average number of synaptic contacts from excitatory to pyramidal cells (Equation 3).	108.0	1
c_{13}	Average number of synaptic contacts from pyramidal to excitatory cells (Equation 3).	135.0	1
c_{32}	Average number of synaptic contacts from inhibitory to pyramidal cells (Equation 4).	33.75	1
c_{23}	Average number of synaptic contacts from pyramidal to inhibitory cells (Equation 4).	33.75	1
$m_{3T,0}$	Input firing rate at the pyramidal cells (Equation 12).	0.1085	$(\text{ms})^{-1}$
G	Global structural connectivity scaling factor.	$0 \leq G \leq 600$	1
$S_{\max, \tau}$	Maximum value of the inhibitory rate/reciprocal of inhibitory time constant (Equation 14).	0.07	$(\text{ms})^{-1}$
$S_{0, \tau}$	Minimum value of the inhibitory rate/reciprocal of inhibitory time constant (Equation 14).	0.02	$(\text{ms})^{-1}$
β_{\max}	95th percentile value for the Abeta burden $A\beta$ as the PET SUVR for all regions and all participants (Equations 13, 14).	2.65	1
β_{off}	Cut-off-value for the Abeta burden $A\beta$ as the PET SUVR, from which one a pathological meaning is suspected (Equations 13, 14).	1.4	1

transmission from excitatory interneurons to pyramidal cells, at the same time.

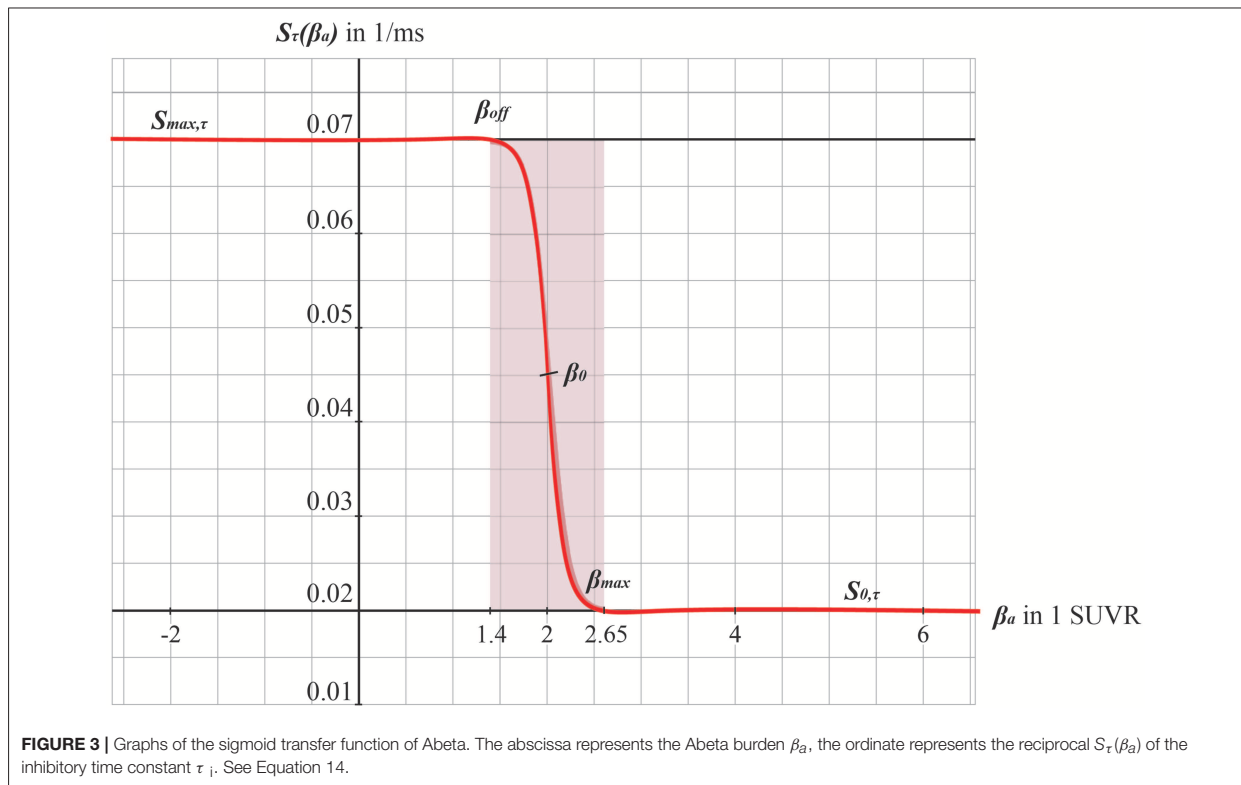
- (2) The ratio of excitatory and inhibitory time constants τ_e/τ_i in the Jansen-Rit model is suitable to model the effect of Abeta on the inhibitory interneurons (by affecting the transmission from inhibitory interneurons to pyramidal cells, **Figures 2B,C**) and is also known to have an effect on the simulated neural frequency (Wendling et al., 2002; Spiegler et al., 2010). Because oscillations emerge in the Jansen-Rit model of a brain region due to the interplay of positive and negative feedback loops (excitatory and inhibitory interneurons), a change in one of the time constants does not necessarily slow down or speed up rhythms. However, if both excitatory and inhibitory time constants, τ_e and τ_i are scaled simultaneously and uniformly, the local equilibrium of interaction between the neural masses remains the same but the time signature such as frequency changes [see Figure 9 in Spiegler et al. (2010), and see Chapter 3.1.3 “Model Equivalence” and Chapter 3.1.4 “Normalization” in Spiegler (2011)]. To conclude, higher τ_i does not necessarily lead to slower rhythms and vice versa.
- (3) Jansen-Rit can simulate physiological rhythms observable in local field potentials (intracranially), stereo-EEG (sEEG), scalp EEG, and MEG (Jansen and Rit, 1995; Spiegler et al., 2010; Sanz-Leon et al., 2015).

Our hypothesized effect of local Abeta deposition as inferred from subject-specific AV-45 PET is a decrease of local inhibition (Busche et al., 2008; Grienberger et al., 2012; Limon et al., 2012; Verret et al., 2012; Hazra et al., 2013; Ripoli et al., 2014; Ren et al., 2018), which leads to a relatively stronger local excitation. This theory allows us translation of the Abeta distribution into the altered dynamics of a population model (Equation 14 and **Figure 3**). We use an averaged healthy SC to control the effect of individual differences in the connectome. I.e., in our simulations the distribution of Abeta is the only individual factor and can therefore be seen as the cause of any differences between the participants. The hypothesized microscale (synaptic), spatially distributed effect is assumed to develop an effect at the population (mesoscale) level and to eventually propagate to the large-scale of the whole brain. A schematic illustration of this concept is provided in **Figures 1, 2**.

METHODS

Alzheimer's Disease Neuroimaging Initiative (ADNI) Database

Empirical data were obtained from the Alzheimer's Disease Neuroimaging Initiative (ADNI) database (adni.loni.usc.edu). The ADNI was launched in 2003 as a public-private partnership, led by Principal Investigator Michael W.



Weiner. The primary goal of ADNI has been to test whether serial MRI, PET, other biological markers, and clinical and neuropsychological assessment can be combined to measure the progression of MCI and early AD. For up-to-date information, see <http://www.adni-info.org>.

In the presently ongoing trial, ADNI-3, the measurements contain T1, T2, DTI, fMRI, Tau PET, Abeta PET, and FDG PET for the participants. The total population of ADNI-3 will contain data of about 2,000 participants (comprising AD, MCI, and HC, see <http://adni.loni.usc.edu/adni-3/>). As inclusion criterion for AD patients the diagnosis criteria of NINCDS-ADRDA from 1984 were used, which contains only clinical features (McKhann et al., 1984). Inclusion criteria for both HC and MCI were a Mini Mental State Examination (MMSE) score between 24 and 30 as well as age between 55 and 90 years. For MCI in addition, the participant must have a subjective memory complaint and abnormal results in another neuropsychological memory test. To fulfill the criteria for AD, the MMSE score had to be below 24 and the NINCDS-ADRDA criteria for probable AD had to be fulfilled (McKhann et al., 1984). Imaging and biomarkers were not used for the diagnosis. For the full inclusion criteria of ADNI-3 see the study protocol (page 11f in http://adni.loni.usc.edu/wp-content/themes/freshnews-dev-v2/documents/clinical/ADNI3_Protocol.pdf). An overview of the epidemiological characteristics of the participants included in this study can be found in **Table 1**.

Data Acquisition and Processing

All images used in this study were taken from ADNI-3. To reach comparable datasets, we used only data from Siemens scanners with a magnetic field strength of 3T (models: TrioTim, Prisma, Skyra, Verio). However, some acquisition parameters differed slightly. See Supplementary Material with **Supplementary Tables 1–6** for the metadata. The following imaging modalities were included: **T1 MPRAGE**. TE = 2.95–2.98 ms, TR = 2.3 s, matrix and voxel size differ slightly. **FLAIR**. TE differs slightly, TR = 4.8 s, matrix size = 160 · 256 · 256, voxel size differs slightly. **DWI** (only for 15 HC participants to create an average healthy SC). TE = 56–71 ms, TR = 3.4–7.2 s, matrix size = 116 · 116 · 80, voxel size = 2 · 2 · 2, bvals = [0, 1000] or [0, 500, 1000, 2000], bvecs = 49 or 115. **Siemens Fieldmaps and PET Data** (AV-45 for Abeta). The preprocessing of imaging data can be subdivided in that of structural images, DWI, and PET.

Structural MRI

We calculated an individual brain parcellation for each included participant of ADNI-3. We followed the minimal preprocessing pipeline (Glasser et al., 2013) of the Human Connectome Project (HCP) for our structural data using Freesurfer (Reuter et al., 2012) (<https://surfer.nmr.mgh.harvard.edu/fswiki/FreeSurferMethodsCitation>), FSL (Smith et al., 2004; Woolrich et al., 2009; Jenkinson et al., 2012) and connectome workbench (<https://www.humanconnectome.org/software/connectome-workbench>). Therefore, we used T1 MPRAGE,

FLAIR and fieldmaps for the anatomical parcellation and DWI for tractography. This consists of a Prefreesurfer, Freesurfer, and Postfreesurfer part. We skipped the step of gradient non-linearity correction, since images provided by ADNI already are corrected for this artifact. Also, the MNI templates were used at 1 mm resolution instead of 0.7 mm. In the Freesurfer pipeline we skipped the step of downsampling our data from 0.7 to 1 mm³, and all recon-all and intermediate steps were performed with the original image resolution. We then registered the subject cortical surfaces (32 000 vertices) to the cortical parcellation of Glasser et al. (2016) using the multimodal surface matching (MSM, see Robinson et al., 2014) tool. For the registration we used cortical thickness, MyelinMaps, cortical curvature and sulc from the subject and template surface. We mapped the parcellation on the surface back into the gray matter volume with connectome workbench. This volume parcellation served as the mask for the connectome and PET intensity extraction.

PET Images

We used the preprocessed version of AV-45 PET. These images had following preprocessing already performed by ADNI: Images acquired 30–50 min post tracer injections: four 5-min frames (i.e., 30–35 min, 35–40 min...). These frames are co-registered to the first and then averaged. The averaged image was linearly aligned such that the anterior-posterior axis of the subject is parallel to the AC-PC line. This standard image has a resolution of 1.5 mm cubic voxels and matrix size of 160 · 160 · 96. Voxel intensities were normalized so that the average voxel intensity was 1. Finally, the images were smoothed using a scanner-specific filter function. The filter functions were determined in the certification process of ADNI from a PET phantom. We used the resulting image and applied the following steps: Rigid aligning the PET image to participants T1 image (after being processed in the HCP structural pipeline). The linear registration was done with FLIRT (FSL). The PET image was then masked with the subject specific brainmask derived from the structural preprocessing pipeline (HCP). To obtain the local burden of Abeta, we calculated the relative intensity to the cerebellum as a common method in the interpretation of AV-45-PET, because it is known that the cerebellum does not show relevant AV-45 PET signals and can therefore act as a reference region for inter-individual comparability between patients (Clark et al., 2011; Meyer et al., 2018). The intensity of gamma radiation, which is caused by a neutralization reaction between local electrons and the emitted positrons of the nuclear tracer is measured for each voxel in the PET image and divided to the cerebellar reference volume: the standardized uptake value ratio (SUVR). We therefore receive in each voxel a relative Abeta burden β which is aggregated according to the parcellation used for our present modeling approach (see below). Thus, we obtain a value β_a for the Abeta burden in each brain region a . The cerebellar white matter mask was taken from the Freesurfer segmentation (HCP structural preprocessing). The image was then partial volume corrected using the Müller-Gärtner method from the PETPVC toolbox (Thomas et al., 2016). For this step the gray (GM) and white matter segmentation from Freesurfer (HCP structural preprocessing) was used. Subcortical region PET

loads were defined as the average SUVR in subcortical GM. Cortical GM PET intensities were mapped onto the individual cortical surfaces using connectome workbench tool with the pial and white matter surfaces as ribbon constraints. Using the multimodal parcellation from Glasser et al. (2016) we derived average regional PET loads.

DWI

We calculated individual tractography only for included HC participants of ADNI-3 to average them to a standard brain template (see section Virtual Human Standard Brain Template Out of Averaged Healthy Brains below). Preprocessing of the diffusion weighted images was mainly done with the programs and scripts provided by the MRtrix3 software package (<http://www.mrtrix.org>).

The following steps were performed:

Dwidenoise. Denoising the DWI data using the method described in Veraart et al. (2016).

Dwipreproc. Motion and eddy current correction using the *dwipreproc* wrapper script for FSL (https://mrtrix.readthedocs.io/en/latest/dwi_preprocessing/dwipreproc.html).

Dwibiascorrect. B1 field inhomogeneity correction using ANTS N4 algorithm.

Dwi2mask. brainmask estimation from the DWI images.

Dwiintensynorm. DWI intensity normalization for the group of participants.

Dwi2response. The normalized DWI image was used to generate a WM response function. We used the algorithm described by Tournier et al. (2013) in this step.

Average_response. An average response function was created from all participants.

Dwi2fod. Using the spherical deconvolution method described by Tournier et al. (2007) we estimated the fiber orientation distribution using the subject normalized DWI image and the average response function. From the DWI data a mean-b0 image was extracted and linear registered to the T1 image. The inverse of the transform was used to bring the T1 brain masked and *aparc+aseg* image (from HCP structural preprocessing) into DWI space. The transformed *aparc+aseg* image was used to generate a five tissue type image.

Tckgen. Anatomical constrained tractography (Smith et al., 2012) was performed using the iFOD2 algorithm (Tournier et al., 2010). Tracks in the resulting image were weighted using SIFT2 algorithm (Smith et al., 2015). We mapped the registered parcellation from Glasser back into the volume. The cortical and subcortical regions that were used to merge the tracks into a connectome.

EEG Forward Solution in TVB

After structural preprocessing with the HCP pipeline we used the individual cortical surfaces and T1 images to compute the person specific Boundary Element Models in Brainstorm (Tadel et al., 2011). Scalp, outer, and inner skull were modeled with 1922 vertices per layer. Using the default “BrainProducts EasyCap 65” EEG cap as locations for the signal space and the cortical surface vertices as source space. The leadfield matrix was estimated using

the adjoint method in OpenMEEG with the default conductivities 1, 0.0125 and 1 for scalp, skull and brain, respectively. Because we are performing region-based simulations only (i.e., no vertex-wise modeling), the leadfield matrix was simplified by summing the coefficients of vertices that belong to the same region. EEG signal was generated by matrix multiplication of the neural time series with the lead field matrix.

Virtual Human Standard Brain Template Out of Averaged Healthy Brains

We use the SCs of all ADNI-3 participants of the group HC, derived from the diffusion-weighted and structural MRI, to average them to one connectome matrix. Two of the HC participants included in the average template were excluded for simulations because it was impossible to compute their leadfield matrices for EEG calculation. Therefore, we use an arithmetic mean $C_\mu = (\sum_{i=1}^n C_i)/n = (C_1 + C_2 + \dots + C_n)/n$, wherein C_μ is the averaged SC matrix, n is the number of HC participants and C_i is the individual SC matrix. The SC matrix and the organization of the corresponding graph can be found in **Figure 4**. As it can be seen in **Figure 4B**, general characteristics of physiological SCs as symmetry, laterality, homology, and subcortical hubs are maintained in the averaged connectome. By choosing an averaged SC instead of individual SCs, it was possible to control all factors except of the individual Abeta distribution supporting our intention to compare the simulated activity that resulted from a “pathogenic” modification by Abeta.

Cause-and-Effect Model of Abeta in the Jansen-Rit Model

The dynamics of the Jansen-Rit model show a rich parameter dependent behavior (Spiegler et al., 2010). A bifurcation analysis of the single population Jansen-Rit model (in contrast to network embedded interacting populations) catalogs and summarizes the repertoire of the model. Bifurcation here refers to a qualitative change in the system behavior with respect to parameter changes. Qualitative changes can be for instance the shift from waxing and waning alpha rhythm as observed in resting human brains to spike wave discharges as observed during epileptic seizures. Bifurcation diagrams explore the qualitatively different states [divided by bifurcations, see Supplementary Figure 1, from Spiegler et al. (2010)]. The bifurcation analysis revealed an important feature of the Jansen-Rit model, which is bistability, that is, the coexistence of two stable states for a certain parameter range (i.e., regime). The bistable regime allows the coexistence of two self-sustained oscillatory states for the standard parameter configuration (Jansen and Rit, 1995) and **Table 2** of which one state generates rhythmic activity in the alpha band and the other one produces slower big spike-wave complexes in theta rhythm. Changes in the kinetics of excitatory and inhibitory PSPs (i.e., changes of time constants) change the model behavior in a way which makes it suitable to scale, that is, to speed up or to slow down local dynamics (Spiegler et al., 2010)—and therefore to scale the global frequency, too. The results of the systematic parameter exploration of the excitatory and inhibitory time constants are summarized in **Supplementary Figure 2**. For

our study, we constructed the model to portrait a wide range of physiological neural rhythms by using a fast limit cycle with alpha and beta frequencies and a slow limit cycle with theta and delta frequencies. To achieve this dynamic behavior of two limit cycles, we used first a very low input on the pyramidal cells (firing rate 0.1085/ms) and no input on the inhibitory interneurons to not overlay the Abeta effects we introduce here. Therefore in the “healthy” condition without the effect of Abeta, the system operates near the subcritical Andronov-Hopf and the saddle-saddle bifurcations (leftmost region in **Supplementary Figure 1**). For the time constants, we used the area of alpha rhythm (blue area in **Supplementary Figure 2**) as control condition without any effect of Abeta. The detailed parameter settings can be found in **Table 2**.

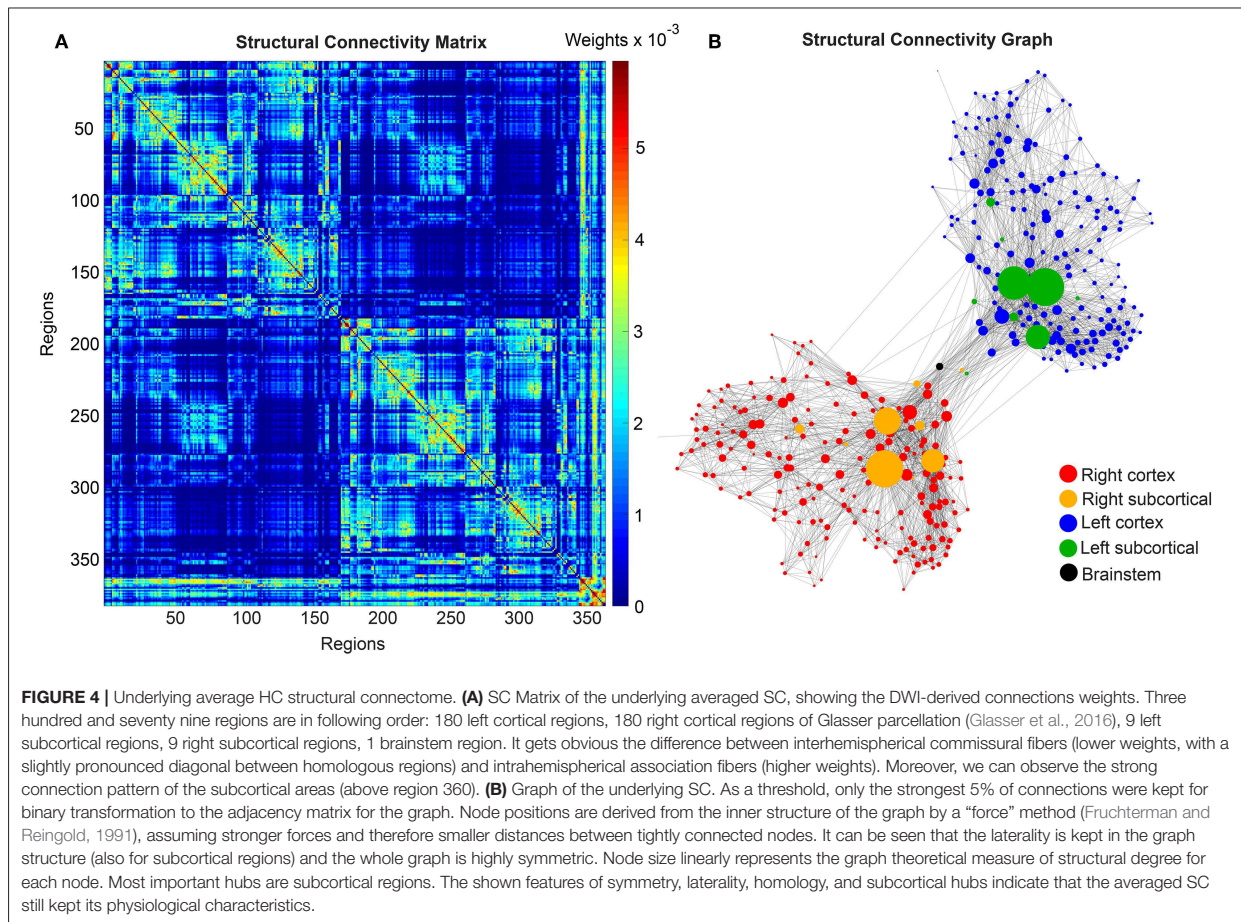
The information about the local Abeta burden is derived from the individual AV-45 PET. As there exists no established clinical standard for SUVR cut-off thresholds differentiating normal form pathological Abeta loads. To scale the possible neurotoxic effect in a realistic way, we need to approximate at what point Abeta toxicity occurs. Following the literature, a 96% correlation to autopsy after Abeta PET was achieved via visual assessment of PET images. The corresponding SUVR cut-off was 1.2 (Clark et al., 2011). Another study showed a higher cut-off point at $SUVR \geq 1.4$ for a 90% sensitivity of clinically diagnosed AD patients with an abnormal Abeta PET scan (Jack et al., 2014). We use here the higher cut-off threshold of $SUVR \geq 1.4$. Consequently, we propose a cause-and-effect model for Abeta that is mapping molecular changes to computational brain network models:

The inhibitory time constant τ_i in each point is a function of β_a . The higher Abeta SUVR, the higher τ_i and therefore the filter action for the synaptic transmission is slower. We decided for this implementation via a synaptic filter slowing because of several reasons:

1. We are focusing on disease linked alterations of EEG frequencies. Hence, we intended to assess a model feature that is already known to be frequency-effective, i.e., it can vary resulting simulated EEG frequencies. From former explorations of the Jansen-Rit-model we know that the neural frequencies are influenced by the ratio of excitatory and inhibitory time constants (Spiegler et al., 2010).
2. Cellular studies are supporting the hypothesis of altered inhibition as a cause for hyperexcitation (Hazra et al., 2013; Ripoli et al., 2014; Ren et al., 2018)—hence we decide for mapping Abeta on the inhibitory time constant leading to a disturbed Excitatory-Inhibitory (E/I) balance.
3. By using a time-effective feature, we intended to differentiate the micro-scale neurotoxic effect of Abeta on synaptic level (Ripoli et al., 2014; Ulrich, 2015; Ren et al., 2018) from connectivity-effective phenomena on a larger scale, which could e.g., be modeled by an alteration of connection strength.

A detailed exploration of the effects that we introduce by this model can be found in the discussion section.

We develop a transform function to implement the PET SUVR in parameters of the brain network model. Specifically, we postulate a sigmoidal decrease function that modifies the



default value for inhibitory time constant τ_i (Equation 14 and Figure 3). We assume the healthy brain without super-threshold Abeta burden operates in a region of the parameter space, which is close to a network criticality. A criticality describes an area in the parameter space, where subtle changes of one variable can have a critical impact on others (Strogatz, 2015) (in this case bifurcations, see Supplementary Figure 1. The thresholding “cut-off” value β_{off} —differentiating normal form pathological Abeta burden—was chosen according to the literature, stating that only after a certain level of tracer uptake a region is considered pathological ($\beta_{\text{off}} = 1.4$, see above). The maximum possible Abeta burden value β_{max} was chosen to be the 95% percentile of the Abeta regional SUVR distribution across all participants. The midpoint of the sigmoid was chosen such that it was half the way between β_{off} and β_{max} . The steepness was chosen such that the function converges to a linear function between β_{off} and β_{max} .

Brain Network Model Construction and Simulation

For the reasons stated in the above introduction, for our simulation approach we selected the Jansen-Rit model

(Zetterberg et al., 1978; Jansen and Rit, 1995; Wendling et al., 2000; David and Friston, 2003; David et al., 2006; Spiegler et al., 2010, 2011; Sanz-Leon et al., 2015; Kunze et al., 2016). The differential equations are presented in Equations 3–5 (Jansen and Rit, 1995). The employed parameter values can be found in Table 2.

As a general approach, the impulse response function (IRF) of a neural mass allows to transform an incoming action potential into a PSP by using a linear time-invariant system. The IRF is the transfer function of the system, which is convoluted with the incoming input (action potentials) to calculate the output (PSPs). The general form of the IRF is the systems output to a (infinitesimal short and high) Dirac impulse and can be estimated experimentally by using short impulses or step functions (Lopes da Silva et al., 1974; Freeman, 1975).

The excitatory IRF $h_e(t)$ is therefore specified as

$$h_e(t) = tH_e \exp(-t/\tau_e)/\tau_e, \quad (1)$$

where τ_e is the excitatory time constant (the time until the PSP reaches its maximum), H_e is a coefficient of the PSP amplitude and t is time.

Similarly, the inhibitory IRF $h_i(t, \beta)$ is specified as

$$h_i(t, \beta) = tH_i \exp(-t/\tau_i(\beta))/\tau_i(\beta), \quad (2)$$

with the same variables as above. As we will describe below in detail, the inhibitory IR is a function of the spatially distributed Abeta burden β , which affects the time characteristics $\tau_i(\beta)$ and therefore $h_i(t, \beta)$ is a function of time and space.

These IRFs can be translated into second-order ordinary differential equations by interpreting them as Green's functions. See Spiegler et al. (2010) for a detailed explanation of the dimensional reduction used here.

The differential equations that describe the network of three neural masses are now presented in Equations 3–5. The variables used for the simulations are listed in **Table 2**:

Excitatory projections v_1 onto pyramidal cells at location a in discretized space ($a = 1, 2, \dots, N$; $N = 379$ regions):

$$\begin{cases} dv_{1,a}(t)/dt = v_{4,a}(t) \\ dv_{4,a}(t)/dt = H_e(m_{3T,a}(t) + c_{31}S(c_{13}v_{3,a}(t)))/\tau_e \\ \quad - 2v_{4,a}(t)/\tau_e - v_{1,a}(t)/\tau_e^2 \end{cases} \quad (3)$$

Inhibitory projections v_2 onto pyramidal cells at location a in space:

$$\begin{cases} dv_{2,a}(t)/dt = v_{5,a}(t) \\ dv_{5,a}(t)/dt = c_{32}H_i S(c_{23}v_{3,a}(t))/\tau_i(\beta_a) \\ \quad - 2v_{5,a}(t)/\tau_i(\beta_a) - v_{2,a}(t)/\tau_i^2(\beta_a) \end{cases} \quad (4)$$

Projections v_3 of pyramidal cells a in space:

$$\begin{cases} dv_{3,a}(t)/dt = v_{6,a}(t) \\ dv_{6,a}(t)/dt = S(v_{30,a}(t))/\tau_e \\ \quad - 2v_{6,a}(t)/\tau_e - v_{3,a}(t)/\tau_e^2, \end{cases} \quad (5)$$

wherein c_{31}, c_{13}, c_{23} are the local connectivity weights between the three neural masses. Equation (4) shows the spatial dependency of the activity of inhibitory interneurons projected onto the pyramidal cells by $\tau_i(\beta_a)$.

Taking into account the biologically plausible configuration of the Jansen-Rit model shown in **Figure 2**, we use several mathematical simplifications to reduce the model's dimensionality without loss of generality. Taking into account that Equation (1) is valid for all excitatory input at dendrites irrespective of the source allows for using one single IRF at the pyramidal cells

$$h_{3I} \equiv h_{3T} \equiv h_e, \quad (6)$$

and, thanks to linearity, translates the summation of excitatory postsynaptic potentials

$$v_{3I} + v_{3T} \equiv v_I \quad (7)$$

into a sum of incoming firing rate, that is, $m_{3T,a}(t) + c_{31} S(c_{13} v_{3,a}(t))$ in Equation (3), describing the excitatory

projections onto pyramidal cells v_1 . This simplification is without restrictions, simply exploits the linearity of the operators and reduces the dimensionality by 2. Furthermore, to adjust notation, the postsynaptic potentials caused by the inhibitory neural mass at pyramidal cells are denoted as

$$v_{32} \equiv v_2, \quad (8)$$

and its kernel is as

$$h_{32} \equiv h_i. \quad (9)$$

The projecting variable of one brain region at location a to other regions in the network is the sum of excitatory and inhibitory postsynaptic potentials at the local neural mass of pyramidal cells

$$v_{30,a}(t) = v_{1,a}(t) - v_{2,a}(t) \quad (10)$$

transferred into a firing rate using a sigmoid. The general form of this transfer function is

$$S(\lambda) = (S_{\max} - S_{\min}) / (1 + \exp(r_\lambda(\lambda_0 - \lambda))) + S_{\min} : 0 < S_{\min} < S_{\max}, \quad (11)$$

with, $\lambda = v$, $S_{v, \max} = 2e_0$ and $S_{v, \min} = 0$ for the potential-to-firing-rate transfer.

Incoming mean firing rates $m_{3T,a}(t)$ at the pyramidal cells at location a from other brain regions $b = 1, 2, \dots, N$, where N is the number of 379 regions are given by

$$m_{3T,a}(t) = m_{3T,0} + G \sum_b w_{a,b} S(v_{30,b}(t)), \quad (12)$$

where $m_{3T,0}$ is baseline input $m_{3T,0} = \text{const.}$ for $\forall t$ and all locations $\forall a$. The global coupling factor G is a coefficient of the incoming activity and therefore scales the connections $w_{a,b}$ incoming at location a from all b provided by the SC. Because of this, G is the crucial factor that moderates the influence of the network to each neural mass and therefore mediates the difference between an uncoupled systems ($G = 0$) and a strong connected system.

In all populations, the state variable $[v_1, v_2, v_3]_a(t)$ are the mean membrane potentials and the derivatives thereof with respect to time t , namely $[v_4, v_5, v_6]_a(t)$ represent the mean currents.

To model how the local Abeta load β_a , measured by the Abeta PET SUVR is affecting the inhibitory time constant we introduce a transfer function (**Figure 3**). The primary assumption of this transfer function is a dependency of the E/I balance on the local Abeta concentration as described above. With higher concentration of Abeta, we assume dynamic changes in the inhibitory population of the neural mass that lead to local hyperexcitation. To model this inside the existing Jansen-Rit equations, potential candidate parameters would be H_i and τ_i as well as c_{32} . The coefficient H_i is not a suitable candidate because it has no direct physiological correlate. The coupling coefficient c_{32} corresponds best to synaptic transmission from inhibitory to pyramidal cells and therefore can be mainly seen as a receptor

surrogate. The time constant τ_i acts as a filter for IPSPs and correlates best with the evidence of decreased IPSP firing rate (Busche et al., 2008; Grienberger et al., 2012; Limon et al., 2012; Verret et al., 2012; Hazra et al., 2013; Ripoli et al., 2014; Ren et al., 2018) and is moreover well explored for the Jansen-Rit model (Wendling et al., 2002; Spiegler et al., 2010). As described above, we expect this transfer function to behave in an asymptotic way for Abeta concentrations below and above a specific range. We determined the lower border at $\beta_{a,\text{off}} = 1.4$ and the upper border at the 95th percentile in our data at $\beta_{a,\text{max}} = 2.65$. By exploring the effects of τ_i in a single region model, we determined the effective range $14.29 \text{ ms} \leq \tau_i < 50 \text{ ms}$. Based on this range we defined the following three-conditional linear function

$$\begin{cases} \tau_i = \tau_{i,\text{min}} & \text{for } \beta_a \leq \beta_{a,\text{off}} \\ \tau_i(\beta_a) = m \cdot \beta_a - c & \text{for } \beta_{a,\text{off}} < \beta_a < \beta_{a,\text{max}} \\ \tau_i = \tau_{i,\text{max}} & \text{for } \beta_a \geq \beta_{a,\text{max}} \end{cases} \quad (13)$$

wherein $\tau_{i,\text{min}}$ and $\tau_{i,\text{max}}$ are the maximum and minimum values for τ_i ,

$$m = (\tau_{i,\text{max}} - \tau_{i,\text{min}}) / (\beta_{a,\text{max}} - \beta_{a,\text{off}}) = 28.6 \text{ and} \\ c = m \cdot \beta_{a,\text{off}} - \tau_{i,\text{min}} = 25.7.$$

Since this function is not differentiable in $\beta_{a,\text{off}}$ and $\beta_{a,\text{max}}$, we used the sigmoid function Equation (12) instead, which is continuous and differentiable. Moreover, a sigmoid can be interpreted as the cumulative (of a logistic distributed) activity acquired by the PET of a small brain volume (voxel) with a low spatial resolution of about 2.5 mm and above (Moses, 2011).

Therefore, the Abeta transfer function is defined as

$$\begin{cases} \tau_i(\beta_a) = S^{-1}(\beta_a) \\ r_{\beta_a} = 2 \ln(S_{\text{max}} \cdot 1s - 1) / (\beta_{a,\text{off}} - \beta_{a,\text{max}}) \\ \beta_0 = (\beta_{a,\text{off}} + \beta_{a,\text{max}}) / 2, \end{cases} \quad (14)$$

wherein r_{β_a} is the slope of the sigmoid, β_0 is the midpoint of the sigmoid and the coefficients are chosen to fit the conditions explained before. In this function, τ_i appears as its reciprocal value τ_i^{-1} as it is implemented in the code of TVB. Because τ_i is a time in ms, the inverse of τ_i is a rate of potential change, and does not directly correspond to a firing rate. The Abeta load affects the inhibitory rate following a sigmoid curve. The rate ranges between S_{min} and S_{max} and the time constant ranges consequently between $1/S_{\text{max}}$ and $1/S_{\text{min}}$.

To simulate the model using TVB, physical space and time are discretized. The system of difference equations is then solved using deterministic Heun's method with a time step of 5 ms. We used a deterministic method to avoid stochastic influences since the simulation was performed in the absence of noise.

The system was integrated for 2 min and the last minute was analyzed in order to diminish transient components in the time series due to the initialization and settle the system into a steady state.

We explore a range of $0 \leq G \leq 600$ which provides an overview about the possible population level behaviors at different states of network coupling. Because the coupling factor G has a crucial influence on the external input on the neuronal

populations, this allows different regions to operate in different dynamical regimes, as it can be seen in the bifurcation diagrams of **Supplementary Figure 1**. Global coupling factor G that was sampled between $G = 0$ (i.e., isolated regions) and $G = 600$ with a step size of $\Delta G = 3$. The initial values were taken from 4,000 random time points for each state variable in each region. The length of 2 min for the simulations was chosen with the aim to diminish possible transient components due to the initialization of state variables at $t = 0$. For analysis we used only the second minute of the simulated signals. No time delays are implemented in the large-scale network interactions since they are not required for the emergence of the here evaluated features and setting them to zero increases reduces required computation resources.

Spectral Properties of the Simulated EEG

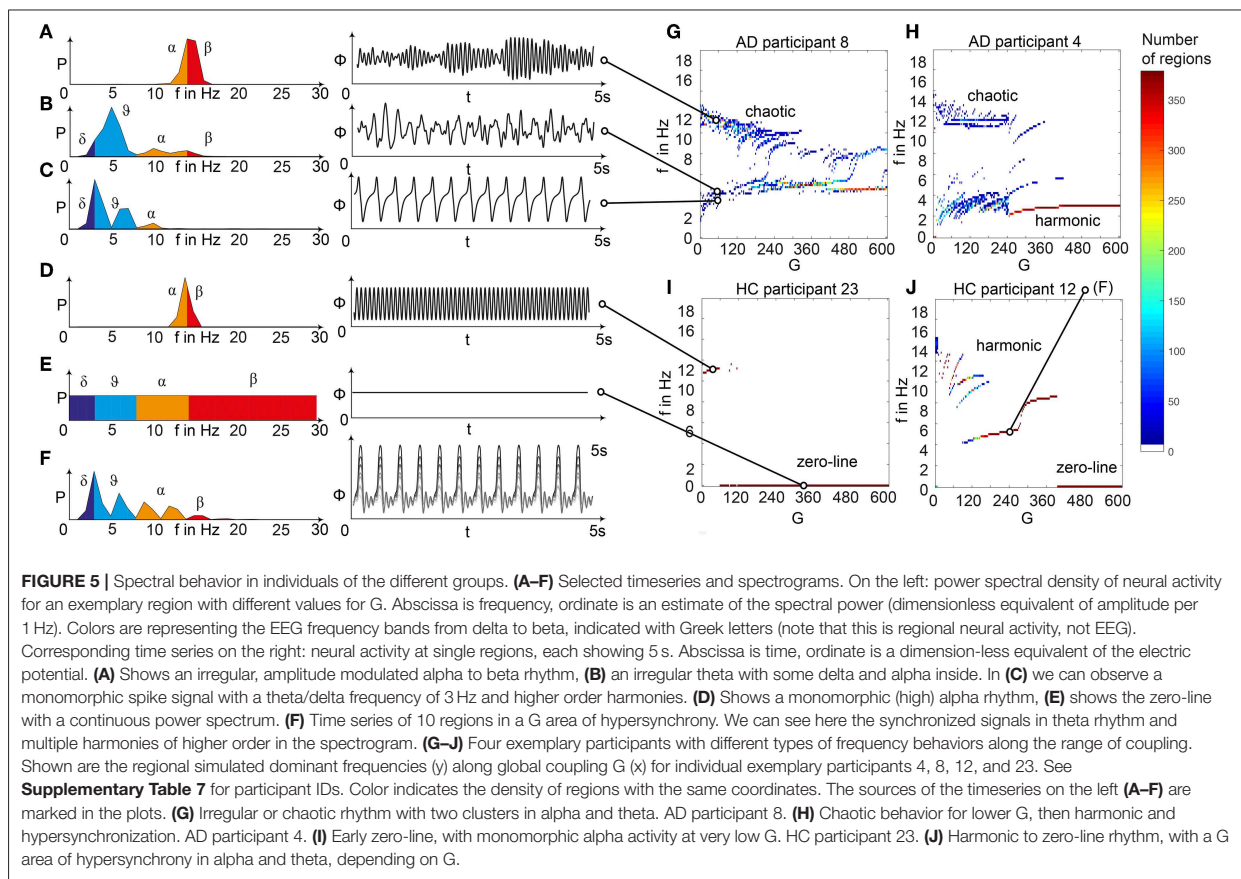
In TVB, we simulate EEG as a projection of the oscillating membrane potentials inside the brain via its electromagnetic fields to the skin surface of the head (Sanz-Leon et al., 2015) using the individual lead field matrices which take into account the different impedances of white matter, gray matter, external liquor space, pia and dura mater, the skull and the skin. Our lead-field matrices considered the impedances of three compartment borders: brain-skull, skull-scalp and scalp-air (Jirsa et al., 2002; Bojak et al., 2010; Litvak et al., 2011; Ritter et al., 2013). The postsynaptic membrane potential (PSP) considered for the projection is the one of the pyramidal cells, as they contribute the mayor part to potential changes in EEG (Kirschstein and Köhling, 2009). The PSP is calculated by summing the synaptic input from excitatory and inhibitory subpopulations to the pyramidal cells. The baseline PSP was derived as the mean PSP across time for every region. For the LFP or EEG peak frequency, we computed the power spectrum using the "periodogram" function of the Scipy python toolbox (Jones et al., 2001). From the spectrogram the "dominant rhythm" was identified as the frequency with the highest power.

RESULTS

Abeta-Inferred Dynamics Lead to Individual Spectral Patterns

We analyzed the dominant frequency in the simulated EEG and regional neural signal (referred to as local field potential (LFP) (**Figures 5G–J**)).

We observed a physiologically looking irregular behavior with two frequency clusters in the alpha and in the theta spectrum (**Figure 5G**). This behavior is expressed in the area of lower global coupling G for all 10 AD participants and in 3 out of 8 MCI and 4 out of 15 HC participants. The irregular time series and the broad continuous frequency spectra (**Figure 5B**) of network regime in $0 < G < 150$ are indicative for deterministic chaos. Such chaotic network regimes in a BNM have already been reported using the same local dynamic model [Figure 2 in Kunze et al. (2016)]. Beside this emerging chaotic behavior in our simulations other phenomena occurred in the parameter space exploration: a state of hypersynchronization between regions (**Figures 5H, J**) and a state of a "zero-line" with no oscillations that clearly does not reflect a physiological brain state (**Figures 5I, J**).



In order to locate the individual simulations in the spectrum of possible dynamics, meaning in the range of possible A_{β} load, we examined extreme values of A_{β} distribution. The virtual brains with a mean A_{β} load of zero (**Supplementary Figure 3A**) and with the maximum A_{β} load at all regions (**Supplementary Figure 3B**), we see as expected for the A_{β} -free system a behavior similar to the low- A_{β} -containing HC participants. This is not surprising, because when the HC subjects do not have a high A_{β} signal, the dynamics will converge to those with zero A_{β} , which is in fact then only determined by the underlying standard SC and therefore remains the same for all participants. However, the homogeneous application of maximum A_{β} burden does not lead to an AD-like pattern but shows a zero-line at the whole spectrum.

To give a mathematical explanation of those phenomena, we related each participants A_{β} -burden to the corresponding inhibitory time constant τ_i and used former analyses of the uncoupled local Jansen-Rit model (Spiegler et al., 2010) to estimate the bifurcation diagrams for the coupled system in this study (**Figure 6**). Shown diagrams allow to predict and explain the occurrence of alpha and theta rhythms or zero-lines depending on the underlying A_{β} burdens. The variation of τ_i by local A_{β} burden fundamentally influences the systems bifurcations by shifting the bifurcation point along the range

of external input to the pyramidal cells. As a consequence, different values of A_{β} lead to a variable occurrence of two limit cycles and a stable focus. Therefore, for a single region with constant external input on pyramidal cells, depending on A_{β} the region might be in an alpha limit cycle, in a theta limit cycle, in a bistable condition where both cycles are possible or in a stable focus.

Simulated EEG Slowing in AD Is Caused by Heterogeneous A_{β} Distribution

Figure 7 displays how the mean dominant rhythms differ between the groups. In the range below $G = 100$ we find a slowing in the AD group. Since in the range of lower G all three groups exhibit realistic frequency spectra and no zero-lines we consider this range of G as “physiological.” Significant differences appear between AD and non-AD for ranges of high and low G and also for high alpha and low theta rhythms (**Figure 7**). The heterogeneous distribution of A_{β} (in contrast to an averaged homogeneous distribution) plays a crucial role in the development of this AD-specific slowing. This is indicated by simulations with the mean averaged A_{β} of each participant mapped on all regions. The simulations revealed a regionally more homogenous behavior in all groups (**Supplementary Figure 4**). Moreover,

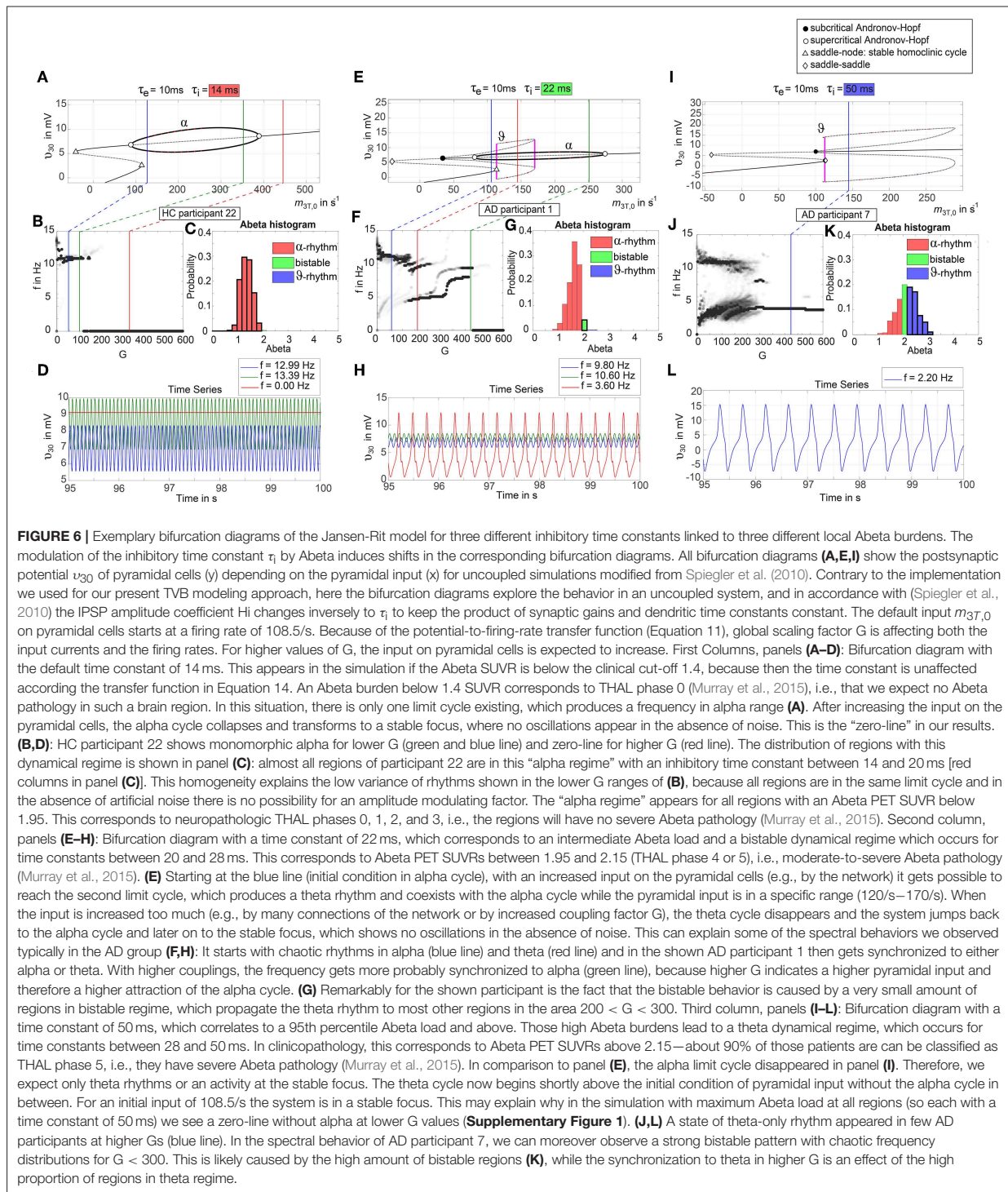
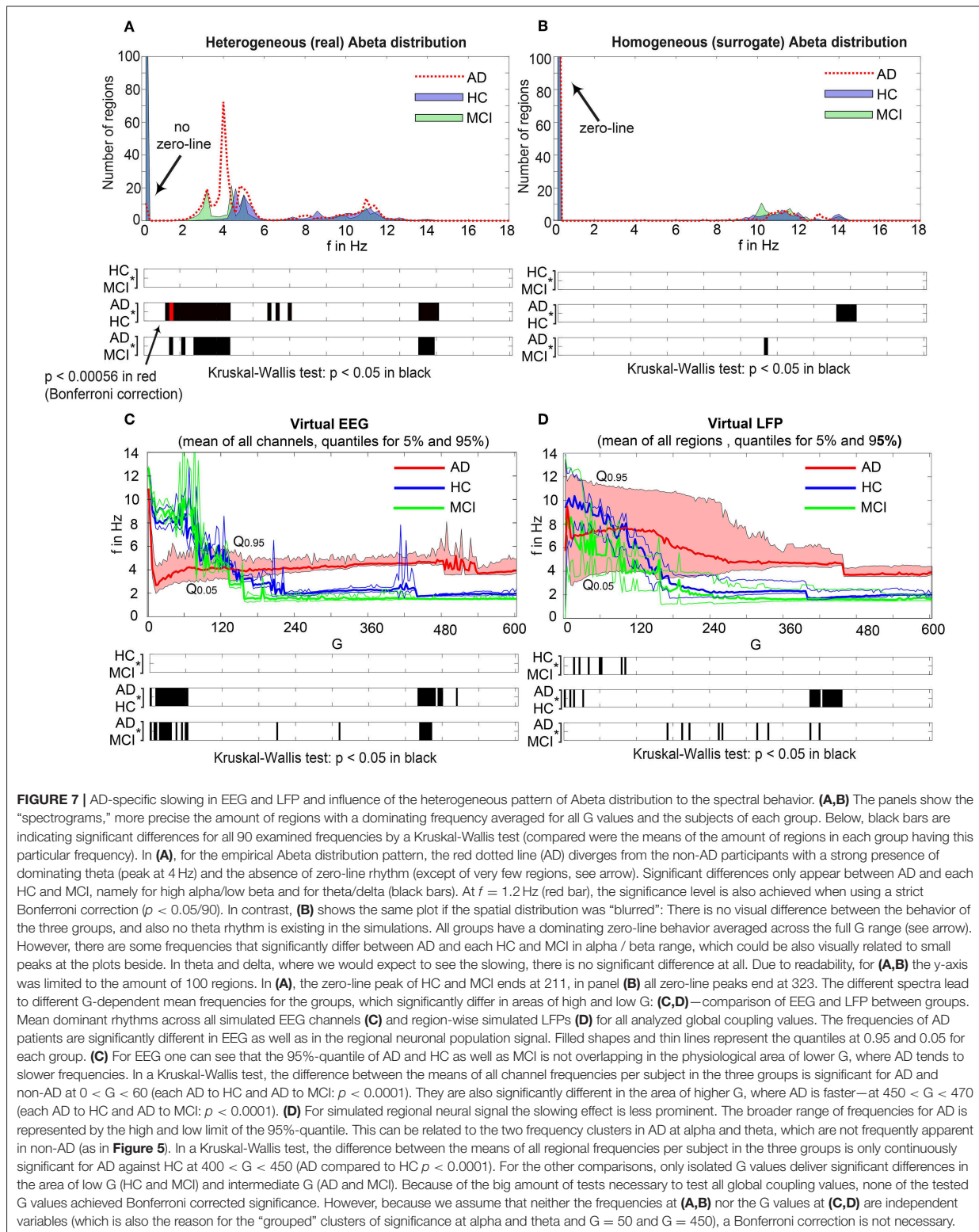


FIGURE 6 | Exemplary bifurcation diagrams of the Jansen-Rit model for three different inhibitory time constants linked to three different local Abeta burdens. The modulation of the inhibitory time constant τ_i by Abeta induces shifts in the corresponding bifurcation diagrams. All bifurcation diagrams (**A,E,I**) show the postsynaptic potential v_{30} of pyramidal cells (y) depending on the pyramidal input (x) for uncoupled simulations modified from Spiegler et al. (2010). Contrary to the implementation we used for our present TVB modeling approach, here the bifurcation diagrams explore the behavior in an uncoupled system, and in accordance with (Spiegler et al., 2010) the IPSP amplitude coefficient H_i changes inversely to τ_i to keep the product of synaptic gains and dendritic time constants constant. The default input $m_{37,0}$ on pyramidal cells starts at a firing rate of 108.5/s. Because of the potential-to-firing-rate transfer function (Equation 11), global scaling factor G is affecting both the input currents and the firing rates. For higher values of G , the input on pyramidal cells is expected to increase. First Column, panels (**A–D**): Bifurcation diagram with the default time constant of 14 ms. This appears in the simulation if the Abeta SUVR is below the clinical cut-off 1.4, because then the time constant is unaffected according to the transfer function in Equation 14. An Abeta burden below 1.4 SUVR corresponds to THAL phase 0 (Murray et al., 2015), i.e., that we expect no Abeta pathology in such a brain region. In this situation, there is only one limit cycle existing, which produces an alpha range (**A**). After increasing the input on the pyramidal cells, the alpha cycle collapses and transforms to a stable focus, where no oscillations appear in the absence of noise. This is the “zero-line” in our results. (**B,D**): HC participant 22 shows monomorphic alpha for lower G (green and blue line) and zero-line for higher G (red line). The distribution of regions with this dynamical regime is shown in panel (**C**): almost all regions of participant 22 are in this “alpha regime” with an inhibitory time constant between 14 and 20 ms [red columns in panel (**C**)]. This homogeneity explains the low variance of rhythms shown in the lower G ranges of (**B**), because all regions are in the same limit cycle and in the absence of artificial noise there is no possibility for an amplitude modulating factor. The “alpha regime” appears for all regions with an Abeta PET SUVR below 1.95. This corresponds to neuropathologic THAL phases 0, 1, 2, and 3, i.e., the regions will have no severe Abeta pathology (Murray et al., 2015). Second column, panels (**E–H**): Bifurcation diagram with a time constant of 22 ms, which corresponds to an intermediate Abeta load and a bistable dynamical regime which occurs for time constants between 20 and 28 ms. This corresponds to Abeta PET SUVRs between 1.95 and 2.15 (THAL phase 4 or 5), i.e., moderate-to-severe Abeta pathology (Murray et al., 2015). (**E**) Starting at the blue line (initial condition in alpha cycle), with an increased input on the pyramidal cells (e.g., by the network) it gets possible to reach the second limit cycle, which produces a theta rhythm and coexists with the alpha cycle while the pyramidal input is in a specific range (120/s–170/s). When the input is increased too much (e.g., by many connections of the network or by increased coupling factor G), the theta cycle disappears and the system jumps back to the alpha cycle and later on to the stable focus, which shows no oscillations in the absence of noise. This can explain some of the spectral behaviors we observed typically in the AD group (**F,H**): It starts with chaotic rhythms in alpha (blue line) and theta (red line) and in the shown AD participant 1 then gets synchronized to either alpha or theta. With higher couplings, the frequency gets more probably synchronized to alpha (green line), because higher G indicates a higher pyramidal input and therefore a higher attraction of the alpha cycle. (**G**) Remarkably for the shown participant is the fact that the bistable behavior is caused by a very small amount of regions in bistable regime, which propagate the theta rhythm to most other regions in the area $200 < G < 300$. Third column, panels (**I–L**): Bifurcation diagram with a time constant of 50 ms. In clinicopathology, this corresponds to Abeta PET SUVRs above 2.15—about 90% of those patients are can be classified as THAL phase 5, i.e., they have severe Abeta pathology (Murray et al., 2015). In comparison to panel (**E**), the alpha limit cycle disappeared in panel (**I**). Therefore, we expect only theta rhythms or an activity at the stable focus. The theta cycle now begins shortly above the initial condition of pyramidal input without the alpha cycle in between. For an initial input of 108.5/s the system is in a stable focus. This may explain why in the simulation with maximum Abeta load at all regions (so each with a time constant of 50 ms) we see a zero-line without alpha at lower G values (**Supplementary Figure 1**). (**J,L**) A state of theta-only rhythm appeared in few AD participants at higher G s (blue line). In the spectral behavior of AD participant 7, we can moreover observe a strong bistable pattern with chaotic frequency distributions for $G < 300$. This is likely caused by the high amount of bistable regions (**K**), while the synchronization to theta in higher G is an effect of the high proportion of regions in theta regime.

with homogeneous distribution of Abeta the slowing in AD participants does not appear: we don't see a significant change in the theta band (**Figure 7B**). This is a strong indicator for the importance of the individual Abeta distribution and a proof for the necessity of heterogeneous excitotoxic effects for the

creation of neural slowing. However, the absence of slowing in the simulations with homogeneous Abeta distribution does not proof the importance of a specific spatial Abeta pattern. In contrast, it only shows that there must be few regions with very high Abeta pathology to slow down the system (see **Figures 6F–G**).



Intra-individual Ratio of High vs. Low Abeta Burden Across All Regions Determines Simulated EEG Frequency Spectrum—Distinct Spatial Configurations of Abeta Do Not Matter for Slowing

We next examined how LFP/EEG slowing is related to the underlying Abeta burden (Figure 8). We revealed significant linear dependencies for all groups between Abeta burden and frequency. We found a strong inverse dependency for AD ($R^2 = 0.625$), i.e., an Abeta-dependent EEG slowing. In contrast, for non-AD participants the relation was revers, i.e., higher values of Abeta caused EEG acceleration.

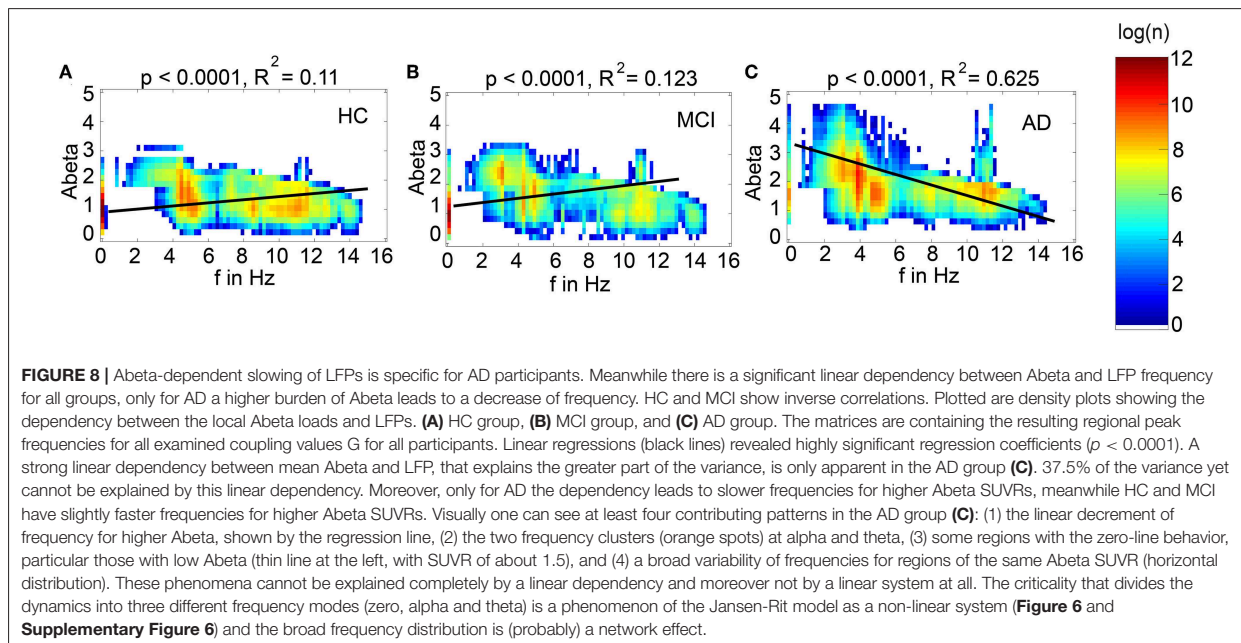
To test if specific regions are more important for the observed phenomena, we had to overcome the bias that only specific regions were strongly affected by Abeta. I.e., for the empirical Abeta distribution we cannot say e.g., for a region with high Abeta if it shows EEG/LFP slowing only because of its high Abeta value or because of its specific spatial and graph theoretical position in the network. Therefore, we next performed simulation with 10 random spatial distributions of the individual Abeta PET SUVRs for the 10 AD participants. In these simulations, the neural slowing appeared similarly to the empirical spatial distributions of Abeta (Supplementary Figure 5), which indicates a minor role of the distinct spatial patterns of Abeta. Instead, the ratio of regions corresponding to the three different dynamical regimes (alpha, theta, and bistable) determined the simulated frequency spectrum (Supplementary Figure 6). For an optimal value of G with $100 < G < 150$, the ratio of regions with an Abeta value in theta regime best corresponded to the ratio of regions with theta frequency in LFP. Moreover, the number of regions in different regimes enables to predict the individual spectral behavior across G . This analysis shows the crucial role of G for the

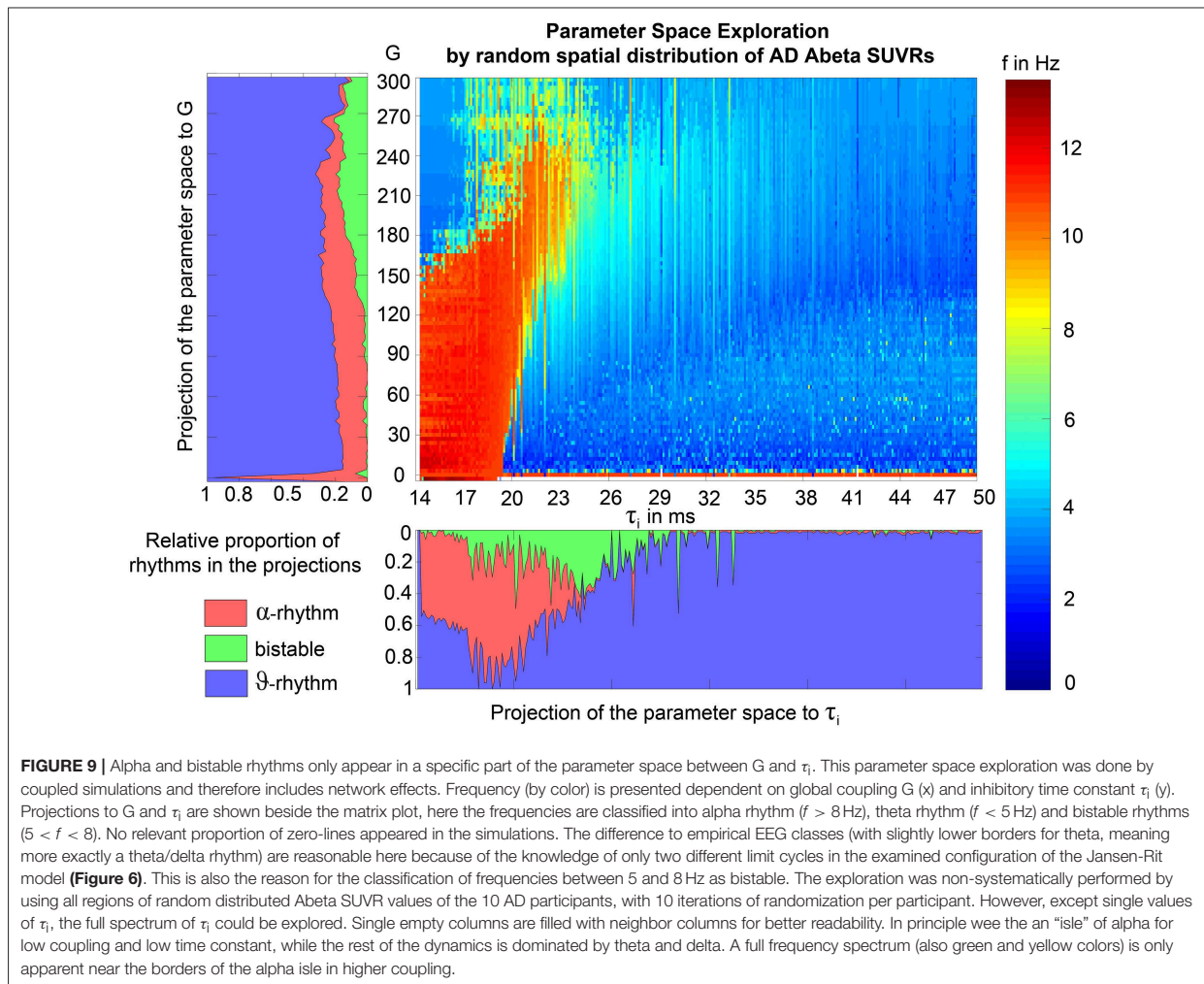
simulation dynamics. There might exist different optima of G —dependent on what phenomenon in the simulation is of interest. But for a specific phenomenon, in this case the correspondence of underlying Abeta PET to frequencies, we can find a narrow optimum of G wherein a specific behavior occurs.

The results of random spatial distribution of Abeta PET SUVRs were also used for a parameter space exploration (Figure 9). The analysis reveals that (1) alpha rhythms are only apparent for low time constants with $\tau_i < 30$ ms, but for the full spectrum of G , more probable for lower G values; (2) relevant amounts of bistable rhythms are only apparent for $17 \text{ ms} < \tau_i < 39 \text{ ms}$ and $G > 120$; (3) theta rhythms are present across almost the full spectra of G and τ_i , with an equal appearance across G , but with a local minimum at $\tau_i \approx 18$ ms, where the system is dominated by alpha and bistable rhythms. This exploration demonstrates two major insights. First, it confirms the crucial role of τ_i for the appearance of alpha or theta rhythms as we expect it out of the (non-coupled) bifurcation diagrams of Figure 6. Network effects are present (e.g., there are theta rhythms for low values of τ_i), but play a minor role here. Second, the value of G does not significantly affect the probability of theta rhythm, except of an alpha-theta shift for low $\tau_i < 20$ ms and higher $G > 160$. This is caused by the coexistence of stable focus in alpha regime and theta limit cycle in theta regime for high pyramidal input (Figures 6A,I).

Neural Slowing Propagates to Central Parts of the Network Independently of the Spatial Abeta Distribution

In the analysis of spatial distribution in relation to the organization of the underlying SC network (Figure 10), it can be seen that unless Abeta is distributed more peripherally, the





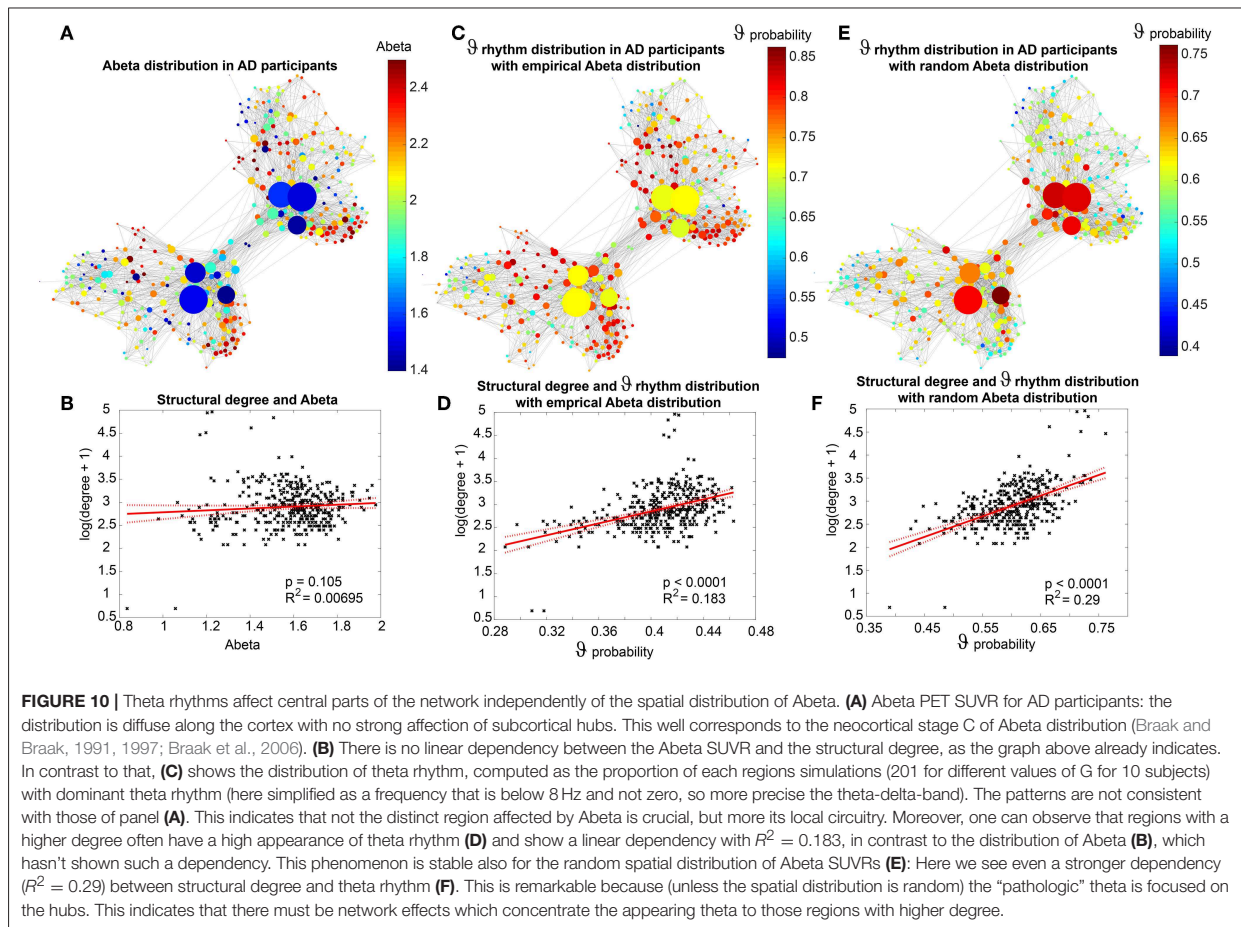
Abeta-dependent effect of neural slowing is focused to central parts of the network. Even a random distribution of Abeta SUVRs leads to this effect (Figures 10E,F), indicating that this is a network effect. Probably this phenomenon is caused because the slowing effects are not only affecting the region itself, but also its local circuitry and neighbored regions. Hubs with a high degree and many close neighbors are therefore more probable of being affected by slow rhythms propagated by other regions. To relate this to empirical facts: We know from our data (Figure 10A) that Abeta is not deposited in hubs, but more in peripheral regions of the networks. This shows, however, how the consecutive pathologic slowing effect is afterwards focused to central and important parts of the networks. A weak peripheral affection of the inhibitory system therefore disturbs the full system seriously.

Virtual Therapy With the NMDA Antagonist Memantine

The former analyses have shown that Abeta-mediated simulated hyperexcitation can lead to realistic changes of simulated brain

imaging signals in AD such as EEG slowing (Figures 5, 6). We therefore wanted to know if an established way to protect the brain of the hyperexcitation, which is the NMDA antagonist memantine, can lead to functional reversibility.

The idea in our model is now that in theory memantine acts anti-excitotoxic via its NMDA antagonism and should therefore be able to weaken the hyperexcitation we introduced to the system by Abeta (Figure 11). As mentioned above, the local coupling parameter c_{31} represents the main part of the glutamatergic transmission and can therefore also be seen as a surrogate of NMDAergic transmission (Figure 11A). We homogeneously increased the default value of c_{31} stepwise to observe the effects on the system. The analysis of the Jansen-Rit equilibria supports the concept of lower excitation introduced by lower c_{31} (Figures 11B,C). The equilibrium manifold is the manifold of fixed points (the equilibrium) that is projected onto the PSP at the pyramidal cells as a function of two parameters, that is, the local excitatory-to-pyramidal coupling coefficient c_{31} and the input on pyramidal cells $m_{3T,0}$. The manifold is the

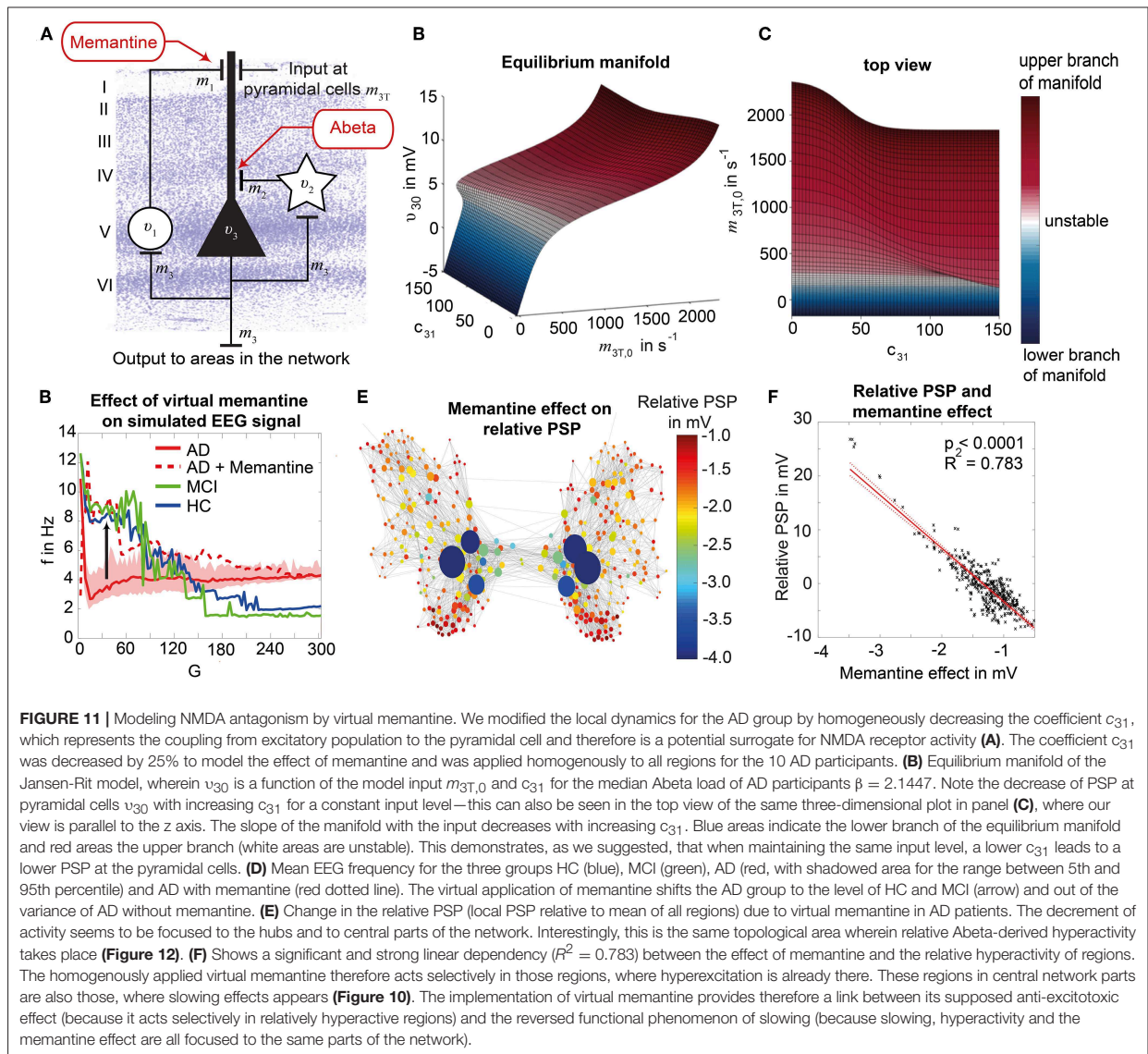


object onto which the system is moving or collapsing dependent on the parameters—in a way the equilibrium that underlies the dynamics of the system. The virtual memantine leads to a partial reversibility of the altered dominant frequencies in AD compared to HC/MCI (**Figure 11D**). Virtual memantine increases the mean dominant EEG frequency. These simulated functional effects do not imply reversibility of neurodegeneration, but they illustrate how pharmacological intervention can theoretically counteract those processes. This observation provides first a potential mechanistic explanation of the pharmacodynamics of memantine. Second, it shows that TVB in general and the Abeta-hyperexcitation model of this study in particular are able to test the efficacy of treatment strategies such as drugs and have therefore the potential to be used for the discovery of new treatment options. Finally, it supports the concept of this study, where the impaired inhibitory function is modeled by an increased synaptic delay and it indirectly indicates that higher Abeta (by increasing τ_i) has led to a local hyperexcitation. It is to mention, that in an uncoupled network both the decrease of c_{31} (memantine) and the increase of τ_i (by Abeta) would have the same effect (**Figures 11B,C, 13C,D**). In a coupled simulation, the effects are in contrast antagonistic. One reason for this seems to

be, that the effect of virtual memantine is focused to central parts of the network (**Figures 11E,F**)—the same parts, where slowing (**Figure 10**) and Abeta-derived hyperexcitation (**Figure 12**) are occurring. The homogeneously applied memantine evolves its action, guided by the topology of the SC network, along the same path as the hyperexcitation is distributed. The effects of altered delay of GABA transmission can be reversed by adjusting NMDA transmission at another subset of the local population model. This illustrates that theoretically an alteration of the inhibitory transmission dynamics may lead to disinhibition causing hyperexcitation in downstream populations, which is reversible by reduction of excitatory input.

DISCUSSION

Local Abeta-mediated disinhibition and hyperexcitation are considered candidate mechanisms of AD pathogenesis. In TVB simulations, the molecular candidate mechanism has led to macro-scale slowing in EEG and neural signal with a particular shift from alpha to theta previously observed in AD patients (Loewenstein et al., 1989; Rice et al., 1990; Dierks et al., 2000; Babiloni et al., 2016; Malek et al., 2017; Nakamura



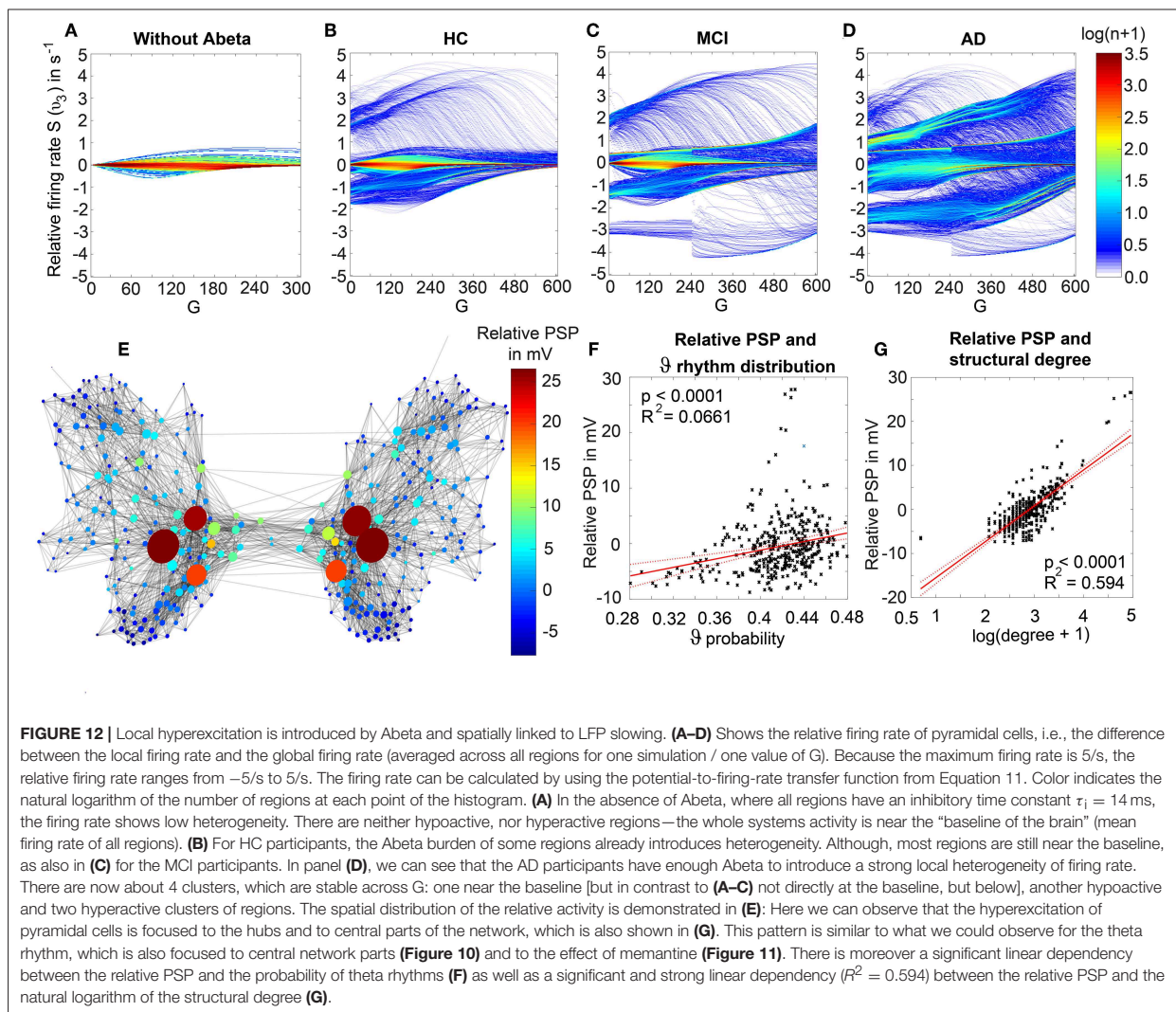
et al., 2018). These observations cannot be directly inferred by the hyperexcitation implemented in our model. Because we standardized all other factors and used a common SC for all simulations, this approach enables to examine the effects of locally altered E/I balance on an individual whole-brain level but without any other confounding factors.

We showed that the slowing in simulated EEG and LFP is specific for the AD group (Figures 7, 8). This offers an explanation, how the shift from alpha to theta, that is observable in EEG of AD patients (Loewenstein et al., 1989; Rice et al., 1990; Dierks et al., 2000; Babiloni et al., 2016; Malek et al., 2017; Nakamura et al., 2018), could be explained on a synaptic level—namely by an impaired inhibition. This computational modeling result supports the

findings of specific toxicity of Abeta to inhibitory neurons (Ripoli et al., 2014; Ulrich, 2015; Ren et al., 2018).

We demonstrate the computational principles underlying this Abeta dependent slowing of EEG/LFP (Figure 6, Supplementary Figure 6). Dependent on the Abeta burden alpha, theta or bistable regime develop caused by an alteration of the inhibitory time constant that leads to changes of the systems bifurcation behavior (Figure 6, Supplementary Figures 1, 2, 6).

The simulated LFP/EEG slowing in AD patients crucially depends on the spatially heterogenous Abeta distribution as measured by PET—the slowing disappears when using a homogeneously distributed mean Abeta burden instead for simulation (Figure 7). To exhibit the slowing effect few regions with high Abeta burden are required—while the



specific location of these regions seems not to be relevant (**Supplementary Figure 5**). The crucial factor for AD-specific slowing behavior in our simulations is the presence of very few regions that are strongly affected by Abeta (**Figure 6F** and middle column of **Supplementary Figure 6**).

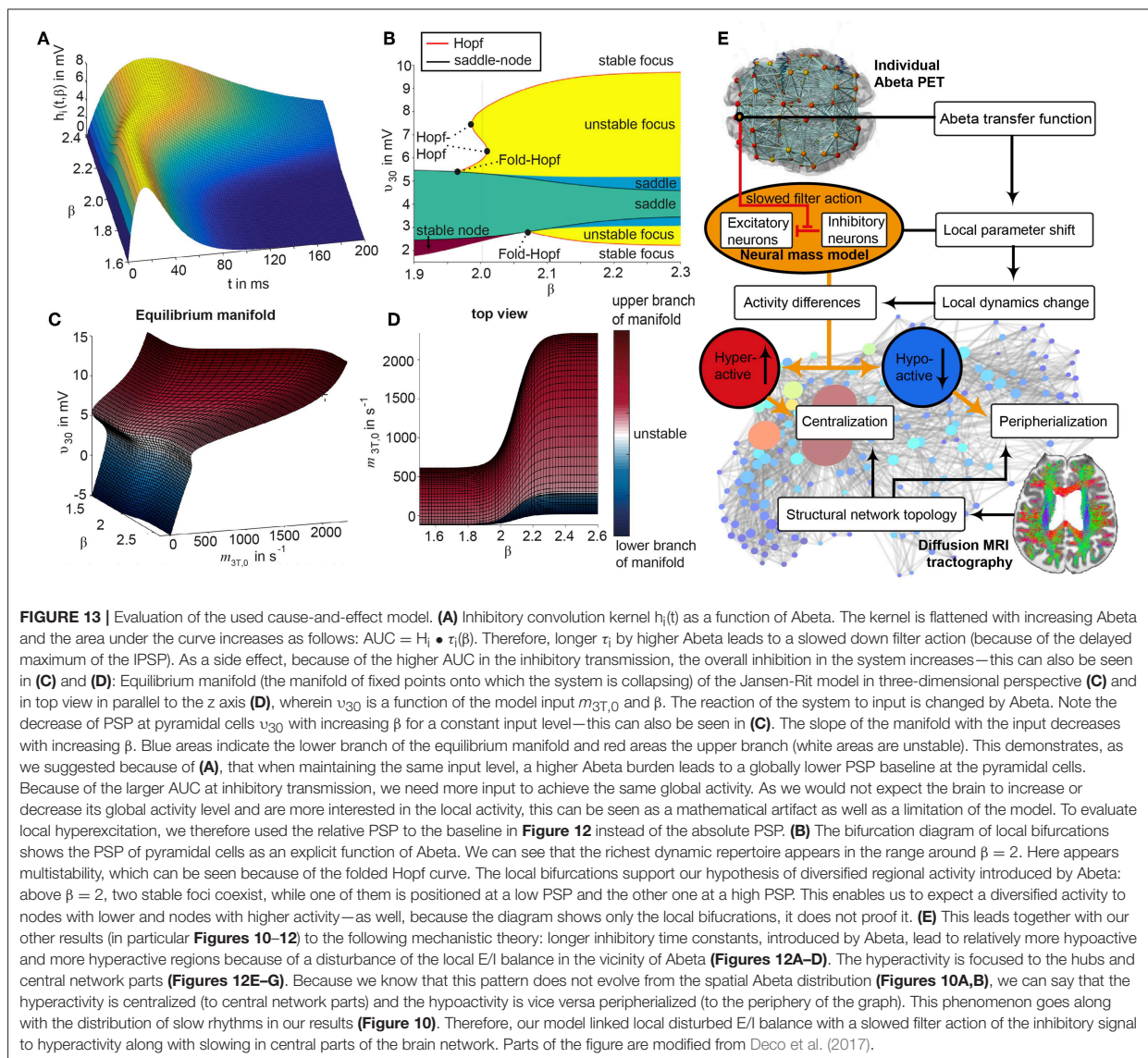
Independently of the location of high Abeta burdens in the simulated brain, slowing emerges at the core, i.e., hubs of the structural connectome (**Figure 10**). This indicates that the central parts of the system are impacted functionally by the Abeta burden. Moreover, it shows that while Abeta is often distributed in peripheral parts of the structural connectome, its functional consequences affect the important hubs. This could provide a possible explanation why a peripheral distribution of Abeta leads to severe disturbances of cognitive function.

Abeta leads by the disturbance of E/I balance to more local hyperexcitation (**Figure 12**). Because the range of activity is broader, we have more hypoactive and also more hyperactive

regions (**Figure 13**). The local hyperexcitation is strongly correlated with local LFP slowing (**Figure 10**) and also focused to the hubs of the network (**Figure 12**).

We also showed that the drug memantine that is known for improving brain function in severe AD can be modeled by a decreased transmission between the excitatory interneurons and the pyramidal cells and is able to achieve a “normalized” brain function *in silico*, too (**Figure 11**). Its effect is evokes selectively in hyperactive regions and in those parts of the network, where slow rhythms appear. This moreover demonstrates the potential of TVB to test and develop new treatment strategies.

One major limitation of this study is the lack of direct validation of the simulated electrophysiological phenomena. Neither EEG nor LFP data was available in the ADNI-3 cohort. Although EEG slowing in AD is an established concept (Loewenstein et al., 1989; Rice et al., 1990; Dierks et al., 2000; Babiloni et al., 2016; Malek et al., 2017; Nakamura et al., 2018),



future studies will have to validate the simulated data directly with individual EEG.

The second important limitation is the implementation of disturbed E/I balance by the inhibitory time constant. Although the longer time constants lead to slowed filter action (**Figure 13A**) and local hyperexcitation at important network structures (**Figure 12**), the global activity is decreased for the same input level. To overcome this model limitation, it would be necessary to correct the input level, e.g., by increasing the default input $m_{3T,0}$ with higher mean Abeta burdens or by increasing a coefficient inside the IRF (Equation 2) to keep the AUC and therefore the transmitted energy at inhibitory transmission constant. This should be examined in future studies to evaluate the effect of such a correction.

However, this would only be necessary if the global activity level would be a target of interest for another research question. Because of the feedback loops in a coupled brain network, each introduction of over- or dis-inhibition will lead both to hypo- and hyper-active regions. An analysis of hyperactivity needs therefore always a control activity—because hyperactivity can be meant spatially, temporally, or dependent on other factors. In our model, we could introduce spatially distributed hyperactivity (**Figure 12**) that was linked to local slowing (**Figure 10**), network topology (**Figures 12E–G**) and could be antagonized selectively by virtual memantine (**Figure 11**).

The differential equations that describe the differential equations that describe Of course the pathophysiological model

presented in this study can only cover a small subspace of possible AD mechanisms. Even Abeta itself is probably only one player in the multifactorial pathogenesis (Selkoe and Hardy, 2016; Gauthier et al., 2018), and synaptic disinhibition is only one of its effects (Furukawa et al., 1996; Good et al., 1996; Hardy and Selkoe, 2002; Chen, 2005; Busche et al., 2012; Prasansuklab and Tencomnao, 2013; Bloom, 2014; Sadigh-Eteghad et al., 2015; Song et al., 2015; Ulrich, 2015; Celebi et al., 2016; Gauthier et al., 2018; Ren et al., 2018). We are fully aware that other major hallmarks as Tau (Bloom, 2014; Guo et al., 2017; Tapia-Rojas et al., 2019) and cardiovascular risk factors (Love and Miners, 2016; Storck and Pietrzik Claus, 2018; Bannai et al., 2019) cannot be excluded in the discussion of AD etiology, as well as alternative concepts such as microglia and neuroinflammation (Heneka et al., 2015a,b; Wang and Colonna, 2019; Zhou et al., 2019), polygenic risk factors (Mahley, 2016; Hudry et al., 2019; Jansen et al., 2019; Takatori et al., 2019), environmental factors as neurotoxic or infectious agents (Alonso et al., 2018; McLachlan et al., 2019), and concomitant proteinopathies (Robinson et al., 2018a,b).

Another limitation is the small sample size of 33 participants. Future studies will have to consider much more participants, which will then help to formulate even more general conclusions. However, because of emergent effects in the brain simulation, differences between the groups were often very relevant and significant. An overview of all used statistical test in this study can be found in **Supplementary Table 8**.

However, we present a first proof of concept for linking molecular changes as detected by PET to large-scale brain modeling using the simulation framework TVB. This study therefore can work as a blueprint for future approaches in computational brain modeling bridging scales of neural function. For the research on AD pathogenesis, this study provides a possible mechanistic explanation that links Abeta-related synaptic disinhibition at the micro-scale to AD-specific EEG slowing. In general, our study can be seen as proof of concept that TVB enables research on disease mechanisms at a multi-scale level and has potential to lead to improved diagnostics and to the discovery of new treatments.

DATA AVAILABILITY

The raw data for this study is available in ADNI. The codes used in this study are available on request to the corresponding author.

ETHICS STATEMENT

This study has been approved from the Ethics Board of the Charité - Universitätsmedizin Berlin under the approval number EA2/100/19.

AUTHOR CONTRIBUTIONS

All authors have made substantial intellectual contributions to this work and approved it for publication. LS and PR had

the idea to this study. LS, PT, ASp, and PR developed the concept and study design. LS wrote the manuscript, conducted the analysis and interpretation of results, and developed the figures. PT performed the MRI and PET image processing and supercomputer simulations. PT, ASp, M-AD-C, ASo, VJ, AM, and PR contributed to the interpretation of the results, figure development, and writing of the manuscript.

FUNDING

Data collection and sharing for this project was funded by the Alzheimer's Disease Neuroimaging Initiative (ADNI) (National Institutes of Health Grant U01 AG024904) and DOD ADNI (Department of Defense award number W81XWH-12-2-0012). ADNI is funded by the National Institute on Aging, the National Institute of Biomedical Imaging and Bioengineering, and through generous contributions from the following: AbbVie, Alzheimer's Association; Alzheimer's Drug Discovery Foundation; Araclon Biotech; BioClinica, Inc.; Biogen; Bristol-Myers Squibb Company; CereSpir, Inc.; Cogstate; Eisai Inc.; Elan Pharmaceuticals, Inc.; Eli Lilly and Company; EuroImmun; F. Hoffmann-La Roche Ltd and its affiliated company Genentech, Inc.; Fujirebio; GE Healthcare; IXICO Ltd.; Janssen Alzheimer Immunotherapy Research and Development, LLC.; Johnson and Johnson Pharmaceutical Research and Development LLC.; Lumosity; Lundbeck; Merck and Co., Inc.; Meso Scale Diagnostics, LLC.; NeuroRx Research; Neurotrack Technologies; Novartis Pharmaceuticals Corporation; Pfizer Inc.; Piramal Imaging; Servier; Takeda Pharmaceutical Company; and Transition Therapeutics. The Canadian Institutes of Health Research is providing funds to support ADNI clinical sites in Canada. Private sector contributions are facilitated by the Foundation for the National Institutes of Health (www.fnih.org). The grantee organization is the Northern California Institute for Research and Education, and the study is coordinated by the Alzheimer's Therapeutic Research Institute at the University of Southern California. ADNI data are disseminated by the Laboratory for Neuro Imaging at the University of Southern California.

PR acknowledges the following funding sources: H2020 Research and Innovation Action grants 826421 and 650003, 720270 and 785907, and ERC 683049; German Research Foundation CRC 1315 and 936, and RI 2073/6-1; Berlin Institute of Health and Foundation Charité, Johanna Quandt Excellence Initiative.

We acknowledge support from the German Research Foundation (DFG) and the Open Access Publication Fund of Charité—Universitätsmedizin Berlin.

Further we acknowledge Lea Doppelbauer and Jan Roediger for their helpful discussions.

SUPPLEMENTARY MATERIAL

The Supplementary Material for this article can be found online at: <https://www.frontiersin.org/articles/10.3389/fncom.2019.00054/full#supplementary-material>

REFERENCES

- Alonso, R., Pisa, D., Fernandez-Fernandez, A. M., and Carrasco, L. (2018). Infection of fungi and bacteria in brain tissue from elderly persons and patients with Alzheimer's disease. *Front. Aging Neurosci.* 10:159. doi: 10.3389/fnagi.2018.00159
- Alzheimer's Association (2018). 2018 Alzheimer's disease facts and figures. *Alzheimer's Dement.* 14, 367–429. doi: 10.1016/j.jalz.2018.02.001
- Babiloni, C., Del Percio, C., Caroli, A., Salvatore, E., Nicolai, E., Marzano, N., et al. (2016). Cortical sources of resting state EEG rhythms are related to brain hypometabolism in subjects with Alzheimer's disease: an EEG-PET study. *Neurobiol. Aging* 48, 122–134. doi: 10.1016/j.neurobiolaging.2016.08.021
- Bannai, T., Mano, T., Chen, X., Ohtomo, G., Ohtomo, R., Tsuchida, T., et al. (2019). Chronic cerebral hypoperfusion shifts the equilibrium of amyloid beta oligomers to aggregation-prone species with higher molecular weight. *Sci. Rep.* 9:2827. doi: 10.1038/s41598-019-39494-7
- Biogen (2019). *Biogen and Eisai to discontinue phase 3 engage and emerge trials of aducanumab in Alzheimer's disease 2019 [04/01/2019]*. Available online at: <http://investors.biogen.com/news-releases/news-release-details/biogen-and-eisai-discontinue-phase-3-engage-and-emerge-trials>
- Blennow, K., de Leon, M. J., and Zetterberg, H. (2006). Alzheimer's disease. *Lancet* 368, 387–403. doi: 10.1016/S0140-6736(06)69113-7
- Bloom, G. S. (2014). Amyloid- β and tau: The trigger and bullet in Alzheimer disease pathogenesis. *JAMA Neurol.* 71, 505–508. doi: 10.1001/jamaneurol.2013.5847
- Bojak, I., Oostendorp, T. F., Reid, A. T., and Kotter, R. (2010). Connecting mean field models of neural activity to EEG and fMRI data. *Brain Topogr.* 23, 139–149. doi: 10.1007/s10548-010-0140-3
- Braak, H., Alafuzoff, I., Arzberger, T., Kretschmar, H., Del Tredici, K. (2006). Staging of Alzheimer disease-associated neurofibrillary pathology using paraffin sections and immunocytochemistry. *Acta Neuropathol.* 112, 389–404. doi: 10.1007/s00401-006-0127-z
- Braak, H., and Braak, E. (1991). Neuropathological staging of Alzheimer-related changes. *Acta Neuropathol.* 82, 239–259. doi: 10.1007/BF00308809
- Braak, H., and Braak, E. (1997). Frequency of stages of Alzheimer-related lesions in different age categories. *Neurobiol. Aging* 18, 351–357. doi: 10.1016/S0197-4580(97)00056-0
- Breakspear, M. (2017). Dynamic models of large-scale brain activity. *Nat. Neurosci.* 20, 340–352. doi: 10.1038/nn.4497
- Busche, M. A., Chen, X., Henning, H. A., Reichwald, J., Staufenbiel, M., Sakmann, B., et al. (2012). Critical role of soluble amyloid-beta for early hippocampal hyperactivity in a mouse model of Alzheimer's disease. *Proc. Natl. Acad. Sci. U.S.A.* 109, 8740–8745. doi: 10.1073/pnas.1206171109
- Busche, M. A., Eichhoff, G., Adelsberger, H., Abramowski, D., Wiederhold, K. H., Haass, C., et al. (2008). Clusters of hyperactive neurons near amyloid plaques in a mouse model of Alzheimer's disease. *Science* 321, 1686–1689. doi: 10.1126/science.1162844
- Cabral, J., Kringelbach, M. L., and Deco, G. (2017). Functional connectivity dynamically evolves on multiple time-scales over a static structural connectome: models and mechanisms. *Neuroimage* 160, 84–96. doi: 10.1016/j.neuroimage.2017.03.045
- Celebi, O., Uzdogan, A., Oguz, K. K., Has, A. C., Dolgun, A., Cakmakli, G. Y., et al. (2016). Default mode network connectivity is linked to cognitive functioning and CSF A β 1-42 levels in Alzheimer's disease. *Arch. Gerontol. Geriatr.* 62, 125–132. doi: 10.1016/j.archger.2015.09.010
- Chen, C. (2005). beta-Amyloid increases dendritic Ca $^{2+}$ influx by inhibiting the A-type K $^{+}$ current in hippocampal CA1 pyramidal neurons. *Biochem. Biophys. Res. Commun.* 338, 1913–1919. doi: 10.1016/j.bbrc.2005.10.169
- Chen, R., Chan, P. T., Chu, H., Lin, Y. C., Chang, P. C., Chen, C. Y., et al. (2017). Treatment effects between monotherapy of donepezil versus combination with memantine for Alzheimer disease: a meta-analysis. *PLoS ONE* 12:e0183586. doi: 10.1371/journal.pone.0183586
- Chiao, P., Bedell, B. J., Avants, B., Zijdenbos, A. P., Grand'Maison, M., O'Neill, P., et al. (2019). Impact of reference and target region selection on amyloid PET SUV ratios in the phase 1b PRIME study of Aducanumab. *J. Nucl. Med.* 60, 100–106. doi: 10.2967/jnumed.118.209130
- Clark, C. M., Schneider, J. A., Bedell, B. J., Beach, T. G., Bilker, W. B., Mintun, M. A., et al. (2011). Use of florbetapir-pet for imaging β -amyloid pathology. *JAMA.* 305, 275–283. doi: 10.1001/jama.2010.2008
- David, O., and Friston, K. J. (2003). A neural mass model for MEG/EEG: coupling and neuronal dynamics. *NeuroImage* 20, 1743–1755. doi: 10.1016/j.neuroimage.2003.07.015
- David, O., Kiebel, S. J., Harrison, L. M., Mattout, J., Kilner, J. M., and Friston, K. J. (2006). Dynamic causal modeling of evoked responses in EEG and MEG. *NeuroImage* 30, 1255–1272. doi: 10.1016/j.neuroimage.2005.10.045
- Deco, G., Jirsa, V. K., Robinson, P. A., Breakspear, M., and Friston, K. (2008). The dynamic brain: from spiking neurons to neural masses and cortical fields. *PLoS Comput. Biol.* 4:e1000092. doi: 10.1371/journal.pcbi.1000092
- Deco, G., Kringelbach, M. L., Jirsa, V. K., and Ritter, P. (2017). The dynamics of resting fluctuations in the brain: metastability and its dynamical cortical core. *Sci. Rep.* 7:3095. doi: 10.1038/s41598-017-03073-5
- Dierks, T., Jelic, V., Pascual-Marqui, R. D., Wahlund, L., Julin, P., Linden, D. E., et al. (2000). Spatial pattern of cerebral glucose metabolism (PET) correlates with localization of intracerebral EEG-generators in Alzheimer's disease. *Clin. Neurophysiol.* 111, 1817–1824. doi: 10.1016/S1388-2457(00)00427-2
- Doggrell, S. A. (2018). Grasping at straws: the failure of solanezumab to modify mild Alzheimer's disease. *Expert Opin. Biol. Ther.* 18, 1189–1192. doi: 10.1080/14712598.2018.1543397
- Falcon, M. I., Riley, J. D., Jirsa, V., McIntosh, A. R., Elinor Chen, E., and Solodkin, A. (2016). Functional mechanisms of recovery after chronic stroke: modeling with the virtual brain. *eNeuro* 3:ENEURO.0158-15.2016. doi: 10.1523/ENEURO.0158-15.2016
- Falcon, M. I., Riley, J. D., Jirsa, V., McIntosh, A. R., Shereen, A. D., Chen, E. E., et al. (2015). The virtual brain: modeling biological correlates of recovery after chronic stroke. *Front. Neurol.* 6:228. doi: 10.3389/fneur.2015.00228
- Freeman, W. J. (ed) (1975). *Mass Action in the Nervous System*. San Diego, CA: Academic Press.
- Fruchterman, T. M. J., and Reingold, E. M. (1991). Graph drawing by force-directed placement. *Softw. Pract. Exper.* 21, 1129–1164. doi: 10.1002/spe.4380211102
- Furukawa, K., Barger, S. W., Blalock, E. M., and Mattson, M. P. (1996). Activation of K $^{+}$ channels and suppression of neuronal activity by secreted beta-amyloid-precursor protein. *Nature* 379, 74–78. doi: 10.1038/379074a0
- Gauthier, S., Zhang, H., Ng, K. P., Pascoal, T. A., and Rosa-Neto, P. (2018). Impact of the biological definition of Alzheimer's disease using amyloid, tau and neurodegeneration (ATN): what about the role of vascular changes, inflammation, Lewy body pathology? *Transl. Neurodegen.* 7:12. doi: 10.1186/s40035-018-0117-9
- Ghosh, A., Rho, Y., McIntosh, A. R., Kotter, R., and Jirsa, V. K. (2008). Noise during rest enables the exploration of the brain's dynamic repertoire. *PLoS Comput. Biol.* 4:e1000196. doi: 10.1371/journal.pcbi.1000196
- Glasser, M. F., Coalson, T. S., Robinson, E. C., Hacker, C. D., Harwell, J., Yacoub, E., et al. (2016). A multi-modal parcellation of human cerebral cortex. *Nature* 536, 171–178. doi: 10.1038/nature18933
- Glasser, M. F., Sotiropoulos, S. N., Wilson, J. A., Coalson, T. S., Fischl, B., Andersson, J. L., et al. (2013). The minimal preprocessing pipelines for the human connectome project. *Neuroimage* 80, 105–124. doi: 10.1016/j.neuroimage.2013.04.127
- Good, T. A., Smith, D. O., and Murphy, R. M. (1996). Beta-amyloid peptide blocks the fast-inactivating K $^{+}$ current in rat hippocampal neurons. *Biophys. J.* 70, 296–304. doi: 10.1016/S0006-3495(96)79570-X
- Grienberger, C., Rochefort, N. L., Adelsberger, H., Henning, H. A., Hill, D. N., Reichwald, J., et al. (2012). Staged decline of neuronal function *in vivo* in an animal model of Alzheimer's disease. *Nat. Commun.* 3:774. doi: 10.1038/ncomms1783
- Guo, T., Noble, W., and Hanger, D. P. (2017). Roles of tau protein in health and disease. *Acta Neuropathol.* 133, 665–704. doi: 10.1007/s00401-017-1707-9
- Hardy, J., and Selkoe, D. J. (2002). The amyloid hypothesis of Alzheimer's disease: progress and problems on the road to therapeutics. *Science* 297, 353–356. doi: 10.1126/science.1072994
- Hazra, A., Gu, F., Aulakh, A., Berridge, C., Eriksen, J. L., and Ziburkus, J. (2013). Inhibitory neuron and hippocampal circuit dysfunction in an aged mouse model of Alzheimer's disease. *PLoS ONE* 8:e64318. doi: 10.1371/journal.pone.0064318

- Heneka, M. T., Carson, M. J., Khoury, J. E., Landreth, G. E., Brosseron, F., Feinstein, D. L., et al. (2015a). Neuroinflammation in Alzheimer's disease. *Lancet Neurol.* 14, 388–405. doi: 10.1016/S1474-4422(15)70016-5
- Heneka, M. T., Golenbock, D. T., and Latz, E. (2015b). Innate immunity in Alzheimer's disease. *Nat. Immunol.* 16:229. doi: 10.1038/ni.3102
- Hindmarsh, J., and Rose, R. (1984). A model of neuronal bursting using three coupled first order differential equations. *Proc. R. Soc. London B Biol. Sci.* 221, 87–102. doi: 10.1098/rspb.1984.0024
- Honey, C. J., Kotter, R., Breakspear, M., and Sporns, O. (2007). Network structure of cerebral cortex shapes functional connectivity on multiple time scales. *Proc. Natl. Acad. Sci. U.S.A.* 104, 10240–10245. doi: 10.1073/pnas.0701519104
- Honig, L. S., Vellas, B., Woodward, M., Boada, M., Bullock, R., Borrie, M., et al. (2018). Trial of solanezumab for mild dementia due to Alzheimer's disease. *N. Engl. J. Med.* 378, 321–330. doi: 10.1056/NEJMoa1705971
- Hudry, E., Klickstein, J., Cannavo, C., Jackson, R., Muzikansky, A., Gandhi, S., et al. (2019). Opposing roles of apolipoprotein E in aging and neurodegeneration. *Life Sci. Alliance* 2:e201900325. doi: 10.26508/lsa.201900325
- Jack, C. R., Wiste, H. J., Weigand, S. D., Rocca, W. A., Knopman, D. S., Mielke, M. M., et al. (2014). Age-specific population frequencies of amyloidosis and neurodegeneration among cognitively normal people age 50–89 years: a cross-sectional study. *Lancet Neurol.* 13, 997–1005. doi: 10.1016/S1474-4422(14)70194-2
- Jack, C. R. Jr., Bennett, D. A., Blennow, K., Carrillo, M. C., Dunn, B., Haeberlein, S. B., et al. (2018). NIA-AA Research Framework: Toward a biological definition of Alzheimer's disease. *Alzheimer's Dement. J. Alzheimer's Assoc.* 14, 535–562. doi: 10.1016/j.jalz.2018.02.018
- Jack, C. R. Jr., Lowe, V. J., Weigand, S. D., Wiste, H. J., Senjem, M. L., Knopman, D. S., et al. (2009). Serial PIB and MRI in normal, mild cognitive impairment and Alzheimer's disease: implications for sequence of pathological events in Alzheimer's disease. *Brain* 132(Pt 5), 1355–1365. doi: 10.1093/brain/awp062
- Jansen, B. H., and Rit, V. G. (1995). Electroencephalogram and visual evoked potential generation in a mathematical model of coupled cortical columns. *Biol. Cybern.* 73, 357–366. doi: 10.1007/BF00199471
- Jansen, I. E., Savage, J. E., Watanabe, K., Bryois, J., Williams, D. M., Steinberg, S., et al. (2019). Genome-wide meta-analysis identifies new loci and functional pathways influencing Alzheimer's disease risk. *Nat. Genet.* 51, 404–413. doi: 10.1038/s41588-018-0311-9
- Jenkinson, M., Beckmann, C. F., Behrens, T. E., Woolrich, M. W., and Smith, S. M. (2012). FSL. *Neuroimage* 62, 782–790. doi: 10.1016/j.neuroimage.2011.09.015
- Jirsa, V. K. (2009). Neural field dynamics with local and global connectivity and time delay. *Philos. Trans. A Math. Phys. Eng. Sci.* 367, 1131–1143. doi: 10.1098/rsta.2008.0260
- Jirsa, V. K., Jantzen, K. J., Fuchs, A., and Kelso, J. A. S. (2002). Spatiotemporal forward solution of the EEG and MEG using network modeling. *IEEE Trans. Med. Imag.* 21, 493–504. doi: 10.1109/TMI.2002.1009385
- Jirsa, V. K., and Kelso, J. A. S. (2000). Spatiotemporal pattern formation in neural systems with heterogeneous connection topologies. *Phys. Rev. E* 62, 8462–8465. doi: 10.1103/PhysRevE.62.8462
- Jirsa, V. K., Proix, T., Perdikis, D., Woodman, M. M., Wang, H., Gonzalez-Martinez, J., et al. (2017). The virtual epileptic patient: individualized whole-brain models of epilepsy spread. *Neuroimage* 145(Pt B), 377–388. doi: 10.1016/j.neuroimage.2016.04.049
- Jirsa, V. K., Sporns, O., Breakspear, M., Deco, G., and McIntosh, A. R. (2010). Towards the virtual brain: network modeling of the intact and the damaged brain. *Arch. Ital. Biol.* 148, 189–205. doi: 10.4449/aib.v148i3.1223
- Jones, E., Oliphant, E., and Peterson, P. (2001). *SciPy: Open Source Scientific Tools for Python*. Available online at: <http://www.scipy.org/> (accessed July 30, 2019).
- Kirschstein, T., and Köhling, R. (2009). What is the source of the EEG? *Clin. EEG Neurosci.* 40, 146–149. doi: 10.1177/155005940904000305
- Kishi, T., Matsunaga, S., Oya, K., Nomura, I., Ikuta, T., and Iwata, N. (2017). Memantine for Alzheimer's disease: an updated systematic review and meta-analysis. *J. Alzheimers Dis.* 60, 401–425. doi: 10.3233/JAD-170424
- Klunk, W. E., Price, J. C., Mathis, C. A., Tsopelas, N. D., Lopresti, B. J., Ziolko, S. K., et al. (2007). Amyloid deposition begins in the striatum of presenilin-1 mutation carriers from two unrelated pedigrees. *J. Neurosci.* 27, 6174–6184. doi: 10.1523/JNEUROSCI.0730-07.2007
- Kringelbach, M. L., McIntosh, A. R., Ritter, P., Jirsa, V. K., and Deco, G. (2015). The rediscovery of slowness: exploring the timing of cognition. *Trends Cogn. Sci.* 19, 616–628. doi: 10.1016/j.tics.2015.07.011
- Kunze, T., Hunold, A., Hauelsen, J., Jirsa, V., and Spiegler, A. (2016). Transcranial direct current stimulation changes resting state functional connectivity: a large-scale brain network modeling study. *NeuroImage* 140, 174–187. doi: 10.1016/j.neuroimage.2016.02.015
- Limon, A., Reyes-Ruiz, J. M., and Milei, R. (2012). Loss of functional GABA(A) receptors in the Alzheimer diseased brain. *Proc. Natl. Acad. Sci. U.S.A.* 109, 10071–10076. doi: 10.1073/pnas.1204606109
- Litvak, V., Mattout, J., Kiebel, S., Phillips, C., Henson, R., Kilner, J., et al. (2011). EEG and MEG data analysis in SPM8. *Comput. Intell. Neurosci.* 2011:852961. doi: 10.1155/2011/852961
- Loewenstein, D. A., Barker, W. W., Chang, J. Y., Apicella, A., Yoshii, F., Kothari, P., et al. (1989). Predominant left hemisphere metabolic dysfunction in dementia. *Arch. Neurol.* 46, 146–152. doi: 10.1001/archneur.1989.00520380046012
- Logovinsky, V., Satlin, A., Lai, R., Swanson, C., Kaplow, J., Osswald, G., et al. (2016). Safety and tolerability of BAN2401 - a clinical study in Alzheimer's disease with a protofibril selective A β antibody. *Alzheimer's Res. Ther.* 8:14. doi: 10.1186/s13195-016-0181-2
- Lopes da Silva, F. H., Hoeks, A., Smits, H., and Zetterberg, L. H. (1974). Model of brain rhythmic activity. The alpha-rhythm of the thalamus. *Kybernetik* 15, 27–37. doi: 10.1007/BF00270757
- Love, S., and Miners, J. S. (2016). Cerebrovascular disease in ageing and Alzheimer's disease. *Acta Neuropathol.* 131, 645–658. doi: 10.1007/s00401-015-1522-0
- Mahley, R. W. (2016). Apolipoprotein E: from cardiovascular disease to neurodegenerative disorders. *J. Mol. Med.* 94, 739–746. doi: 10.1007/s00109-016-1427-y
- Malek, N., Baker, M. R., Mann, C., and Greene, J. (2017). Electroencephalographic markers in dementia. *Acta Neurol. Scand.* 135, 388–393. doi: 10.1111/ane.12638
- Martinez, G., Vernooij, R. W., Fuentes Padilla, P., Zamora, J., Bonfill Cosp, X., and Flicker, L. (2017). 18F PET with florbetapir for the early diagnosis of Alzheimer's disease dementia and other dementias in people with mild cognitive impairment (MCI). *Cochr. Database Syst. Rev.* 11:CD012216. doi: 10.1002/14651858.CD012216.pub2
- McKhann, G., Drachman, D., Folstein, M., Katzman, R., Price, D., and Stadlan, E. M. (1984). Clinical diagnosis of Alzheimer's disease: report of the NINCDS-ADRDA work group under the auspices of department of health and human services task force on Alzheimer's disease. *Neurology* 34, 939–944. doi: 10.1212/WNL.34.7.939
- McLachlan, D. R. C., Bergeron, C., Alexandrov, P. N., Walsh, W. J., Pogue, A. I., Percy, M. E., et al. (2019). Aluminum in neurological and neurodegenerative disease. *Mol. Neurobiol.* 56, 1531–1538. doi: 10.1007/s12035-018-1441-x
- Merlet, I., Birot, G., Salvador, R., Molaee-Ardekani, B., Mekonnen, A., Soria-Frishi, A., et al. (2013). From oscillatory transcranial current stimulation to scalp EEG changes: a biophysical and physiological modeling study. *PLoS ONE* 8:e57330. doi: 10.1371/journal.pone.0057330
- Meyer, M. A., Caccia, A., Martinez, D., and Mingos, M. A. (2018). PET imaging of 18F-florbetapir in cognitively impaired individuals: lack of activity within the cerebellar cortex. *Neurol Int.* 10:7666. doi: 10.4081/ni.2018.7666
- Morris, E., Chalkidou, A., Hammers, A., Peacock, J., Summers, J., and Keevil, S. (2016). Diagnostic accuracy of (18)F amyloid PET tracers for the diagnosis of Alzheimer's disease: a systematic review and meta-analysis. *Eur. J. Nucl. Med. Mol. Imag.* 43, 374–385. doi: 10.1007/s00259-015-3228-x
- Moses, W. W. (2011). Fundamental limits of spatial resolution in PET. *Nucl. Instrum. Methods Phys. Res. A.* 648(Suppl. 1), S236–S240. doi: 10.1016/j.nima.2010.11.092
- Murray, M. E., Lowe, V. J., Graff-Radford, N. R., Liesinger, A. M., Cannon, A., Przybelski, S. A., et al. (2015). Clinicopathologic and (11)C-Pittsburgh compound B implications of Thal amyloid phase across the Alzheimer's disease spectrum. *Brain* 138, 1370–1381. doi: 10.1093/brain/awv050
- Nakamura, A., Cuesta, P., Fernandez, A., Arahata, Y., Iwata, K., Kuratsubo, I., et al. (2018). Electromagnetic signatures of the preclinical and prodromal stages of Alzheimer's disease. *Brain* 141, 1470–1485. doi: 10.1093/brain/aww044
- Ossenkopppele, R., Jansen, W. J., Rabinovici, G. D., Knol, D. L., van der Flier, W. M., van Berckel, B. N., et al. (2015). Prevalence of amyloid PET

- positivity in dementia syndromes: a meta-analysis. *JAMA* 313, 1939–1949. doi: 10.1001/jama.2015.4669
- Osswald, G. (2018). *BioArctic Announces Positive Topline Results of BAN2401 Phase 2b at 18 Months in Early Alzheimer's Disease*. *BioArctic Press Release*.
- Panza, F., Lozupone, M., Dibello, V., Greco, A., Daniele, A., Seripa, D., et al. (2019). Are antibodies directed against amyloid-beta (A β) oligomers the last call for the Abeta hypothesis of Alzheimer's disease? *Immunotherapy* 11, 3–6. doi: 10.2217/imt-2018-0119
- Petkoski, S., Palva, J. M., Jirsa, V. K. (2018). Phase-lags in large scale brain synchronization: methodological considerations and *in-silico* analysis. *PLoS Comput. Biol.* 14:e1006160. doi: 10.1371/journal.pcbi.1006160
- Petkoski, S., Spiegler, A., Proix, T., Aram, P., Temprado, J.-J., and Jirsa, V. K. (2016). Heterogeneity of time delays determines synchronization of coupled oscillators. *Phys. Rev.* 94:012209. doi: 10.1103/PhysRevE.94.012209
- Pink, J., O'Brien, J., Robinson, L., and Longson, D. (2018). Dementia: assessment, management and support: summary of updated NICE guidance. *BMJ*. 361:k2438. doi: 10.1136/bmj.k2438
- Prasansuklab, A., and Tencomnao, T. (2013). Amyloidosis in Alzheimer's disease: the toxicity of Amyloid Beta (A β), mechanisms of its accumulation and implications of medicinal plants for therapy. *Evid. Based Complement. Alternat. Med.* 2013:413808. doi: 10.1155/2013/413808
- Proix, T., Bartolomei, F., Guye, M., and Jirsa, V. K. (2017). Individual brain structure and modelling predict seizure propagation. *Brain* 140, 641–654. doi: 10.1093/brain/awx004
- Ren, S.-Q., Yao, W., Yan, J.-Z., Jin, C., Yin, J.-J., Yuan, J., et al. (2018). Amyloid β causes excitation/inhibition imbalance through dopamine receptor 1-dependent disruption of fast-spiking GABAergic input in anterior cingulate cortex. *Sci. Rep.* 8:302. doi: 10.1038/s41598-017-18729-5
- Reuter, M., Schmansky, N. J., Rosas, H. D., and Fischl, B. (2012). Within-subject template estimation for unbiased longitudinal image analysis. *Neuroimage* 61, 1402–1418. doi: 10.1016/j.neuroimage.2012.02.084
- Rice, D. M., Buchsbaum, M. S., Starr, A., Auslander, L., Hagman, J., and Evans, W. J. (1990). Abnormal EEG slow activity in left temporal areas in senile dementia of the Alzheimer type. *J. Gerontol.* 45, M145–M151. doi: 10.1093/geronj/45.4.M145
- Ripoli, C., Cocco, S., Li Puma, D. D., Piacentini, R., Mastrodonato, A., Scala, F., et al. (2014). Intracellular accumulation of amyloid- β (A β) protein plays a major role in A β -induced alterations of glutamatergic synaptic transmission and plasticity. *J. Neurosci.* 34, 12893–12903. doi: 10.1523/JNEUROSCI.1201-14.2014
- Ritter, P., Schirner, M., McIntosh, A. R., and Jirsa, V. K. (2013). The virtual brain integrates computational modeling and multimodal neuroimaging. *Brain Connect.* 3, 121–145. doi: 10.1089/brain.2012.0120
- Robinson, E. C., Jbabdi, S., Glasser, M. F., Andersson, J., Burgess, G. C., Harms, M. P., et al. (2014). MSM: a new flexible framework for multimodal surface matching. *Neuroimage* 100, 414–426. doi: 10.1016/j.neuroimage.2014.05.069
- Robinson, J. L., Corrada, M. M., Kovacs, G. G., Dominique, M., Caswell, C., Xie, S. X., et al. (2018a). Non-Alzheimer's contributions to dementia and cognitive resilience in The 90+ Study. *Acta Neuropathol.* 136, 377–388. doi: 10.1007/s00401-018-1872-5
- Robinson, J. L., Lee, E. B., Xie, S. X., Rennert, L., Suh, E., Bredenberg, C., et al. (2018b). Neurodegenerative disease concomitant proteinopathies are prevalent, age-related and APOE4-associated. *Brain* 141, 2181–2193. doi: 10.1093/brain/awy146
- Roche (2019). *Roche to Discontinue Phase III CREAD 1 and 2 Clinical Studies of Crenezumab in Early Alzheimer's Disease (AD)-Other Company Programmes in AD Continue 2019 [updated 04/01/2019]*. Available online at: https://www.roche.com/dam/jcr:e3181d56-8cac-4db8-a7d4-2f883ee2847c/en/20190130-MR_CREN_EN.pdf
- Sadigh-Eteghad, S., Sabermarouf, B., Majidi, A., Talebi, M., Farhoudi, M., and Mahmoudi, J. (2015). Amyloid-beta: a crucial factor in Alzheimer's disease. *Med. Principles Pract.* 24, 1–10. doi: 10.1159/000369101
- Salloway, S., Honigberg, L. A., Cho, W., Ward, M., Friesenhahn, M., Brunstein, F., et al. (2018). Amyloid positron emission tomography and cerebrospinal fluid results from a crenezumab anti-amyloid-beta antibody double-blind, placebo-controlled, randomized phase II study in mild-to-moderate Alzheimer's disease (BLAZE). *Alzheimer's Res. Ther.* 10:96. doi: 10.1186/s13195-018-0424-5
- Sanz Leon, P., Knock, S. A., Woodman, M. M., Domide, L., Mersmann, J., McIntosh, A. R., et al. (2013). The Virtual Brain: a simulator of primate brain network dynamics. *Front. Neuroinform.* 7:10. doi: 10.3389/fninf.2013.00010
- Sanz-Leon, P., Knock, S. A., Spiegler, A., and Jirsa, V. K. (2015). Mathematical framework for large-scale brain network modeling in The Virtual Brain. *Neuroimage* 111, 385–430. doi: 10.1016/j.neuroimage.2015.01.002
- Schirner, M., Rothmeier, S., Jirsa, V. K., McIntosh, A. R., and Ritter, P. (2015). An automated pipeline for constructing personalized virtual brains from multimodal neuroimaging data. *Neuroimage* 117, 343–357. doi: 10.1016/j.neuroimage.2015.03.055
- Schmolesky, M. (2005). "The primary visual cortex" in *Webvision: The Organization of the Retina and Visual System [Internet]*, eds H. Kolb, E. Fernandez, and R. Nelson (Salt Lake City, UT: University of Utah Health Sciences Center).
- Schöll, M., Lockhart Samuel, N., Schonhaut Daniel, R., O'Neil James, P., Janabi, M., Ossenkoppele, R., et al. (2016). PET imaging of Tau deposition in the aging human brain. *Neuron* 89, 971–982. doi: 10.1016/j.neuron.2016.01.028
- Schüz, A., and Braitenberg, V. (ed) (2002). "The human cortical white matter: quantitative aspects of cortico-cortical long-range connectivity," in *Cortical Areas: Unity and Diversity* (London; New York, NY: Taylor & Davis), 377f. doi: 10.4324/9780203219911_chapter_16
- Selkoe, D. J., and Hardy, J. (2016). The amyloid hypothesis of Alzheimer's disease at 25 years. *EMBO Mol. Med.* 8, 595–608. doi: 10.15252/emmm.201606210
- Smith, R. E., Tournier, J.-D., Calamante, F., and Connelly, A. (2012). Anatomically-constrained tractography: improved diffusion MRI streamlines tractography through effective use of anatomical information. *NeuroImage* 62, 1924–1938. doi: 10.1016/j.neuroimage.2012.06.005
- Smith, R. E., Tournier, J. D., Calamante, F., and Connelly, A. (2015). SIFT2: enabling dense quantitative assessment of brain white matter connectivity using streamlines tractography. *Neuroimage* 119, 338–351. doi: 10.1016/j.neuroimage.2015.06.092
- Smith, S. M., Jenkinson, M., Woolrich, M. W., Beckmann, C. F., Behrens, T. E., Johansen-Berg, H., et al. (2004). Advances in functional and structural MR image analysis and implementation as FSL. *Neuroimage* 23(Suppl. 1), S208–S219. doi: 10.1016/j.neuroimage.2004.07.051
- Song, Z., Insel, P. S., Buckley, S., Johannes, S., Mezher, A., Simonson, A., et al. (2015). Brain amyloid-beta burden is associated with disruption of intrinsic functional connectivity within the medial temporal lobe in cognitively normal elderly. *J. Neurosci.* 35, 3240–3247. doi: 10.1523/JNEUROSCI.2092-14.2015
- Sotero, R. C., and Trujillo-Barreto, N. J. (2008). Biophysical model for integrating neuronal activity, EEG, fMRI and metabolism. *NeuroImage* 39, 290–309. doi: 10.1016/j.neuroimage.2007.08.001
- Sotero, R. C., Trujillo-Barreto, N. J., Iturria-Medina, Y., Carbonell, F., and Jimenez, J. C. (2007). Realistically coupled neural mass models can generate EEG rhythms. *Neural Comput.* 19, 478–512. doi: 10.1162/neco.2007.19.2.478
- Spiegler, A. (2011). *Dynamics of Biologically Informed Neural Mass Models of the Brain*. Ilmenau: Universitätsverlag Ilmenau.
- Spiegler, A., and Jirsa, V. (2013). Systematic approximations of neural fields through networks of neural masses in the virtual brain. *NeuroImage* 83, 704–725. doi: 10.1016/j.neuroimage.2013.06.018
- Spiegler, A., Kiebel, S. J., Atay, F. M., and Knösche, T. R. (2010). Bifurcation analysis of neural mass models: impact of extrinsic inputs and dendritic time constants. *NeuroImage* 52, 1041–1058. doi: 10.1016/j.neuroimage.2009.12.081
- Spiegler, A., Knösche, T. R., Schwab, K., Hauelsen, J., and Atay, F. M. (2011). Modeling brain resonance phenomena using a neural mass model. *PLoS Comput. Biol.* 7:e1002298. doi: 10.1371/journal.pcbi.1002298
- Stefanescu, R. A., and Jirsa, V. K. (2008). A low dimensional description of globally coupled heterogeneous neural networks of excitatory and inhibitory neurons. *PLoS Comput. Biol.* 4:e1000219. doi: 10.1371/journal.pcbi.1000219
- Stefanovski, L., Ghani, A., McIntosh, A. R., Ritter, P. (2016). Linking connectomics and dynamics in the human brain. *e-Neuroforum* 7, 64–70. doi: 10.1007/s13295-016-0027-1
- Storck, S. E., and Pietrzik Claus, U. (2018). The Blood brain-barrier and its role in Alzheimer's disease. *Neuroforum* 24:A197. doi: 10.1515/nf-2018-A014
- Strogatz, S. H. (2015). *Nonlinear Dynamics and Chaos: With Applications to Physics, Biology, Chemistry, and Engineering: Second Edition*. Boulder, CO: Westview Press, a member of the Perseus Books Group.

- Tadel, F., Baillet, S., Mosher, J. C., Pantazis, D., and Leahy, R. M. (2011). Brainstorm: a user-friendly application for MEG/EEG analysis. *Comput. Intell. Neurosci.* 2011:13. doi: 10.1155/2011/879716
- Takatori, S., Wang, W., Iguchi, A., and Tomita, T. (2019). Genetic risk factors for alzheimer disease: emerging roles of microglia in disease pathomechanisms. *Adv. Exp. Med. Biol.* 1118, 83–116. doi: 10.1007/978-3-030-05542-4_5
- Tapia-Rojas, C., Cabezas-Opazo, F., Deaton, C. A., Vergara, E. H., Johnson, G. V. W., and Quintanilla, R. A. (2019). It's all about tau. *Prog. Neurobiol.* 175, 54–76. doi: 10.1016/j.pneurobio.2018.12.005
- Thal, D. R., Rub, U., Orantes, M., and Braak, H. (2002). Phases of a beta-deposition in the human brain and its relevance for the development of AD. *Neurology* 58, 1791–1800. doi: 10.1212/WNL.58.12.1791
- Thomas, B. A., Cuplov, V., Bousse, A., Mendes, A., Thielemans, K., Hutton, B. F., et al. (2016). PETPVC: a toolbox for performing partial volume correction techniques in positron emission tomography. *Phys. Med. Biol.* 61, 7975–7993. doi: 10.1088/0031-9155/61/22/7975
- Tournier, J. D., Calamante, F., and Connelly, A. (2007). Robust determination of the fibre orientation distribution in diffusion MRI: non-negativity constrained super-resolved spherical deconvolution. *Neuroimage* 35, 1459–1472. doi: 10.1016/j.neuroimage.2007.02.016
- Tournier, J. D., Calamante, F., and Connelly, A. (2010). Improved probabilistic streamlines tractography by 2nd order integration over fibre orientation distributions. *Proc. Intl. Soc. Mag. Reson. Med.* 18:1670.
- Tournier, J. D., Calamante, F., and Connelly, A. (2013). Determination of the appropriate b value and number of gradient directions for high-angular-resolution diffusion-weighted imaging. *NMR Biomed.* 26, 1775–1786. doi: 10.1002/nbm.3017
- Ulrich, D. (2015). Amyloid-beta impairs synaptic inhibition via GABA(A) receptor endocytosis. *J. Neurosci.* 35, 9205–9210. doi: 10.1523/JNEUROSCI.0950-15.2015
- Veraart, J., Novikov, D. S., Christiaens, D., Ades-aron, B., Sijbers, J., and Fieremans, E. (2016). Denoising of diffusion MRI using random matrix theory. *NeuroImage* 142, 394–406. doi: 10.1016/j.neuroimage.2016.08.016
- Verret, L., Mann Edward, O., Hang Giao, B., Barth Albert, M. I., Cobos, I., Ho, K., et al. (2012). Inhibitory interneuron deficit links altered network activity and cognitive dysfunction in Alzheimer model. *Cell* 149, 708–721. doi: 10.1016/j.cell.2012.02.046
- Villemagne, V. L., Ataka, S., Mizuno, T., Brooks, W. S., Wada, Y., Kondo, M., et al. (2009). High striatal amyloid beta-peptide deposition across different autosomal Alzheimer disease mutation types. *Arch. Neurol.* 66, 1537–1544. doi: 10.1001/archneurol.2009.285
- Walsh, D. M., and Selkoe, D. J. (2007). A beta oligomers - a decade of discovery. *J. Neurochem.* 101, 1172–1184. doi: 10.1111/j.1471-4159.2006.04426.x
- Wang, S., and Colonna, M. (2019). Microglia in Alzheimer's disease: a target for immunotherapy. *J. Leukoc. Biol.* 106, 219–227. doi: 10.1002/jlb.mr0818-319r
- Wendling, F., Bartolomei, F., Bellanger, J. J., and Chauvel, P. (2002). Epileptic fast activity can be explained by a model of impaired GABAergic dendritic inhibition. *Eur. J. Neurosci.* 15, 1499–1508. doi: 10.1046/j.1460-9568.2002.01985.x
- Wendling, F., Bellanger, J. J., Bartolomei, F., and Chauvel, P. (2000). Relevance of nonlinear lumped-parameter models in the analysis of depth-EEG epileptic signals. *Biol. Cybernet.* 83, 367–378. doi: 10.1007/s004220000160
- WHO (2011). *Global Health and Ageing*. Aging UNIO, WHO.
- Wilson, H. R., and Cowan, J. D. (1972). Excitatory and inhibitory interactions in localized populations of model neurons. *Biophys. J.* 12, 1–24. doi: 10.1016/S0006-3495(72)86068-5
- Wimo, A., Guerchet, M., Ali, G. C., Wu, Y. T., Prina, A. M., Winblad, B., et al. (2017). The worldwide costs of dementia 2015 and comparisons with 2010. *Alzheimers Dement.* 13, 1–7. doi: 10.1016/j.jalz.2016.07.150
- Wimo, A., Jonsson, L., Gustavsson, A., McDaid, D., Ersek, K., Georges, J., et al. (2011). The economic impact of dementia in Europe in 2008-cost estimates from the Eurocode project. *Int. J. Geriatr. Psychiatry* 26, 825–832. doi: 10.1002/gps.2610
- Wong, K.-F., and Wang, X.-J. (2006). A recurrent network mechanism of time integration in perceptual decisions. *J. Neurosci.* 26, 1314–1328. doi: 10.1523/JNEUROSCI.3733-05.2006
- Woolrich, M. W., Jbabdi, S., Patenaude, B., Chappell, M., Makni, S., Behrens, T., et al. (2009). Bayesian analysis of neuroimaging data in FSL. *Neuroimage* 45(1 Suppl.), S173–S186. doi: 10.1016/j.neuroimage.2008.10.055
- Wright, J. J., and Liley, D. T. J. (2010). Dynamics of the brain at global and microscopic scales: neural networks and the EEG. *Behav. Brain Sci.* 19, 285–295. doi: 10.1017/S0140525X00042679
- Xu, J., Wang, J., Wimo, A., Fratiglioni, L., and Qiu, C. (2017). The economic burden of dementia in China, 1990–2030: implications for health policy. *Bull. World Health Organ.* 95, 18–26. doi: 10.2471/BLT.15.167726
- Zetterberg, L. H., Kristiansson, L., and Mossberg, K. (1978). Performance of a model for a local neuron population. *Biol. Cybernet.* 31, 15–26. doi: 10.1007/BF00337367
- Zhou, J., Yu, W., Zhang, M., Tian, X., Li, Y., and Lu, Y. (2019). Imbalance of microglial TLR4/TREM2 in LPS-treated APP/PS1 transgenic mice: a potential link between Alzheimer's disease and systemic inflammation. *Neurochem. Res.* 44, 1138–1151. doi: 10.1007/s11064-019-02748-x
- Zimmermann, J., Perry, A., Breakspear, M., Schirner, M., Sachdev, P., Wen, W., et al. (2018). Differentiation of Alzheimer's disease based on local and global parameters in personalized Virtual Brain models. *NeuroImage Clin.* 19, 240–251. doi: 10.1016/j.nicl.2018.04.017

Conflict of Interest Statement: The authors declare that the research was conducted in the absence of any commercial or financial relationships that could be construed as a potential conflict of interest.

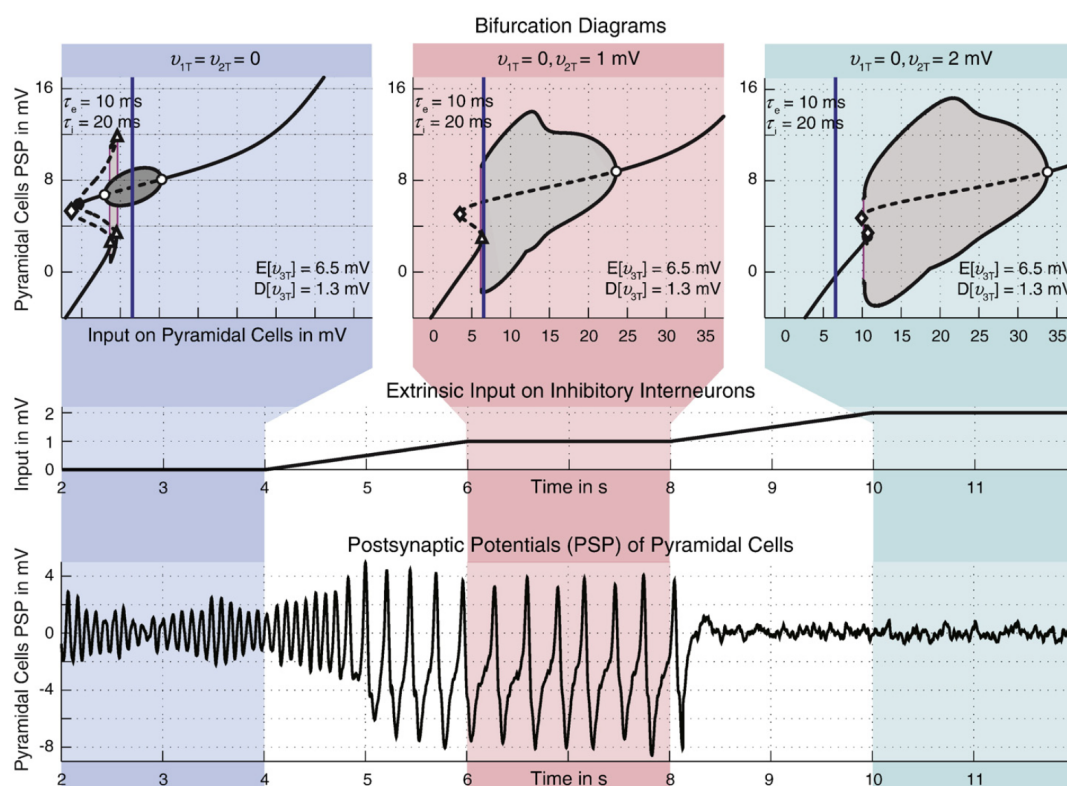
Copyright © 2019 Stefanovski, Triebkorn, Spiegler, Diaz-Cortes, Solodkin, Jirsa, McIntosh and Ritter. This is an open-access article distributed under the terms of the Creative Commons Attribution License (CC BY). The use, distribution or reproduction in other forums is permitted, provided the original author(s) and the copyright owner(s) are credited and that the original publication in this journal is cited, in accordance with accepted academic practice. No use, distribution or reproduction is permitted which does not comply with these terms.

SUPPLEMENTARY MATERIAL DER ORIGINALPUBLIKATION

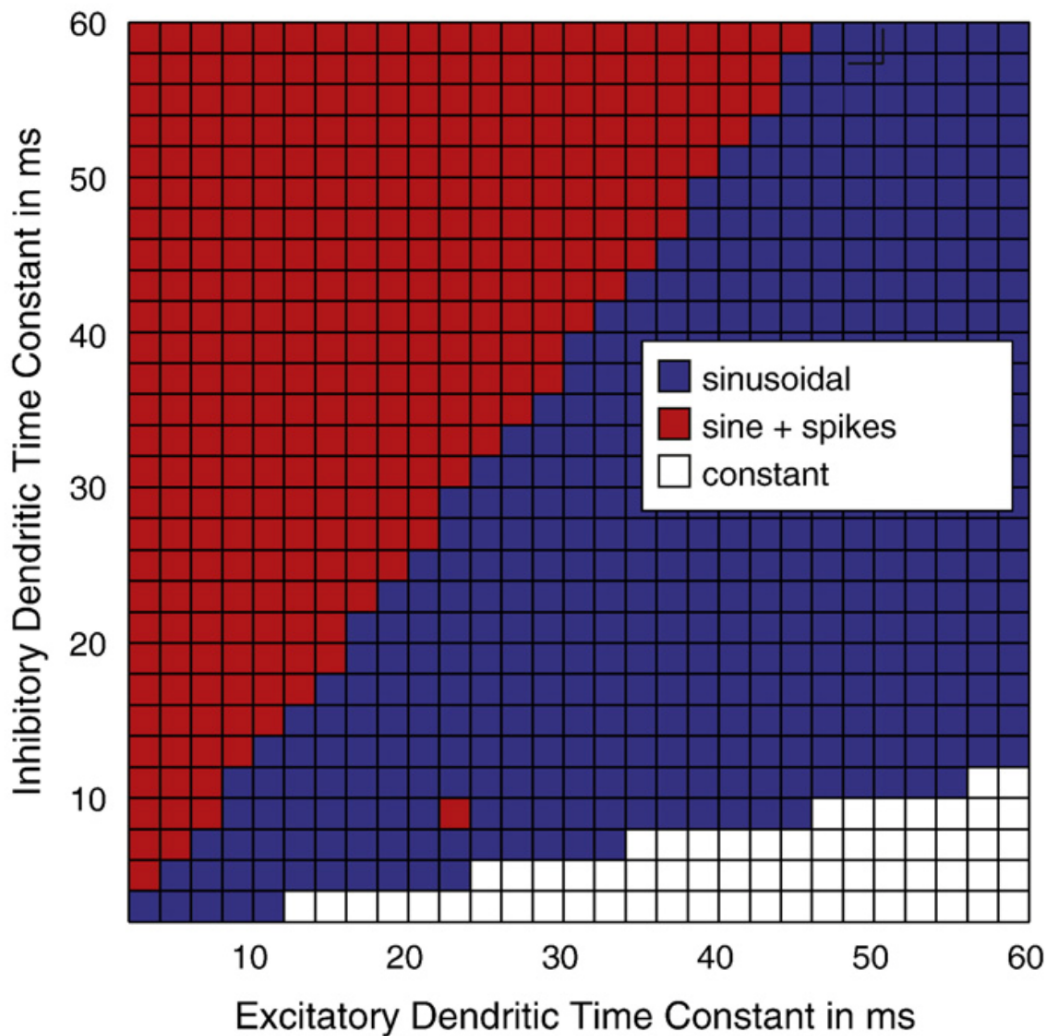
Stefanovski, L., P. Triebkorn, A. Spiegler, M.-A. Diaz-Cortes, A. Solodkin, V. Jirsa, A.R. McIntosh and P. Ritter for the Alzheimer's Disease Neuroimaging Initiative, *Linking Molecular Pathways and Large-Scale Computational Modeling to Assess Candidate Disease Mechanisms and Pharmacodynamics in Alzheimer's Disease*. Frontiers in Computational Neuroscience, 2019. **13**(54).

<https://doi.org/10.3389/fncom.2019.00054>

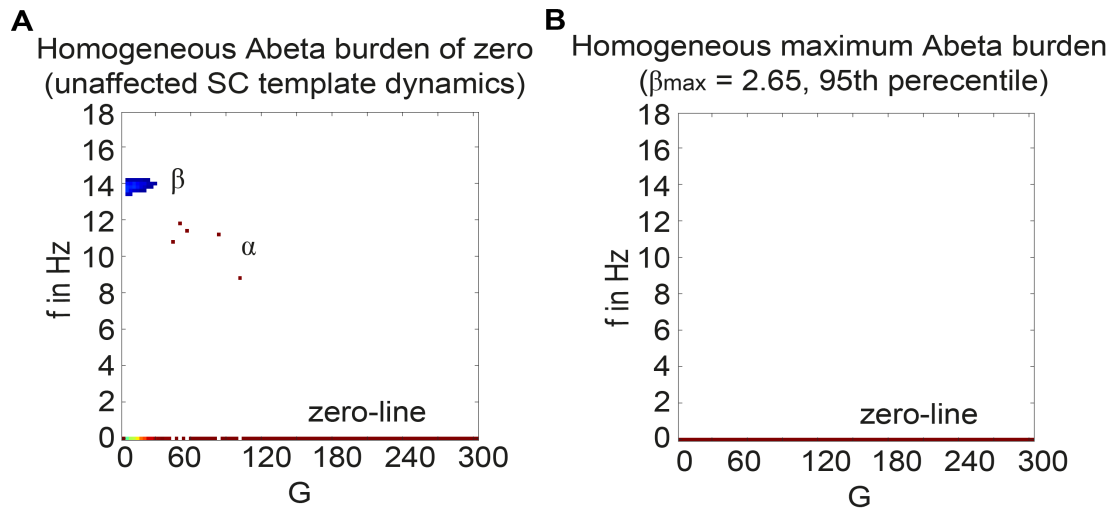
**SUPPLEMENTARY MATERIAL.
FIGURES.**



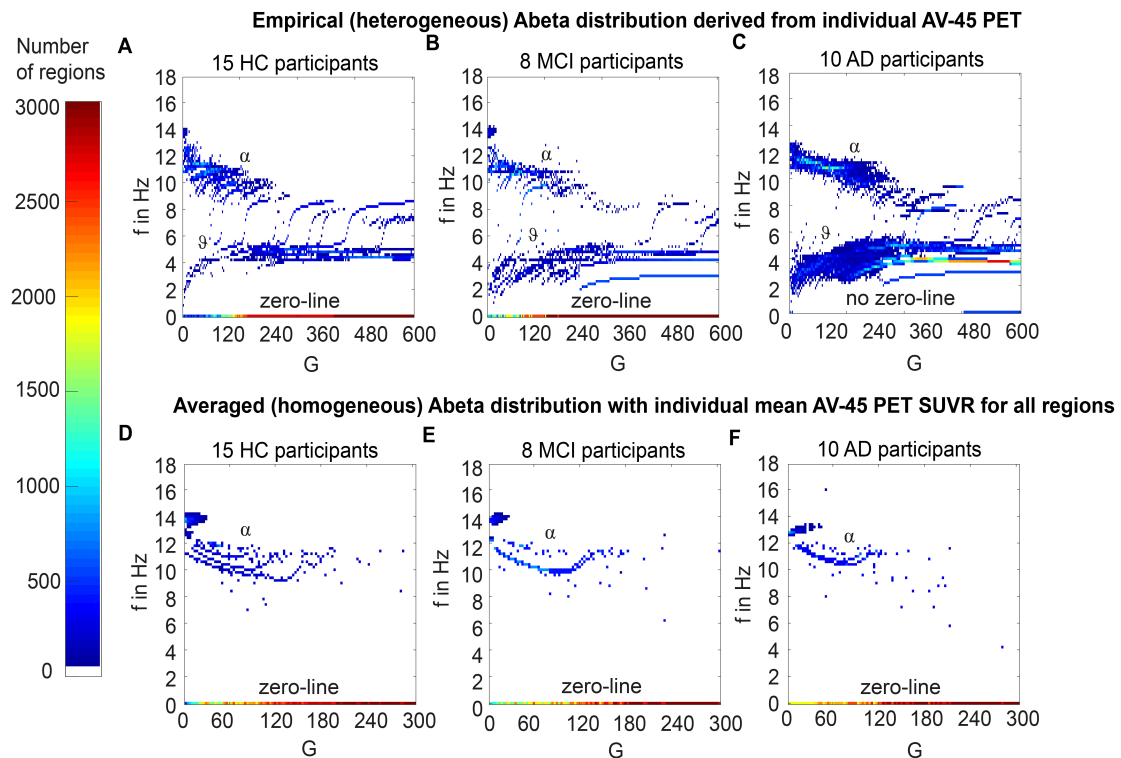
Supplementary Figure 1. Input on pyramidal cells in Jansen-Rit model leads to fundamental changes (criticalities) in the behavior of the system. Taken from Spiegel et al., figure 13 of (1) with permission. Input on inhibitory cells is changed with time (middle row). Shown are three different states of the model: amplitude-modulated alpha activity (highlighted in blue), slower spiking activity (red) and noise in the absence of intrinsic oscillations (green). In the top row, the corresponding bifurcation diagrams are shown for different input values on inhibitory cells. The diagrams show the bifurcations between input on pyramidal cells (x) and the PSP of pyramidal cells (y). Criticalities lead to fundamental changes of the temporal behavior of PSP for only slightly different inputs. In this case, the criticalities of the non-linear system are bifurcations in its mathematical meaning (2). Different types of bifurcations can be seen: sub-critical (black) and supercritical (white) Andronov–Hopf bifurcations, saddle–saddle bifurcations (diamonds) and saddle-node bifurcations (triangles), global bifurcations (red lines). For a more detailed description and for the context of this figure in the corresponding study, please consider the original publication (1).



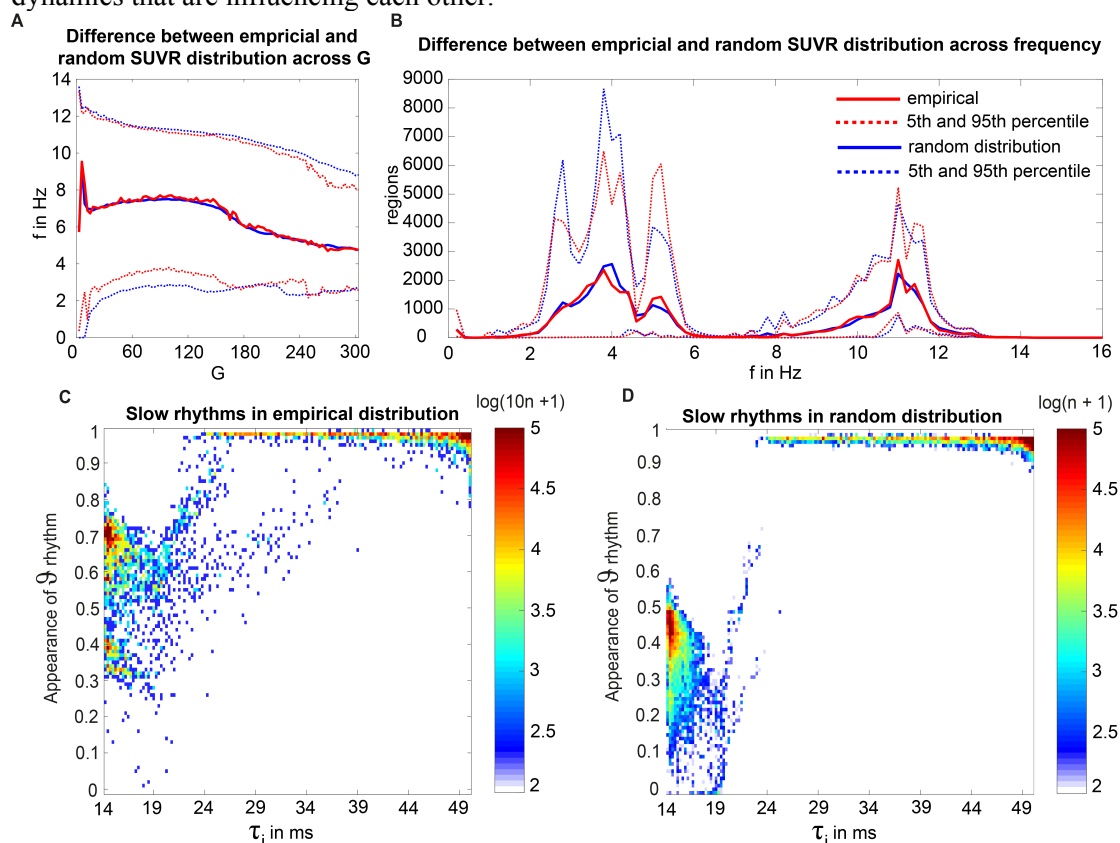
Supplementary Figure 2. Ratio of excitatory and inhibitory time constants modulates frequency in Jansen-Rit model Taken from Spiegler et al., figure 7 of (1) with permission. Blue regions in the parameter space show fast sinusoidal oscillations in alpha rhythm. In red areas, also slower spikes in theta rhythm get possible. For a more detailed description and for the context of this figure in the corresponding study, please consider the original publication (1).



Supplementary Figure 3. Control simulations for the standardized SC template with extreme values of Abeta burden. Because the only individual feature in this study is the Abeta distribution, all participants show the same behaviour for an equal and homogeneous Abeta distribution. Density of regions with a specific dominating frequency at each G. Shown are the sums of all participants regions. **(A)** Homogeneous distribution with Abeta burden of zero at each region, therefore representing the unaffected dynamics that are only driven by the underlying averaged healthy SC template. There is a small beta cluster and single G values between 50 and 100 with alpha rhythms, but the behaviour is dominated by the zero-line. See also **Figure 6A**. **(B)** Homogeneous distribution with Abeta burden of $\beta_{\max} = 2.65$ at each region. Maximum Abeta was calculated by the 95th percentile of all regions in all participants. It is also represented in the sigmoid curve in **Figure 3**. The full G spectrum is characterized by the zero-line. See also **Figure 6I**.

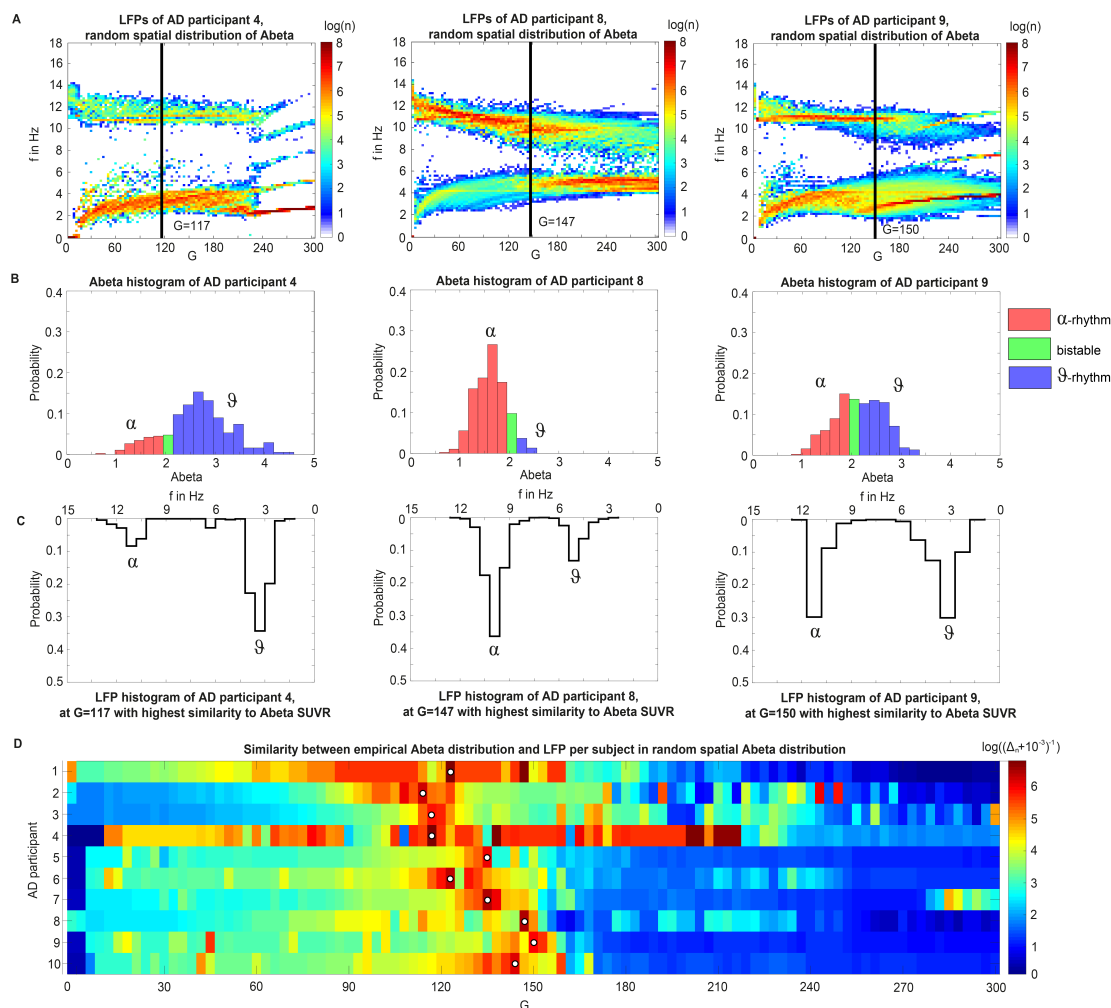


Supplementary Figure 4. AD-specific slowing in neural frequencies and influence of the heterogeneous spatial pattern of Abeta distribution to the spectral behavior. (A, B, C) - Overview of the different frequency behaviors dependent on global coupling factor G , summarized for the three groups HC, MCI, AD. The plots show the density of regions with a specific dominating frequency at each G . Shown are the sums of all participants' regions for (A) HC ($n=15$), (B) MCI ($n=8$) and (C) AD ($n=10$). Notably some regions reside at a frequency of 0 beginning at low G values for HC and MCI. This behavior is not apparent for AD, there is only a blue line (meaning low density) at zero at a high G (C) – because only 1 out of the 10 AD participants showed a zero-line behavior. (D, E, F): corresponding plots for simulations with homogeneous distribution of averaged Abeta load for each subject, so without spatial information about Abeta distribution and without Abeta heterogeneity. The mean AV-45 PET SUVR for each participant was applied to every region of the brain. The phenomena found in panels (A-C) do not appear in (D) HC, (E) MCI and (F) AD. Namely all show a similar synchronized alpha rhythm at low G and convert early to the zero-line behaviour. This strongly supports the hypothesis that not the general burden of Abeta is the driving factor for the observed phenomena in this study. It seems to be more the spatial heterogeneity in the brain, meaning that in the brain coexist areas with different local dynamics that are influencing each other.



Supplementary Figure 5. Results for random spatial distribution of Abeta PET SUVRs of AD participants. (A) Mean dominating frequencies (y) along global coupling (x), averaged across regions and subjects. Color legend shown in (B). There is no relevant difference except the smoother contour of the blue line because of 10-times more simulations. (B) Spectrogram-like plot with amount of regions (y) per frequency (x). Again the random distribution and the empirical distribution do not differ. (C, D) Dependency between Abeta-PET-derived time constant (x) and the probability of dominant theta rhythm (y) across all simulations. (C) empirical distribution, (D) random distribution. Again we can observe the

models criticalities at about 18ms and 24ms, where the theta probability increases and alpha rhythms disappear. Moreover, we can see a shift of the sweet spot for low time constants by the ‘shuffling’: meanwhile for $\tau_i=14$ ms in the empirical distribution theta appears in 70% of the simulations, in the corresponding simulations with random spatial distribution it appears only in 45% of the simulations. This means that the AD-specific spatial pattern leads to specific slowing for regions with very low Abeta in comparison to the random distribution.



Supplementary Figure 6. Number of regions in different regimes determine overall spectral properties of simulated EEG. Surrogate Abeta PET SUVR distributions reveals the role of region burden for the emergence different dynamical regimes. (A) shows for three exemplary AD participants (4, 8 and 9) the dominating frequencies (γ) of each region depending on global coupling factor G (x axis). Shown is the sum of 10 random spatial distributions of the empirical Abeta. The corresponding histograms with the normalized amount of regions with various Abeta can be seen in (B): classified by their inhibitory time constant to the alpha, theta or bistable regime (Figure 6). Below in (C) is the frequency distribution shown for a specific value of G , where the ratio of theta rhythm corresponds best to the ratio of regions in theta regime, indicated by a black line in (A). This similarity is demonstrated in (D): the optimal range (white dot) is very similar for all 10 AD subjects at $100 < G < 150$. Similarity is quantified here as the logarithm of the reciprocal of absolute difference between the ratios of theta to alpha and theta together, meaning that high values show high similarity. Note that subject 4 has three additional optima beside the presented one at $G = 117$: 138, 201, and 204. Beside this optimal correspondence of frequencies and Abeta

SUVRs, we can see a dependency across large parts of the G spectrum: for participant 4, the high amount of theta regime regions lead to a dominant theta cluster in the full G spectrum and synchronizes to a theta/delta rhythm for higher Gs, independent of the spatial distributions. Vice versa, participant 8 has a high amount of alpha regime regions and shows therefore a dominant alpha cluster until G=150 – afterwards the bistable and theta regions reach the theta limit cycle (see **Figure 6**) and propagate slower rhythms. Participant 9 has an equal distribution of alpha and theta regime regions and many bistable regions, which leads to alpha and theta clusters of the same intensity until G=150, while again afterwards the slower rhythms are dominating. The reason for the dominance of slower rhythms for higher G values can also be found in the bifurcation diagrams of **Figure 6**: while in theta regime (**Figure 6I**) for lower Gs the system is in a stable focus and for higher Gs get to the theta limit cycle, the alpha regime (**Figure 6A**) vice versa starts in alpha limit cycle and ends for higher Gs in a stable focus. Since in the absence of noise the system produces no oscillations in stable focuses, for higher Gs the alpha regions with no intrinsic oscillations can easily be synchronized to the propagated theta signal of neighbored regions. All this indicates that TVB weights the distribution of Abeta and transforms it to a complex slowing phenomenon.

TABLES.

Supplementary Table 1. MPRAGE metadata.

ID	Model	TE [ms]	TR [s]	MatrixSize	VoxelSize [mm]
023_S_1190	TrioTim	2.98	2.3	(176, 240, 256)	(1.0, 1.0, 1.0)
002_S_1280	Prisma_fit	2.95	2.3	(176, 240, 256)	(1.2000046, 1.0546875, 1.0546875)
011_S_4547	Prisma_fit	2.98	2.3	(208, 240, 256)	(1.0, 1.0, 1.0)
168_S_6142	Prisma_fit	2.98	2.3	(208, 240, 256)	(0.9999948, 1.0, 1.0)
002_S_6103	Prisma_fit	2.98	2.3	(208, 240, 256)	(1.0, 1.0, 1.0)
002_S_4654	Prisma_fit	2.95	2.3	(176, 240, 256)	(1.199997, 1.0546875, 1.0546875)
022_S_5004	TrioTim	2.98	2.3	(176, 240, 256)	(1.0, 1.0, 1.0)
003_S_6067	Prisma	2.98	2.3	(208, 240, 256)	(1.0, 1.0, 1.0)
002_S_4229	Prisma_fit	2.98	2.3	(208, 240, 256)	(1.0, 1.0, 1.0)
012_S_6073	Prisma	2.98	2.3	(208, 240, 256)	(1.0, 1.0, 1.0)
002_S_1261	Prisma_fit	2.95	2.3	(176, 240, 256)	(1.2000046, 1.0546875, 1.0546875)
002_S_6009	Prisma_fit	2.95	2.3	(176, 240, 256)	(1.2000046, 1.0546875, 1.0546875)
007_S_4488	Prisma	2.98	2.3	(208, 240, 256)	(1.0, 1.0, 1.0)
003_S_4288	Prisma	2.98	2.3	(208, 240, 256)	(1.0, 1.0, 1.0)
002_S_4213	Prisma_fit	2.98	2.3	(208, 240, 256)	(1.0, 1.0, 1.0)
114_S_6039	Verio	2.98	2.3	(176, 240, 256)	(1.0, 1.0, 1.0)
036_S_4430	Skyra	2.95	2.3	(176, 240, 256)	(1.199997, 1.0546875, 1.0546875)
041_S_4974	Prisma_fit	2.95	2.3	(176, 240, 256)	(1.2000046, 1.0546875, 1.0546875)
007_S_4272	Prisma	2.98	2.3	(208, 240, 256)	(1.0, 1.0, 1.0)
011_S_4827	Prisma_fit	2.98	2.3	(208, 240, 256)	(1.0, 1.0, 1.0)

002_S_6053	Prisma_fit	2.98	2.3	(208, 240, 256)	(1.0, 1.0, 1.0)
003_S_4644	Prisma	2.98	2.3	(208, 240, 256)	(1.0, 1.0, 1.0)
002_S_4799	Prisma_fit	2.95	2.3	(176, 240, 256)	(1.2000046, 1.0546875, 1.0546875)
002_S_0413	Prisma_fit	2.95	2.3	(176, 240, 256)	(1.2000046, 1.0546875, 1.0546875)
114_S_0416	Verio	2.98	2.3	(176, 240, 256)	(1.0, 1.0, 1.0)
002_S_5178	Prisma_fit	2.95	2.3	(176, 240, 256)	(1.199997, 1.0546875, 1.0546875)
002_S_6030	Prisma_fit	2.95	2.3	(176, 240, 256)	(1.2000046, 1.0546875, 1.0546875)
003_S_1122	Prisma	2.98	2.3	(208, 240, 256)	(1.0000056, 1.0, 1.0)
011_S_4893	Prisma_fit	2.98	2.3	(208, 240, 256)	(1.0, 1.0, 1.0)
002_S_1155	Prisma_fit	2.95	2.3	(176, 240, 256)	(1.2000046, 1.0546875, 1.0546875)
036_S_4715	Skyra	2.95	2.3	(176, 240, 256)	(1.2000046, 1.0546875, 1.0546875)
007_S_4387	Prisma	2.98	2.3	(208, 240, 256)	(1.0, 1.0, 1.0)
007_S_4620	Prisma	2.98	2.3	(208, 240, 256)	(1.0, 1.0, 1.0)

Supplementary Table 2. FLAIR metadata.

ID	Model	TE [ms]	TR [s]	MatrixSize	VoxelSize [mm]
023_S_1190	TrioTim	443	4.8	(160, 256, 256)	(1.2000046, 1.0, 1.0)
002_S_1280	Prisma_fit	441	4.8	(160, 256, 256)	(1.2000046, 1.0, 1.0)
011_S_4547	Prisma_fit	441	4.8	(160, 256, 256)	(1.2000046, 1.0, 1.0)
168_S_6142	Prisma_fit	441	4.8	(160, 256, 256)	(1.2000002, 1.0, 1.0)
002_S_6103	Prisma_fit	441	4.8	(160, 256, 256)	(1.199997, 1.0, 1.0)
002_S_4654	Prisma_fit	441	4.8	(160, 256, 256)	(1.199997, 1.0, 1.0)
022_S_5004	TrioTim	439	4.8	(160, 256, 256)	(1.199997, 1.0, 1.0)
003_S_6067	Prisma	441	4.8	(160, 256, 256)	(1.2000046, 1.0, 1.0)
002_S_4229	Prisma_fit	441	4.8	(160, 256, 256)	(1.199997, 1.0, 1.0)
012_S_6073	Prisma	441	4.8	(160, 256, 256)	(1.2000046, 1.0, 1.0)
002_S_1261	Prisma_fit	441	4.8	(160, 256, 256)	(1.2000046, 1.0, 1.0)
002_S_6009	Prisma_fit	441	4.8	(160, 256, 256)	(1.2000046, 1.0, 1.0)
007_S_4488	Prisma	441	4.8	(160, 256, 256)	(1.2000046, 1.0, 1.0)
003_S_4288	Prisma	441	4.8	(160, 256, 256)	(1.199997, 1.0, 1.0)
002_S_4213	Prisma_fit	441	4.8	(160, 256, 256)	(1.199997, 1.0, 1.0)
114_S_6039	Verio	343	4.8	(160, 256, 256)	(1.0, 1.0, 1.0)
036_S_4430	Skyra	441	4.8	(160, 256, 256)	(1.2000046, 1.0, 1.0)
041_S_4974	Prisma_fit	441	4.8	(160, 256, 256)	(1.199997, 1.0, 1.0)
007_S_4272	Prisma	441	4.8	(160, 256, 256)	(1.199997, 1.0, 1.0)
011_S_4827	Prisma_fit	441	4.8	(160, 256, 256)	(1.199997, 1.0, 1.0)

002_S_6053	Prisma_fit	441	4.8	(160, 256, 256)	(1.199997, 1.0, 1.0)
003_S_4644	Prisma	441	4.8	(160, 256, 256)	(1.199997, 1.0, 1.0)
002_S_4799	Prisma_fit	441	4.8	(160, 256, 256)	(1.2000046, 1.0, 1.0)
002_S_0413	Prisma_fit	441	4.8	(160, 256, 256)	(1.2000046, 1.0, 1.0)
114_S_0416	Verio	343	4.8	(160, 256, 256)	(1.0, 1.0, 1.0)
002_S_5178	Prisma_fit	441	4.8	(160, 256, 256)	(1.199997, 1.0, 1.0)
002_S_6030	Prisma_fit	441	4.8	(160, 256, 256)	(1.2000046, 1.0, 1.0)
003_S_1122	Prisma	441	4.8	(160, 256, 256)	(1.2000005, 1.0, 1.0)
011_S_4893	Prisma_fit	441	4.8	(160, 256, 256)	(1.2000046, 1.0, 1.0)
002_S_1155	Prisma_fit	441	4.8	(160, 256, 256)	(1.2000046, 1.0, 1.0)
036_S_4715	Skyra	441	4.8	(160, 256, 256)	(1.2000046, 1.0, 1.0)
007_S_4387	Prisma	441	4.8	(160, 256, 256)	(1.2000046, 1.0, 1.0)
007_S_4620	Prisma	441	4.8	(160, 256, 256)	(1.2000046, 1.0, 1.0)

Supplementary Table 3. DTI metadata (only for HC participants to average the SC template)

ID	Model	Institute	TE [ms]	TR [s]	MatrixSize	VoxelSize [mm, mm, mm, s]	n_Bvecs	Bvals
002_S_1280	Prisma_fit	OHSU_AIRC	56	7.2	(116, 116, 80, 55)	(2.0, 2.0, 2.0, 7.2)	49	[0. 1000.]
002_S_6103	Prisma_fit	OHSU_AIRC	56	7.2	(116, 116, 80, 55)	(2.0, 2.0, 2.0, 7.2)	49	[0. 1000.]
003_S_6067	Prisma	USCINI	56	7.2	(116, 116, 80, 55)	(2.0, 2.0, 2.0, 7.2)	49	[0. 1000.]
002_S_6009	Prisma_fit	OHSU_AIRC	56	7.2	(116, 116, 80, 55)	(2.0, 2.0, 2.0, 7.2)	49	[0. 1000.]
007_S_4488	Prisma	MAYO_CLINIC_MRI_58	71	3.4	(116, 116, 81, 127)	(2.0, 2.0, 2.0, 3.4)	115	[0. 500. 1000. 2000.]
003_S_4288	Prisma	USC_Stevens_Hall_Institut e	56	7.2	(116, 116, 80, 55)	(2.0, 2.0, 2.0, 7.2)	49	[0. 1000.]
002_S_4213	Prisma_fit	OHSU_AIRC	56	7.2	(116, 116, 80, 55)	(2.5172415, 2.5172415, 2.0, 7.2)	49	[0. 1000.]
002_S_6053	Prisma_fit	OHSU_AIRC	56	7.2	(116, 116, 80, 55)	(2.0, 2.0, 2.0, 7.2)	49	[0. 1000.]
003_S_4644	Prisma	USCINI	56	7.2	(116, 116, 80, 55)	(2.0, 2.0, 2.0, 7.2)	49	[0. 1000.]
002_S_4799	Prisma_fit	OHSU_AIRC	56	7.2	(116, 116, 80, 55)	(2.0, 2.0, 2.0, 7.2)	49	[0. 1000.]
002_S_0413	Prisma_fit	OHSU_AIRC	56	7.2	(116, 116, 80, 55)	(2.0, 2.0, 2.0, 7.2)	49	[0. 1000.]
002_S_5178	Prisma_fit	OHSU_AIRC	56	7.2	(116, 116, 80, 55)	(2.0, 2.0, 2.0, 7.2)	49	[0. 1000.]
002_S_6030	Prisma_fit	OHSU_AIRC	56	7.2	(116, 116, 80, 55)	(2.0, 2.0, 2.0, 7.2)	49	[0. 1000.]
007_S_4387	Prisma	MAYO_CLINIC_MRI_58	71	3.4	(116, 116, 81, 127)	(2.0, 2.0, 2.0, 3.4)	115	[0. 500. 1000. 2000.]
007_S_4620	Prisma	MAYO_CLINIC_MRI_58	71	3.4	(116, 116, 81, 127)	(2.0, 2.0, 2.0, 3.4)	115	[0. 500. 1000. 2000.]

Supplementary Table 4. AV-45 PET (Abeta) metadata.

ID	Scanner	Model	MatrixSize	VoxelSize [mm]
----	---------	-------	------------	----------------

023_S_1190	Siemens	Biograph6_TruePoint	(160, 160, 96)	(1.5, 1.5, 1.5)
002_S_1280	Philips	GEMINI_TF_TOF_16	(160, 160, 96)	(1.5, 1.5, 1.5)
011_S_4547	Siemens	Biograph40_TruePoint	(160, 160, 96)	(1.5, 1.5, 1.5)
168_S_6142	GE	Discovery_STE	(160, 160, 96)	(1.5, 1.5, 1.5)
002_S_6103	Philips	GEMINI_TF_TOF_16	(160, 160, 96)	(1.5, 1.5, 1.5)
002_S_4654	Philips	GEMINI_TF_TOF_16	(160, 160, 96)	(1.5, 1.5, 1.5)
022_S_5004	Philips	Ingenuity_TF_PET_CT	(160, 160, 96)	(1.5, 1.5, 1.5)
003_S_6067	Siemens	Biograph64_TruePoint	(160, 160, 96)	(1.5, 1.5, 1.5)
002_S_4229	Philips	GEMINI_TF_TOF_16	(160, 160, 96)	(1.5, 1.5, 1.5)
012_S_6073	GE	Discovery_710	(160, 160, 96)	(1.5, 1.5, 1.5)
002_S_1261	Philips	GEMINI_TF_TOF_16	(160, 160, 96)	(1.5, 1.5, 1.5)
002_S_6009	Philips	GEMINI_TF_TOF_16	(160, 160, 96)	(1.5, 1.5, 1.5)
007_S_4488	GE	Discovery_690	(160, 160, 96)	(1.5, 1.5, 1.5)
003_S_4288	Siemens	Biograph64_TruePoint	(160, 160, 96)	(1.5, 1.5, 1.5)
002_S_4213	Philips	GEMINI_TF_TOF_16	(160, 160, 96)	(1.5, 1.5, 1.5)
114_S_6039	Philips	GEMINI_TF_TOF_64	(160, 160, 96)	(1.5, 1.5, 1.5)
036_S_4430	Siemens	Biograph40_TruePoint	(160, 160, 96)	(1.5, 1.5, 1.5)
041_S_4974	Siemens	HR+	(160, 160, 96)	(1.5, 1.5, 1.5)
007_S_4272	GE	Discovery_690	(160, 160, 96)	(1.5, 1.5, 1.5)
011_S_4827	Siemens	Biograph40_TruePoint	(160, 160, 96)	(1.5, 1.5, 1.5)
002_S_6053	Philips	GEMINI_TF_TOF_16	(160, 160, 96)	(1.5, 1.5, 1.5)
003_S_4644	Siemens	Biograph64_TruePoint	(160, 160, 96)	(1.5, 1.5, 1.5)
002_S_4799	Philips	GEMINI_TF_TOF_16	(160, 160, 96)	(1.5, 1.5, 1.5)
002_S_0413	Philips	GEMINI_TF_TOF_16	(160, 160, 96)	(1.5, 1.5, 1.5)
114_S_0416	Philips	GEMINI_TF_TOF_64	(160, 160, 96)	(1.5, 1.5, 1.5)
002_S_5178	Philips	GEMINI_TF_TOF_16	(160, 160, 96)	(1.5, 1.5, 1.5)
002_S_6030	Philips	GEMINI_TF_TOF_16	(160, 160, 96)	(1.5, 1.5, 1.5)
003_S_1122	Siemens	Biograph64_TruePoint	(160, 160, 96)	(1.5, 1.5, 1.5)
011_S_4893	Siemens	Biograph40_TruePoint	(160, 160, 96)	(1.5, 1.5, 1.5)
002_S_1155	Philips	GEMINI_TF_TOF_16	(160, 160, 96)	(1.5, 1.5, 1.5)
036_S_4715	Siemens	Biograph40_TruePoint	(160, 160, 96)	(1.5, 1.5, 1.5)
007_S_4387	GE	Discovery_690	(160, 160, 96)	(1.5, 1.5, 1.5)
007_S_4620	GE	Discovery_690	(160, 160, 96)	(1.5, 1.5, 1.5)

Supplementary Table 5. AV-14-51 PET (Tau) metadata

ID	Scanner	Model	MatrixSize	VoxelSize [mm]
023_S_1190	Siemens	Biograph6_TruePoint	(160, 160, 96)	(1.5, 1.5, 1.5)
002_S_1280	Philips	GEMINI_TF_TOF_16	(160, 160, 96)	(1.5, 1.5, 1.5)
011_S_4547	Siemens	Biograph40_TruePoint	(160, 160, 96)	(1.5, 1.5, 1.5)
168_S_6142	GE	Discovery_STE	(160, 160, 96)	(1.5, 1.5, 1.5)
002_S_6103	Philips	GEMINI_TF_TOF_16	(160, 160, 96)	(1.5, 1.5, 1.5)
002_S_4654	Philips	GEMINI_TF_TOF_16	(160, 160, 96)	(1.5, 1.5, 1.5)
022_S_5004	Philips	Ingenuity_TF_PET_CT	(160, 160, 96)	(1.5, 1.5, 1.5)
003_S_6067	Siemens	Biograph64_TruePoint	(160, 160, 96)	(1.5, 1.5, 1.5)
002_S_4229	Philips	GEMINI_TF_TOF_16	(160, 160, 96)	(1.5, 1.5, 1.5)
012_S_6073	GE	Discovery_710	(160, 160, 96)	(1.5, 1.5, 1.5)
002_S_1261	Philips	GEMINI_TF_TOF_16	(160, 160, 96)	(1.5, 1.5, 1.5)
002_S_6009	Philips	GEMINI_TF_TOF_16	(160, 160, 96)	(1.5, 1.5, 1.5)
007_S_4488	GE	Discovery_690	(160, 160, 96)	(1.5, 1.5, 1.5)
003_S_4288	Siemens	Biograph64_TruePoint	(160, 160, 96)	(1.5, 1.5, 1.5)
002_S_4213	Philips	GEMINI_TF_TOF_16	(160, 160, 96)	(1.5, 1.5, 1.5)
114_S_6039	Philips	GEMINI_TF_TOF_64	(160, 160, 96)	(1.5, 1.5, 1.5)
036_S_4430	Siemens	Biograph40_TruePoint	(160, 160, 96)	(1.5, 1.5, 1.5)
041_S_4974	Siemens	HR+	(160, 160, 96)	(1.5, 1.5, 1.5)
007_S_4272	GE	Discovery_690	(160, 160, 96)	(1.5, 1.5, 1.5)
011_S_4827	Siemens	Biograph40_TruePoint	(160, 160, 96)	(1.5, 1.5, 1.5)
002_S_6053	Philips	GEMINI_TF_TOF_16	(160, 160, 96)	(1.5, 1.5, 1.5)
003_S_4644	Siemens	Biograph64_TruePoint	(160, 160, 96)	(1.5, 1.5, 1.5)
002_S_4799	Philips	GEMINI_TF_TOF_16	(160, 160, 96)	(1.5, 1.5, 1.5)
002_S_0413	Philips	GEMINI_TF_TOF_16	(160, 160, 96)	(1.5, 1.5, 1.5)
114_S_0416	Philips	GEMINI_TF_TOF_64	(160, 160, 96)	(1.5, 1.5, 1.5)
002_S_5178	Philips	GEMINI_TF_TOF_16	(160, 160, 96)	(1.5, 1.5, 1.5)
002_S_6030	Philips	GEMINI_TF_TOF_16	(160, 160, 96)	(1.5, 1.5, 1.5)
003_S_1122	Siemens	Biograph64_TruePoint	(160, 160, 96)	(1.5, 1.5, 1.5)
011_S_4893	Siemens	Biograph40_TruePoint	(160, 160, 96)	(1.5, 1.5, 1.5)
002_S_1155	Philips	GEMINI_TF_TOF_16	(160, 160, 96)	(1.5, 1.5, 1.5)
036_S_4715	Siemens	Biograph40_TruePoint	(160, 160, 96)	(1.5, 1.5, 1.5)
007_S_4387	GE	Discovery_690	(160, 160, 96)	(1.5, 1.5, 1.5)
007_S_4620	GE	Discovery_690	(160, 160, 96)	(1.5, 1.5, 1.5)

Supplementary Table 6. Dates of Imaging and MMSE.

ID	MMSE date	MPRAGE date	FLAIR date	DTI date	AV-45 PET date	AV-1451 PET date
023_S_1190	17/11/13	17/10/23	17/10/23		17/10/25	17/11/08
002_S_1280	18/3/7	17/3/13	17/3/13	17/3/13	17/3/02	18/3/5
011_S_4547	17/8/18	17/8/18	17/8/18		17/8/30	17/8/24
168_S_6142	17/12/5	17/12/18	17/12/18		18/1/17	18/1/3
002_S_6103	17/10/25	17/11/20	17/11/20	17/11/20	17/11/21	18/1/17
002_S_4654	18/5/15	17/5/3	17/5/3		17/5/2	18/5/22
022_S_5004	18/6/29	18/3/14	17/3/21		17/3/21	17/4/5
003_S_6067	17/12/4	17/8/18	17/8/18	17/8/18	17/10/13	17/10/18
002_S_4229	18/5/14	17/9/20	17/9/20		17/9/20	17/10/3
012_S_6073	17/9/18	17/9/22	17/9/22		17/10/12	17/10/11
002_S_1261	18/3/8	17/3/15	17/3/15		17/3/14	17/3/15
002_S_6009	17/4/1	17/4/17	17/4/17	17/4/17	17/5/16	17/5/15
007_S_4488	18/6/11	17/9/12	17/9/12	17/9/12	17/9/22	17/9/13
003_S_4288	17/10/2	17/10/3	17/10/3	17/10/3	17/10/3	18/2/22
002_S_4213	17/8/16	17/8/14	17/8/14	17/8/14	17/8/14	17/8/17
114_S_6039	17/8/10	17/7/21	17/7/21		17/8/24	17/10/4
036_S_4430	17/11/15	17/11/07	17/11/07		17/11/15	17/11/21
041_S_4974	17/10/30	17/10/5	17/10/5		17/8/24	17/10/12
007_S_4272	18/1/18	18/1/16	18/1/16		17/12/19	18/1/17
011_S_4827	17/8/24	17/8/31	17/8/31		17/8/28	17/9/7
002_S_6053	17/7/21	17/7/18	17/7/18	17/7/18	17/8/23	17/8/24
003_S_4644	17/6/26	17/6/21	17/6/21	17/6/21	18/2/28	18/4/17
002_S_4799	18/6/7	17/5/22	17/5/22	17/5/22	17/5/18	18/6/13
002_S_0413	17/6/16	17/6/21	17/6/21	17/6/21	17/6/15	17/6/21
114_S_0416	18/7/24	17/10/24	17/10/24		17/10/24	17/11/21
002_S_5178	17/6/6	17/5/31	17/5/31	17/5/31	17/6/5	17/5/31
002_S_6030	17/6/9	17/6/15	17/6/15	17/6/15	17/7/25	17/7/24
003_S_1122	18/7/25	17/5/18	17/5/18		17/8/8	17/8/10
011_S_4893	18/7/17	17/11/8	17/11/8		17/11/1	17/11/7
002_S_1155	18/5/9	17/4/24	17/4/24		17/4/20	17/4/24
036_S_4715	17/10/13	17/10/10	17/10/10		17/10/10	17/10/12
007_S_4387	17/10/31	17/11/1	17/11/1	17/11/1	17/10/24	17/11/29
007_S_4620	17/12/12	17/12/05	17/12/05	17/12/05	17/12/06	17/12/14

Supplementary Table 7. Participants IDs used in this study and corresponding ADNI official ID.

	ID	ADNI ID
AD	1	023 S 1190
	2	011 S 4547
	3	168 S 6142
	4	114 S 6039
	5	036 S 4430
	6	041 S 4974
	7	011 S 4827
	8	114 S 0416
	9	011 S 4893
	10	036 S 4715
HC	11	002 S 1280
	12	002 S 6103
	13	003 S 6067
	14	002 S 6009
	15	007 S 4488
	16	003 S 4288
	17	002 S 4213
	18	002 S 6053
	19	003 S 4644
	20	002 S 4799
	21	002 S 0413
	22	002 S 5178
	23	002 S 6030
	24	007 S 4387
	25	007 S 4620
MCI	26	002 S 4654
	27	022 S 5004
	28	002 S 4229
	29	012 S 6073
	30	002 S 1261
	31	007 S 4272
	32	003 S 1122
	33	002 S 1155

Supplementary Table 8. Overview of the used statistical tests in this study.

Statistical question (Figure)	Data	Independent (grouping) variable	Statistical Test	Justification
Do specific frequency bands in LFP differ between diagnostic groups for the empirical Abeta distribution? (Figure 7A)	Amount of regions with a specific frequency range, averaged over participants (group-wise) and all G values	1. HC and MCI (n=23) 2. AD and HC (n=25) 3. AD and MCI (n=18)	Kruskal-Wallis-Test	Variable does not meet the normality assumption of one-sided ANOVA
Do specific frequency bands in LFP differ between diagnostic groups for the homogeneous Abeta distribution? (Figure 7B)	Amount of regions with a specific frequency range, averaged over participants (group-wise) and all G values	1. HC and MCI (n=23) 2. AD and HC (n=25) 3. AD and MCI (n=18)	Kruskal-Wallis-Test	Variable does not meet the normality assumption of one-sided ANOVA
Does the mean frequency in EEG differ between diagnostic groups for the empirical Abeta distribution? (Figure 7C)	Mean EEG frequency, averaged over all channels and all participants (group-wise) for different values of G	1. HC and MCI (n=23) 2. AD and HC (n=25) 3. AD and MCI (n=18)	Kruskal-Wallis-Test	Variable does not meet the normality assumption of one-sided ANOVA
Does the mean frequency in LFP differ between diagnostic groups for the	Mean LFP frequency, averaged over all regions and all participants (group-wise)	1. HC and MCI (n=23) 2. AD and	Kruskal-Wallis-Test	Variable does not meet the normality assumption of one-

empirical Abeta distribution? (Figure 7D)	for different values of G	HC (n=25) 3. AD and MCI (n=18)		sided ANOVA
In how far is the regional LFP frequency linear dependent on the regional Abeta burden? (Figure 8)	Regional LFP frequency and regional beta PET SUVR for all regions and all G values, averaged over all participants (group-wise)	1. HC (n=15) 2. MCI (n=8) 3. AD (n=10)	Linear regression and correlation analysis	Question on linear dependency (given by p) and strength of its dependency (given by R ²)
In how far is there a linear dependency between the logarithmized structural degree and the local Abeta burden? (Figure 10B)	Natural logarithm of the structural degree of the averaged healthy standard connectome per region and local Abeta PET SUVR per region averaged over AD participants	AD (n=10)	Linear regression and correlation analysis	Question on linear dependency and strength of its dependency
In how far is there a linear dependency between the logarithmized structural degree and the local probability of theta rhythm in simulations with empirical Abeta distribution? (Figure 10D)	Natural logarithm of the structural degree of the averaged healthy standard connectome per region and the proportion of each regions simulations (201 for different values of G for 10 subjects) with dominant theta rhythm (simplified as a frequency that is below 8 Hz and not zero), averaged over AD participants	AD (n=10)	Linear regression and correlation analysis	Question on linear dependency and strength of its dependency
In how far is there a linear dependency between the logarithmized structural degree and the local probability of theta rhythm in simulations with random Abeta distribution? (Figure 10F)	Natural logarithm of the structural degree of the averaged healthy standard connectome per region and the proportion of each regions simulations (random Abeta distribution) with dominant theta rhythm, averaged over AD participants	AD (n=10)	Linear regression and correlation analysis	Question on linear dependency and strength of its dependency

1. Spiegler A, Kiebel SJ, Atay FM, Knösche TR. Bifurcation analysis of neural mass models: Impact of extrinsic inputs and dendritic time constants. *NeuroImage*. 2010;52(3):1041-58.
2. Strogatz SH. *Nonlinear dynamics and chaos : with applications to physics, biology, chemistry, and engineering: Second edition*. Boulder, CO : Westview Press, a member of the Perseus Books Group, [2015]; 2015.

LEBENS LAUF

Mein Lebenslauf wird aus datenschutzrechtlichen Gründen in der elektronischen Version meiner Arbeit nicht veröffentlicht.

VOLLSTÄNDIGE PUBLIKATIONSLISTE

1. **Stefanovski, L.**, A. Ghani, A.R. McIntosh, and P. Ritter, *Linking connectomics and dynamics in the human brain*. Neuroforum, 2016. **22**(3): p. 64-70. [IF 2016: 0,16]
2. Solodkin, A., J. Zimmermann, A.R. McIntosh, **L. Stefanovski**, and P. Ritter, *Neurological Biomarkers and Neuroinformatics: The Role of The Virtual Brain*, in *Molecular-Genetic and Statistical Techniques for Behavioral and Neural Research*, R.T. Gerlai, Editor. 2018, Academic Press: San Diego. p. 3-30. [Buchkapitel ohne IF]
3. **Stefanovski, L.**, P. Triebkorn, A. Spiegler, M.-A. Diaz-Cortes, A. Solodkin, V. Jirsa, A.R. McIntosh and P. Ritter for the Alzheimer's Disease Neuroimaging Initiative, *Linking Molecular Pathways and Large-Scale Computational Modeling to Assess Candidate Disease Mechanisms and Pharmacodynamics in Alzheimer's Disease*. Frontiers in Computational Neuroscience, 2019. **13**(54). [IF 2019: 2,535]
4. Triebkorn, P., J. Zimmermann, **L. Stefanovski**, D. Roy, A. Solodkin, V. Jirsa, G. Deco, M. Breakspear, A.R. McIntosh, and P. Ritter, *Identifying optimal working points of individual Virtual Brains: A large-scale brain network modelling study*. bioRxiv, 2020: p. 2020.03.26.009795. (Preprint ohne IF)

Datum und Unterschrift

DANKSAGUNG

Zunächst möchte ich mich bei Prof. Dr. Petra Ritter dafür bedanken, dass sie diese Arbeit durch ihre stetige Unterstützung überhaupt erst möglich gemacht hat und dafür, dass sie mich mit ihrer Begeisterung für die Gehirnsimulation angesteckt hat. Ich danke ihr außerdem dafür, dass sie mir stets die Möglichkeit gab, auch neue, ganz eigene wissenschaftliche Ideen zu verwirklichen.

Ich danke allen meinen Kollegen aus der Sektion für Gehirnsimulation, mit denen ich in den letzten Jahren zusammenarbeiten durfte. Insbesondere möchte ich Paul Triebkorn für alles danken, was er mir in dieser Zeit beigebracht hat, sowie für seine Geduld und Unterstützung bei unserer gemeinsamen Arbeit.

Ich möchte mich außerdem bei Prof. Dr. Harald Prüß dafür bedanken, dass er mir die Feinheiten der Klinik (vermeintlich) neurodegenerativer Erkrankungen nahegebracht hat und so erheblich dazu beigetragen hat, mich für die Disziplin der Neurologie zu begeistern.

Ich danke meinen Freunden, die mir immer geduldig und aufmerksam zugehört haben, wenn ich von meiner Forschung berichtete, selbst wenn sie besonders abstrakt und unverständlich war.

Ich bedanke mich außerdem bei meiner Biologielehrerin M. D. dafür, dass sie es schon in der Schulzeit geschafft hat, mich für das wissenschaftliche Arbeiten zu begeistern.

Ich danke meiner Familie für die immerwährende Unterstützung und den Halt, die sie mir stets gegeben haben. Meinem Vater danke ich besonders für seine geduldige Art und dafür, dass er immer zur Stelle ist, wenn ich seine Hilfe brauche. Meiner Mutter danke ich dafür, dass sie mir beigebracht hat, klinisch zu denken und entschieden zu handeln.

Zuletzt danke ich meiner Großmutter dafür, dass sie immer an mich geglaubt hat.